Asymmetric flow measurement in space constrained cooling water ducts using a traversing probe

Prepared by:

Rudzani Allan Mutshinya

MTSRUD002

Department of Mechanical Engineering

University of Cape Town

Supervisor:

Dr Wim Fuls

May 2015

Submitted to the Department of Mechanical Engineering at the University of Cape Town in partial fulfilment of the academic requirements for a Master of Science degree in Mechanical Engineering.

Key Words: Flow measurement, Asymmetric flow, Pitot tube, 90° Bend

Abstract

The majority of Eskom's coal-fired power stations utilize surface condensers and wet cooling towers to discard waste heat from the steam cycle. During the commissioning of the plant, an orifice is installed in the circulating cooling water (CW) ducts to measure the CW flow rate for cooling tower performance acceptance purposes. However, this instrument is removed afterwards because of the additional head losses it introduces, as well as the risk of its degrading over time to the point where pieces may break off and damage equipment downstream. As a result, there is currently no installed instrument measuring the CW flow rate.

The aim of this research was to identity and recommend a type of flow measurement technique suitable for flow measurements in the CW ducts. After conducting a literature survey, the author restricted research to a local flow measuring technique as a result of physical constraints on site. In addition, the flow profile in the CW ducts was unknown so that existing flow rate measurement standards could not be applied. Thus the focus of this research was to predict the expected accuracy of local flow measurements in asymmetric flow conditions.

A CFD model was developed to simulate site conditions and to generate asymmetrical flow profiles through a 90° bend. This exercise provided indicative flow profiles and more realistic sets of data which were inputs into the algorithms. The algorithms were used to predict the expected measurement accuracy of the local flow measurement technique based on three different traversing paths; number of traverses; number of measurement points along each traverse; and the measurement location downstream of the 90° bend.

As a result of the above, three types of traversing paths were considered in this research, namely: a single traverse through the pipe centre; two ±45° traverses; and a chord-wise traverse. Furthermore, investigations were conducted at: 0D; 2.2D; 3.3D; 6.6D; 11.1D and 20D downstream of a 90° bend, where D is the pipe diameter. In addition to the CFD simulations, physical tests were performed at the Eskom Water Flow Calibration Laboratory. The tests were performed at flow conditions similar to those considered in the CFD simulations. Test investigations were conducted at: 2.2D; 6.6D; 11.1D and 20D downstream of a 90° bend, for the three traversing paths mentioned above.

The various algorithms successfully predicted the expected flow measurement. In particular, the two ± 45° traverses, provided the least static errors and most consistent results for a given distance away from a 90° bend. At distances greater than 11D and $Re \geq 10^6$, if was found that the single traverse at 90° to the bending axis, provides similar static errors to that of the two ± 45° traverses.

The outcome of this research will enable proper verification of the contractors' guarantees on cooling tower performances. Furthermore, it will be possible to determine the flow rate into a single main condenser and to monitor the performance of the CW pumps.

Declaration

I, Rudzani Allan Mutshinya, hereby declare the work contained in this dissertation to be my own. All information which has been obtained from various journal articles, text books or other sources has been referenced accordingly. I have not allowed, and will not allow, anyone to copy my work with the intention of passing it off as his/her own work or part thereof.

Signed by candidate

_____

Rudzani Mutshinya

24 May 2015

Date

Acknowledgements

First and foremost, I would like to thank my God almighty who saw me through this research. For with Him, everything is possible.

I would like to thank the Eskom Power Plant Engineering Institute for sponsoring this research.

I would like to express my deepest gratitude to Dr Wim Fuls, my academic supervisor, for his patience, guidance, constructive criticism and encouragement during this research. I thank him for imparting his knowledge and insight to me.

I express my greatest appreciation to Dr Francois du Preez, my industrial supervisor, for his valuable input and suggestions during this research.

I also thank the staff at the Eskom Water Flow Calibration Laboratory. In particular, I thank Mr Ferdi Liebenberg and Mr Patrick Dube for their valuable technical support during the experimental work of this research.

Last but not least, I thank my darling wife, Mrs Rivalani Mutshinya, for her support and understanding during this research. She was indeed my cheerleader and a pillar of strength.

Table of Contents

List of Figures

List of Tables

List of Nomenclature

General symbols

A	Cross-sectional area of a stream normal to the velocity, [m^2]
C	Coefficient of discharge for orifices, tubes and nozzles
B	Magnetic flux density, [Tesla]
D	Diameter of pipe, [m]
e	Induced voltage, [V]
E	Young modulus, [Pa]
f	Frequency, [Hz]
F_b	Blockage factor
g	Acceleration of gravity, [m/s^2]
h	Head, [m]
i	Increment range variable
I	Second moment of area, [m^4]
j	Increment range variable
k	Spring stiffness
L	Length, [m]
m	Mass, [kg]
n	Number of increments
o	Outer
P	Pressure, [Pa]
Q	Rate of volume flow, [m^3/s]
r,R	Radius, [m]
Re	Reynolds number
S_t	Shrouhal number
T	Temperature, [°C]
U	Mean axial fluid velocity, [m/s]
V	Local velocity of the fluid, [m/s]
v	Volume, [m^3]

Greek symbols

α	Angle, [°]
β	Angle, [°]
Δ	Change
ε	Uncertainty, [%]
θ	Any angle, [°]
μ	Absolute or dynamic viscosity, [Pa.s]
ν	Kinematic viscosity, [m^2/s]
ρ	Density, [kg/m^3]
σ	Stress, [Pa]
∑	Sum
Ø	Diameter, [m]

Acronyms and Abbreviations

ave	Average
br	Brass
BS	British standard
CAD	Computer aided design
CFD	Computational fluid dynamics
Emf	Electromotive force
in	Inner
ISO	International Organization for Standardization
PS	Power station
out	Outer
ss	Stainless steel

Glossary

Vertical plane	Plane parallel to the bending axis
0° Traverse	Traverse parallel to the bending axis
90° Traverse	Traverse perpendicular to the bending axis
0° and 90° Traverses	Multiple traverse at 0° and 90° to the vertical plane
-45° and +45° Traverses	Multiple traverse at ±45° to the vertical plane
Bend	90° Bend
Bending axis	The axis around which the bend of a pipe occurs
Measurement accuracy	An indication of how the a measured quantity compares to the real measurement
Static error	Errors resulting from of any reason or assumption made in the algorithms. The error remain constant from some number of discretized elements to infinity
Turndown	The maximum calibration divided by the minimum required calibration in order to determine the minimum reliable flow reading for a given maximum flow rate

1. Introduction

The majority of Eskom's coal-fired power stations utilize surface condensers and wet cooling towers to discard waste heat from the steam cycle. The CW flow rate to the cooling tower affects the temperature at which condensation takes place inside the condenser. This, in turn, affects the back pressure of the turbine as well as overall efficiency of the plant. A lower cooling temperature reduces plant efficiency and can cause the turbine to trip on "low vacuum".

During commissioning of the plant, an orifice is installed in the circulating CW ducts to measure the CW flow rate for acceptance purposes. However, this instrument is removed afterwards because of the additional head losses it incurs, as well as the risk of its degrading over time to the point where pieces may break off and damage equipment downstream. This means that there is currently no installed instrument recording the flow rate of the cooling water.

A coal-fired power station, shown in Figure 1 below, consists of different flow paths with different flowing media. This research focuses on the main cooling system of the power station and those flow meters relevant to operating conditions.

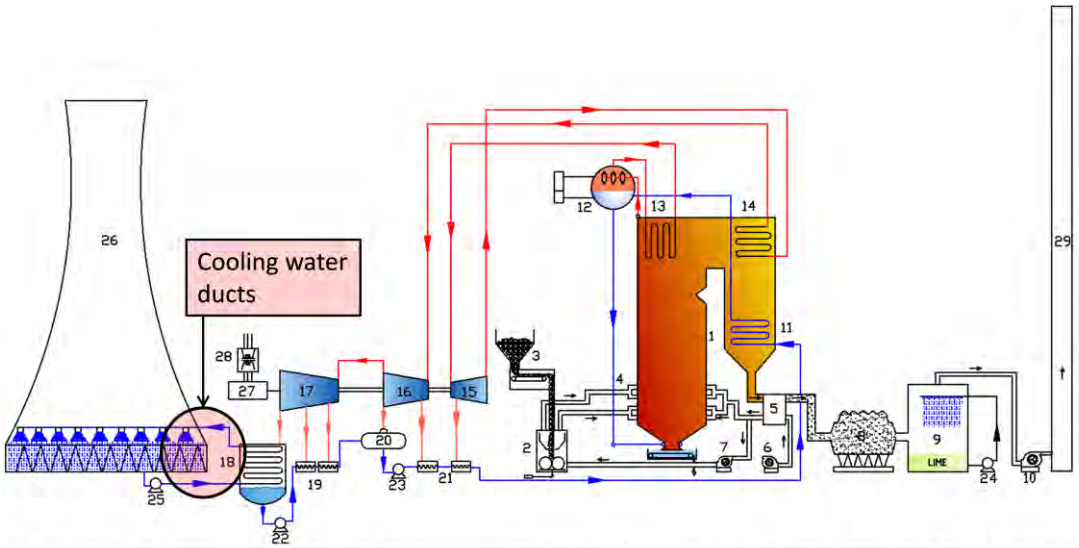

1	Boiler	6	Forced draught fan	11	Economiser	16	Intermediate pressure turbine	21	High pressure feedwater heaters	26	Wet cooling tower
2	Mills	7	Primary air fan	12	Boiler drum	17	Low pressure turbine	22	Condensate extraction pump	27	Generator
3	Coal feeder	8	De-dusting plant	13	Super-heater	18	Condenser	23	Boiler feedwater pump	28	Generator transformer
4	Burners	9	Flue gas desulphurisation plant	14	Re-heater	19	Low pressure feedwater heaters	24	Flue gas desulphurisation pump	29	Stack
5	Air heater	10	Induced draught fan	15	High pressure turbine	20	Deaerator	25	Circulating cooling water pump		

Figure 1: Basic power plant layout (EPPEI Annual Booklet 2014)

Cooling water circulates from the CW pump house to the main condenser of the turbine. The heat is then transferred via the condenser tubes from the process water-steam mixture in the shell of the condenser to the circulating cooling water inside the tubes. The cooling water is transported through the CW ducts to the cooling towers where the heat is released to the atmosphere.

As part of the efficiency studies done on all plants in Eskom, all cooling systems need to undergo detailed performance testing. This requires accurate measurement of the CW flow rate, typically an uncertainty of ±1% for acceptance test purposes. Installing the original orifice plates into the CW ducts would require a multi-unit shutdown, as well as plenty of engineering time. A multi-unit shutdown is not feasible, given the current electricity generation crisis Eskom is facing.

An alternative, less intrusive, method of measuring the CW flow rate is therefore needed. The device should be such that it can be moved from one station to the next, as well as function on all plants requiring CW flow measurement. A further opportunity exists to install a similar device in the CW duct permanently for online flow measurement and integration into the EtaPro online condition monitoring system.

1.1 Aim of the project

The main aim of the project is to develop a flow rate measuring technique for CW ducts and recommend an optimal method that will be implemented at Eskom power stations. The flow measurement technique identified by this research will be utilized for performance test purposes, but could also be converted for later use in online measurements.

1.2 Research approach

A study of the literature on state-of-the-art flow measurement technologies was conducted. The study identified typical practical considerations and key differences of various flow measurement techniques in order to shortlist options.

A comprehensive list was also compiled of the physical CW duct layout designs and measuring pit details of power stations where the research would be relevant in Eskom. This was achieved by conducting site visits to collect drawings and take measurements of unknown parameters.

The flow rate conditions (regime) and flow development (velocity profiles) were identified in order to apply the correct fundamental equations and analytical model when selecting the most practical flow rate measuring technique.

Current power station hydrodynamic entrance lengths and other potential upstream flow disturbances were also studied in order to understand the expected flow profile. It was especially important to have knowledge of the level of symmetry of the flow profile. In addition, an investigation was conducted to determine possible stratification or other factors, such as sedimentation at the bottom or trapped air at the top that might cause the fluid cross section to deviate from a perfect circle.

Although a study on various techniques was conducted, the traversing local flow measurement was the intuitive solution. This study therefore focuses later on the traversing local flow measurement technique. An analytical model was developed with the aim of determining the number and locations of measurement points across the duct to achieve the desired accuracy.

The following test codes and standards were studied and used as selection criteria of the traversing probes:

- BS 1042 Part 1 : Measurement of fluid flow in closed conduits;
- ISO 3966:2008 : Measurement of fluid flow in closed conduits – Velocity-area method using pitot static tubes (supersedes BS 1042-2.1:1983);
- ISO 7194:2008 : Measurement of fluid flow in closed conduits - Velocity-area methods of flow measurement in swirling or asymmetric flow conditions in circular ducts by means of current-meters or pitot static tubes (supersedes BS 1042-2.3:1984), and
- BS 4485 Part 2: 1988: Methods for performance testing.

However, the use of the above standards for flow measurement is valid only for symmetrical flow profiles. Since there was a probability of the flow being asymmetrical, especially in instances where there were flow disturbances nearby, upstream of the flow meter, a different approach was adopted.

Indicative CFD analyses were undertaken to produce representative asymmetrical flow profiles. These were then used to develop a traversing scheme to predict the flow profile with minimal measurements. Using Computer Aided Design (CAD) software, it was possible to produce a 3D surface that was utilized to develop the chord-wise algorithm.

Scale model experimental tests were also carried out to confirm the method of estimating the measured accuracy for a given flow profile. The details and level of validation that these tests produced were determined during the project.

A sensitivity analysis was performed on the recommended measurement method considering the systematic error and random errors of the measurements. These support the overall accuracy of the measurement method.

Also used in the research was a traversing pitot tube which acts like a cantilever beam in the flow. The necessary load conditions, including vibrations due to vortex shedding, were studied to establish a set of technical requirements. Further or additional requirements and concepts for the sealing and non-intrusive installation of the device were also developed.

1.3 Outline of report

Chapter 2 documents research of the literature on flow measurements.

Chapter 3 provides an additional literature study, in this instance focusing on the design of a pitot tube.

Prior to utilizing test methods to verify and validate the mathematical algorithm, flow phenomena in ducts with 90° bend were studied. The findings are documented in Chapter 4.

The developed algorithm is included in Chapter 5; its validation and testing are documented in Chapter 6; and the applicability of the algorithm is included in Chapter 7.

The physical experimental work and findings are documented in Chapter 8.

The research conclusions and recommendations are documented in Chapter 9, which is followed by the Appendices.

2. Flow Measurement Literature Review

The fundamentals for the measurement of fluid flow can be derived or expressed using the following basic concepts of energy and physical properties [1]:

- The continuity of flow equation
- Bernoulli's equation of energy
- Fluid density and viscosity

These fundamentals were applied in this research for the selection of a feasible flow meter.

2.1 Flow measurement principles

The continuity of flow equation confirms the conservation of mass law which states that the total mass entering a system or boundary is equal to the total mass leaving the boundary. Therefore the mass of the closed system remains constant with time. This is shown by Equation (1) and Figure 2.

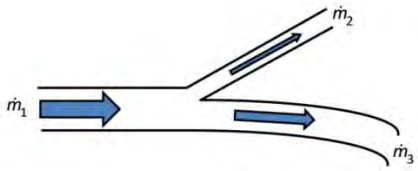

Figure 2: Conservation of mass

$$\sum \dot{m}_{in} = \sum \dot{m}_{out}$$
$$\dot{m}_1 = \dot{m}_2 + \dot{m}_3 \quad (1)$$

The balance of the kinetic and potential energy of the fluid particles can be expressed by the Bernoulli Equation (2) . It states that the energies in the fluid along a streamline remain constant for steady state flows with insignificant fluid frictional and compressibility effects.

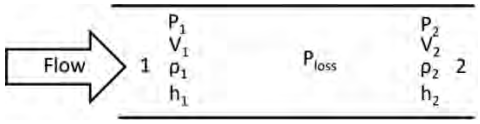

Figure 3: Schematic illustration of the Bernoulli equation

The Bernoulli equation is only valid for incompressible flows [2] and states that an increase in the pressure drop or decrease in the potential energy of a fluid will result in a simultaneous increase in the velocity of the fluid.

$$P_1 + \frac{1}{2}\rho_1 V_1^2 + \rho_1 g_1 h_1 - P_{loss} = P_2 + \frac{1}{2}\rho_2 V_2^2 + \rho_2 g_2 h_2 \quad (2)$$

It is important to note that every flow contains a frictional component thus the inviscid flow assumption is an ideal assumption.

The Bernoulli equation can be expanded to include energies added or removed from the fluid. For instance, a pump will add energy to the fluid and a turbine will extract energy from the fluid.

Most flow rate measurements are inference measurements. In other words, the flow meter measures certain fluid parameters and deduces the flow rate. A flow meter would measure the pressure drop across a known cross-sectional area and relate the pressure drop to the average velocity of the flow. This type of measurement is also referred to as bulk flow measurement. Furthermore, some flow measurements result from measuring a quantity of fluid per unit time. Examples are the weight tank system, used to determine the bulk mass rate, and the bucket system to calculate the volumetric flow rate. Some bulk flow measurements are attributable to inferring or correlating vibrations or motions of a flow meter component to the flow velocity. The accuracy of this bulk flow measuring technique depends on the uncertainty of the equipment, which is typically ±0.2%.

Bulk flow or average velocity can be determined by taking the weighted average of a number of point velocities [3]. Point velocity measurements are velocity measurements of the fluid at a specific point. Such measurements are frequently used in the aerodynamic industry.

2.2 State of the art of flow measurement

There are numerous flow meters with different flow measurement principles. Their selection is influenced by the following: flow medium; required accuracy; cost and operating conditions. This research highlights flow meters than can be utilized based on site constraints, accuracy and cost. The flow meters studied in this research are summarized in Figure 4.

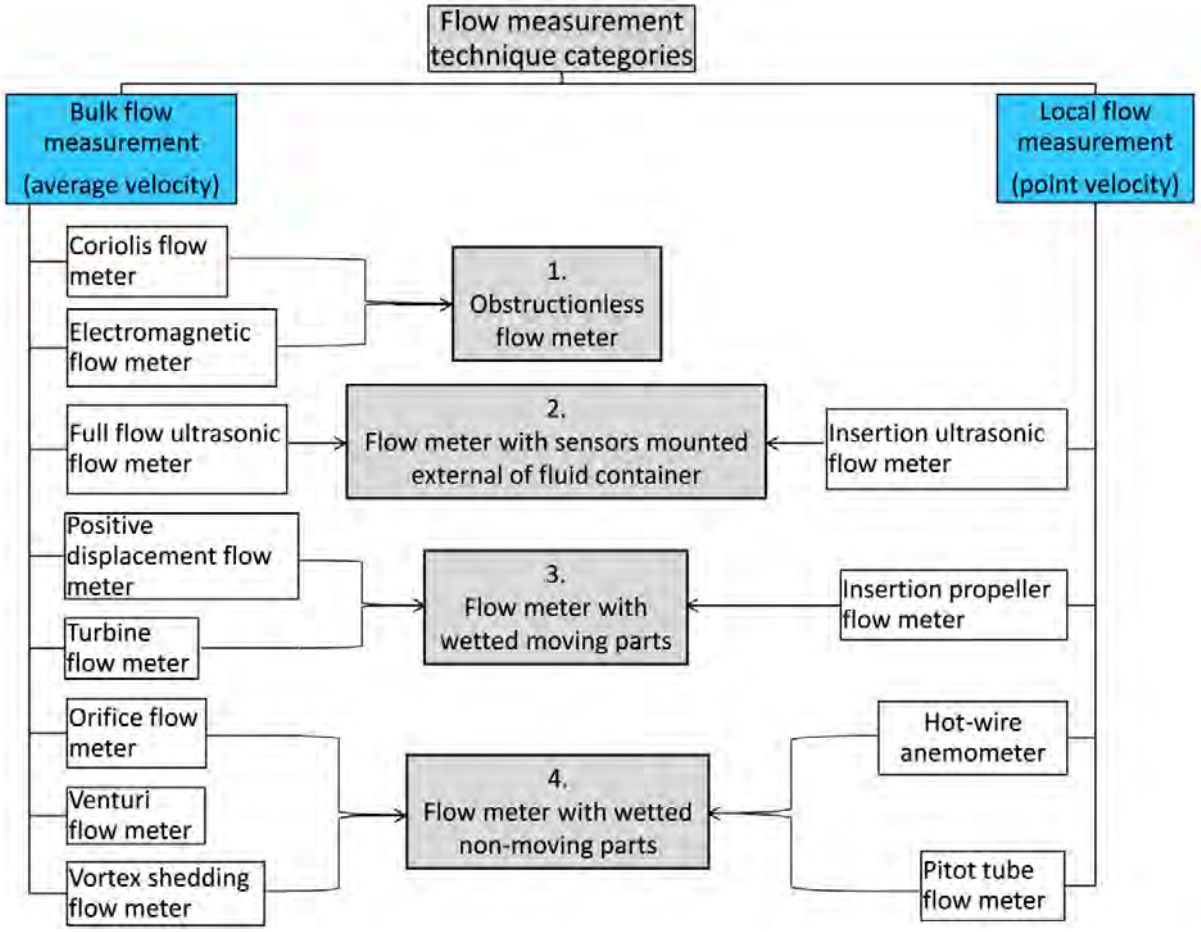

Figure 4: State of the art of technology

The following section provides a description and basic operating principles of each flow meter included in Figure 4.

The different types of flow meter can be identified as obstructionless flow meters, flow meters with sensors mounted outside the fluid container, flow meters with wetted moving parts or flow meters that have wetted non-moving parts.

2.2.1 Obstructionless flow meters

These types of flow meters measure the flow rate without obstructing the flow path. This category includes flow meters such as the coriolis meter and the electromagnetic flow meter.

a) Coriolis mass flow meter:

The coriolis flow meter uses the inertia of the flow to measure directly the mass flow rate and not the flow velocity nor volumetric flow rate. Since this flow meter directly measures the mass flow, it can achieve high accuracy over a wide range of flow rates and flow conditions. This is achieved by channelling the flow to be measured through the tube, allowing for fewer sources of errors in the measurement: these flow meters typically have an uncertainty of ±0.2% [2].

Flow detectors, indicated as FD_1 and FD_2 in Figure 5, measure the vibration or the oscillation of the flow tubes.

Figure 5: Coriolis meter operating principle [4]

Unfortunately the accuracy achieved by the coriolis meter comes at a high cost, incurring modifications to the main flow line. However, the coriolis meter remains simpler to install compared with other flow meters such as the venturi, nozzle and orifice plate.

The most notable advantage of the coriolis meter is that it is not affected by swirls or asymmetrical flows. Therefore, less effort is required to condition the flow profile, which is not the case with the electromagnetic flow meter.

b) Electromagnetic flow meter:

Similar to the coriolis flow meter, the electromagnetic flow meter offers non-intrusive flow measurements depending on the type of design. They operate on principles established in experiments conducted by Michael Faraday in the 1830s. In these experiments, an electromotive force was generated by moving a conductor across a magnetic field [3]. Faraday also found that the induced emf is proportional to the speed at which the conductor moves perpendicular to the magnetic field. In the case of the electromagnetic flow meter, the fluid acts as a conductor and an emf is generated across the pipe diameter owing to the magnetic induction.

The electromagnetic flow meter has been widely used across the industry since its invention in the mid-1950s. Furthermore, it is available in various designs, most common of which are full flow meters and insertion type meters [3] as shown in Figure 6(a) and Figure 6(b) respectively.

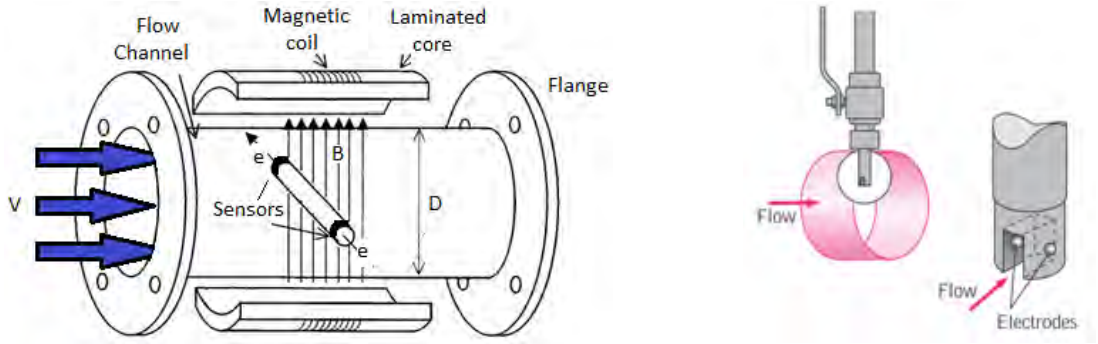

Figure 6: Electromagnetic flow meter (a) full-flow type [2] (b) insertion type [3]

Of interest in this category is the full flow electromagnetic flow meter as it does not interfere with the flow. It therefore does not introduce any head losses when measuring the flow rate.

As in Faraday's experiments, a magnetic coil encloses the pipe where the flow is to be measured. A current is then passed through the magnetic coil to generate a magnetic field. Two electrodes on either sides of the pipe are drilled into the pipe but remain flush with the inner surface of the pipe, thus causing no obstruction to the flow. A voltmeter connected to the electrodes measures the voltage difference across the electrodes and is related to the flow velocity.

The velocity of the flow (*V*) can be calculated by dividing the induced voltage (*e*) by the product of the magnetic flux density (*B*) and the pipe inner diameter (*D*) where the measurement is taken. This is represented by Equation (3).

$$V = \frac{e}{BD} \tag{3}$$

The quality of flowing medium therefore plays an important role as it is required to have a large enough amount of charged particles [3]. For this reason, flow rates of deionised water cannot be measured by an electromagnetic flow meter [2]. Nonetheless, uncertainties of up to ±5% can be achieved in applications where there is poor electrode resistance contact with the fluid due to insufficient flow impurities. However, electromagnetic flow meters have been reported to achieve uncertainties of ±0.25% [2].

Compared with the Coriolis meter, electrometric flow meters are expensive but unlike the coriolis meter, they are restricted in the types of fluid for which they can measure the flow rate.

2.2.2 Flow meters with sensors mounted outside the fluid container

Flow meters in this category are also obstructionless flow meters, but they are mounted outside the pipe transporting the flow to be measured. Ultrasonic flow meters are a typical example of flow meters in this category.

Ultrasonic flow meter:

There are two principles that ultrasonic flow meters adopt: the transit-time (or time in flight) and Doppler effect (or frequency shift). Both these principles generate a transmitting and receiving transducer which respectively send and receive the signal. The sound waves that are generated are transmitted through the pipe wall thickness and the propagation of the wave signal through the flowing fluid is recorded. As the name suggests, the signals are typically at a frequency of the order of 1 MHz [3].

Ultrasonic flow meters perform poorly when measurements are taken in areas of asymmetrical flow profile created by high levels of swirls and eddies [3]. Such flow disturbances may be present downstream of a 90° bend.

The transit time type ultrasonic flow meter is widely used in industry. The principle of transit time ultrasonic flow meters compares the travelling time of the wave signals travelling in the direction of the flow and those travelling in the opposite direction.

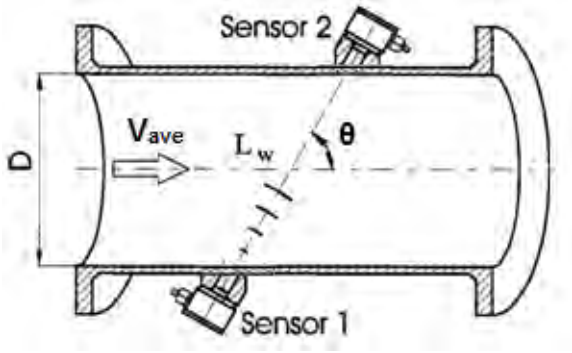

Figure 7: Transit time ultrasonic flow meter [2]

For a known travelling path (L_w), it is possible to calculate the average flow velocity (V_{ave}) in the pipe. It involves two transducers that alternately transmit and receive ultrasonic waves, one in the direction of flow and the other in the opposite direction. The travel time for each direction can be measured accurately, and the difference in the travel time can be calculated.

Doppler-effect ultrasonic flow meter utilizes the same principle as that of the transit time ultrasonic flow meter. However, these flow meters employ the Doppler effect to measure the average flow, along the sonic, directly from the fluid. This is achieved by mounting a piezoelectric transducer on the outer surface of the pipe which transmits a sound wave at a constant frequency into the flowing liquid through the pipe wall. Unlike the transit time ultrasonic flow, the wave signal is returned to the piezoelectric transducer by reflecting off the impurities in the fluid such as suspended solid particles and gas bubbles entrained in the fluid. A microprocessor then compares the frequency shift between the transmitted and reflected signals.

The advantage of ultrasonic flow meters is that they have a multi-industrial application, extending to the medical field where they are used to measure the flow of blood in the vascular system. Furthermore, being non-intrusive they do not introduce any pressure loss into the system. In addition, clamps-on-ultrasonic flow meters are relatively easy and quick to install and require no pipe modifications [3]. However, these flow meters can produce erroneous measurements when installed incorrectly. It is worth mentioning that this holds true for all flow meters.

2.2.3 Flow meters with wetted moving parts

These flow meters are distinguished by mechanical motion of their parts as the fluid flow makes contact with them. Typical flow meters in this category include positive displacement and turbine meters.

a) Positive displacement meter:

This type of flow meter utilizes the concept of positive displacement to measure the volumetric flow rate of a continuous flow. This is achieved by periodically entrapping a portion of the flow and returning it to the flow stream, into a cavity with a known volume. The number of entrapments over a known period thus provides the total volumetric flow rate of the stream.

There are a number of positive displacement flow meters used in industry such as the bi-rotor type and the piston type flow meter. These examples are shown in Figure 8 and Figure 9.

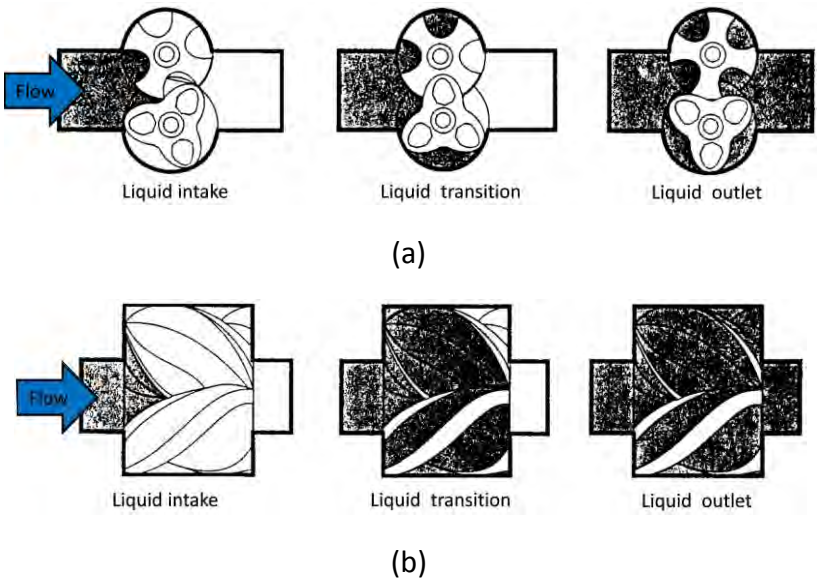

Figure 8: Bi-rotor type flow meter: (a) standard principle (b) axial flow principle [2]

A disadvantage of positive displacement meters is that they are fully intrusive flow meters. Small amounts of energy are absorbed from the flowing fluid. This energy is

transferred to the moving parts in order to overcome their internal resistance, thus enabling motion of the parts and creating a pressure drop across the flow meter.

Although gear lashing, in certain positive displacement meters, may introduce in-flow measurement accuracies, they remain capable of achieving low measurement inaccuracies, thus providing accurate volumetric flow rates. A tight tolerance is required between the moving and non-moving parts.

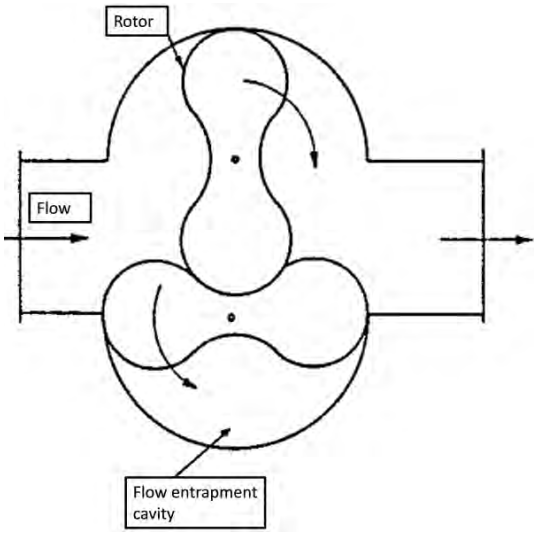

Figure 9: Gear type flow meter [2]

Unlike the flow meters already discussed in this chapter, positive displacement flow meters are not sensitive to upstream flow profile distortions [2]. The positive displacement meter can therefore be installed at close proximity to a flow disturbance and still take volumetric flow rate measurements without any loss of accuracy. Although this may be desirable in most industrial applications, the size of the requisite pipeline coupled with the space constraint involved may limit the use of the positive displacement flow meter.

b) Turbine flow meter:

The turbine flow meter is also an in-line flow meter. It has seen great improvements to the original axial vaned flow meter principle, credited in 1970 to Woltman [2]. The turbine flow meter consists of a single turbine rotor mounted concentrically on a shaft. The turbine rotor is enclosed within a cylindrical housing through which the flow passes.

The flowing fluid causes the turbine rotor to rotate and the rotation is detected by a sensor, typically a magnetic type. Each rotor blade rotation infers a fixed volume of fluid passing per unit time.

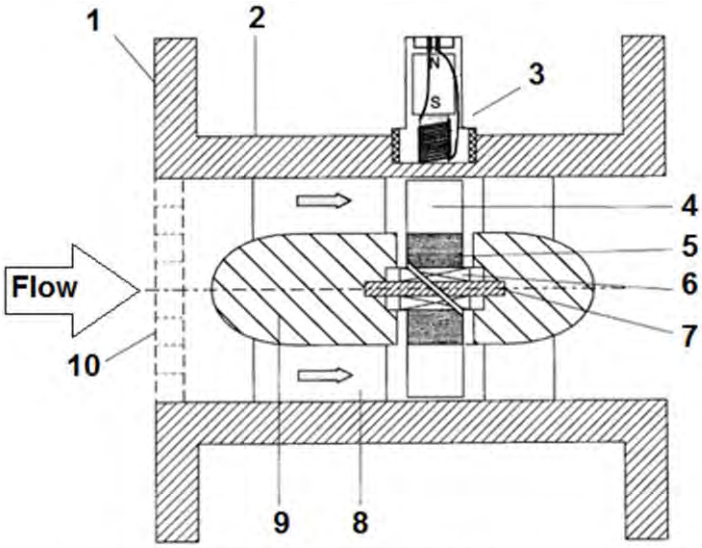

1	Flange	4	Rotor blade	7	Rotor shaft
2	Flow meter body	5	Rotor hub	8	Flow straightener
3	Rotation transducer	6	Rotor shaft bearing	9	Diffuser
				10	Flow conditioning plate

Figure 10: Longitudinal section of an axial turbine [2]

There is an assortment of axial turbine flow meters with a variety of applications in industries including oil, petrochemical, natural gas, aerospace and other industries. Irrespective of the industrial application, turbine flow meters are designed for clean flows and require no power supply [5].

The turbine meter is, however, recommended only for low viscosity flow. Furthermore, the flow upstream and downstream of the flow meter requires conditioning because the moving parts of the meter are sensitive to the flow profile. In addition, turbine meters require twenty to thirty diametric lengths upstream of the flow meter [5].

2.2.4 Flow meters that have wetted non-moving parts

Unlike those described in the previous section, flow meters of this type experience no mechanical motion of the parts, but the fluid flow does make contact with the parts. Typical examples of flow meters in this category include vortex shedding meters and thermal anemometers.

a) Vortex shedding meter:

These flow meters utilize the concept of flow separation where the fluid separates as it flows around bluff body placed inside the pipe. This phenomenon is referred to as vortex shedding or the Von Karman principle. The vortices that are generated as flow passes the bluff body are shed periodically, the shedding frequency demonstrably proportional to the average flow velocity. An ultrasonic, fibre-optic or sensitive pressure sensor detects and monitors the fluctuation in the vortex pattern. It further transmits a pulsating output signal and a microprocessor utilizes the vortex shedding or pulsating frequency to calculate and display the average flow velocity.

Figure 11 shows the basic operation of a vortex flow meter where the average velocity (V) is calculated by

$$V = \frac{f_{st} \cdot d}{S_t} \tag{4}$$

where S_t is defined as the Strouhal number and f_{st} is the vortex shedding frequency generated when the fluid pass the bluff object of characteristic diameter d.

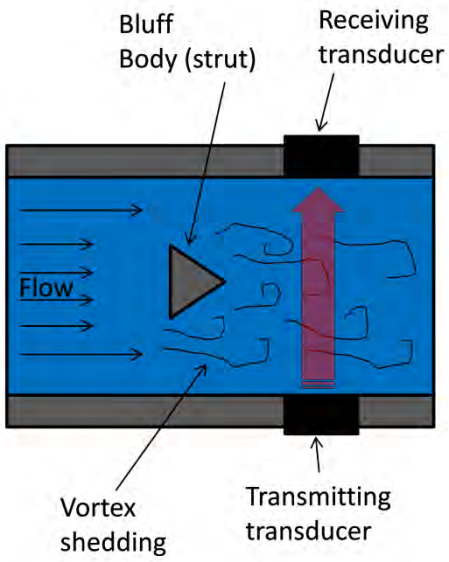

Figure 11: The operation of a vortex flow meter

From Equation (4), it can be seen that the average flow velocity is proportional to the vortex shedding frequency. The vortex flow meter is capable of accurately measuring wide ranges of Reynolds numbers, typically from 10^4 to 10^7.

b) Hot wire anemometer:

The hot wire anemometer is a typical example of the thermal anemometers available in the market. These flow meters are commonly used in fluid research facilities and have been in existence since the late 1950s [3]. The hot wire anemometer measures the local velocity of a flowing fluid by means of an electrically heated sensor and the forced convective heat transfer Q off the sensor by the flowing fluid, as shown in Figure 12. This sensor is usually made of different alloys such as platinum, tungsten or platinum-iridium [3].

The forced convective heat loss from the sensor is a function of the flow velocity. Two operating principles, namely constant temperature and constant current, are discussed below.

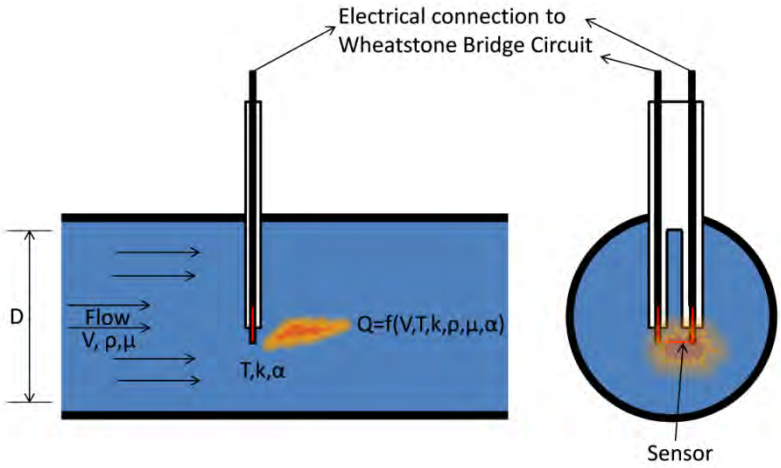

Figure 12: Hot-wire anemometer

The constant temperature anemometer (CTA) is the most common type [3] of thermal anemometer. The temperature of the sensor tends to decrease with an increase in flow rate of the surrounding fluid. However, an electronic control ensures that the sensor remains at the same temperature by changing the electrical current to the sensor (resistor). It can be shown from Ohm's law, in Equation (5), that the voltage (E) across the sensor with a constant resistance (R), changes with current (I).

$$E = IR \tag{5}$$

The voltage across the sensor or the electric current passing through the sensor can be measured by an amplifier. A correlation between the voltage and the flow velocity was

obtained by using forced convection relations and conservation of energy laws. This can be expressed by King's law [3] as

$$E^2 = a + bV^n \tag{6}$$

From Equation (6), the measured local velocity (V) can be represented as,

$$V = \sqrt[n]{\frac{E^2 - a}{b}} \tag{7}$$

where n, a and b are the calibration factors for a given probe and E is the voltage in volts.

From these relations, it can be seen that a higher flow velocity requires a higher voltage across the sensor to maintain constant temperature. This is a result of a higher heat transfer rate from the sensor to the surrounding fluid.

In the case of a constant current anemometer (CCA) the change in resistivity of a Wheatstone bridge is measured when the current through the sensor is kept constant. Thus, for a constant current, the resistivity of the sensor is a function of the flow

velocity V.

As is applicable to all flow meters, thermal anemometers have limitations too. For instance, they are sensitive to flow variations. In contrast, constant temperature anemometers have a reduced sensitivity to flow variations and are therefore more widely used than the constant current anemometer [3].

In the case of the hot-wire anemometer, flow with high levels of solid particles or contaminants poses a breakage hazard for the wire sensor. The hot-wire anemometer is therefore structurally vulnerable at high levels of contamination in the flowing fluid. A remedy for this problem is the use of a larger and more robust sensor which causes more interference to the flow. In addition, the flow meter may then elicit a lower frequency response [3]. Nonetheless, its fragility suggests it should be used in clean gas flows.

c) Orifice:

The orifice is a typical example of differential flow meters. They essentially consist of two elements: a flow obstruction to create a pressure drop and a method to measure the resulting pressure drop. The orifice flow meter was commercialized in the early 1900s and has a typical flow rate measurement uncertainty of ±2% [2]. In essence, it is a plate with a specific hole that can be clamped between flanges in a pipeline [2].

The orifice is a simple flow meter without moving parts so it is a reliable and relatively cheap flow meter. Its simplicity is shown in Figure 13.

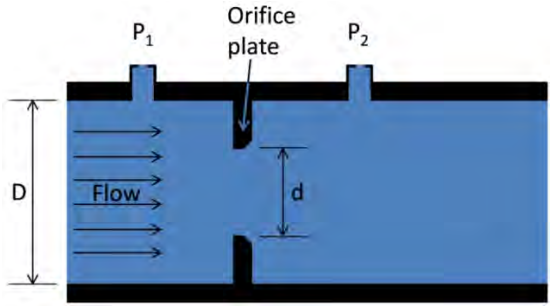

Figure 13: Orifice flow meter

The operation of the orifice is based on observations made by Bernoulli, who noted that the velocity in a pipe increases as it passes through a restricted area resulting in the decrease of the static pressure in the throat or restriction section [2]. Using Bernoulli's Equation (2), described early in this chapter, the pressure difference upstream and downstream of the plate is recorded to obtain the average flow velocity.

The theoretical average flow velocity (V_{ave_T}) of fluid flowing with a density ρ can be calculated from

$$V_{ave\_T} = \frac{A_2}{A_1}\sqrt{\frac{2(P_1 - P_2)}{\rho(1-\beta^4)}} \tag{8}$$

Since Equation (8) provides the ideal average velocity (V_{ave}), the reference average velocity is obtained by introducing an orifice discharge coefficient (C_d) into Equation (8) to give Equation (9). The discharge coefficient corrects the theoretical velocity, taking into account the orifice plate geometry

$$V_{ave} = C_d \frac{A_2}{A_1}\sqrt{\frac{2(P_1 - P_2)}{\rho(1-\beta^4)}} \tag{9}$$

where A_1 and A_2 are the upstream and orifice cross-sectional areas respectively. The ratio of the orifice diameter to the upstream diameter is denoted by β. The pressures upstream and downstream of the orifice plate are denoted by P_1 and P_2 respectively.

In order to use Equation (9), the flow must be fully developed in the sense that the flow profile must be steady.

It is important to note that this requirement does not refer to the profile being either symmetric or asymmetric. This means that the orifice is sensitive to the flow profile and, like most flow meters, it requires at least ten diameters upstream and five diameters downstream of the flow meter.

Although orifice flow meters are relatively cheap, they introduce a permanent pressure drop in the pipeline, possibly resulting in an increase in the pumping power required. Further, the flow meter is limited to a measurement range of typically 3:1. In addition, the orifice requires more maintenance and monitoring because the leading edge of the orifice is susceptible to wear, which may severely affect measurement accuracy. For this reason, the orifice is recommended for use in clean fluids [2].

d) Venturi:

The venturi is the oldest type of differential pressure flow meter, dating back to 1887 [2]. Its operation is similar to that of an orifice. Unlike the orifice, the venturi allows for smooth entrance of the fluid into the restricted or throat section as shown in Figure 14.

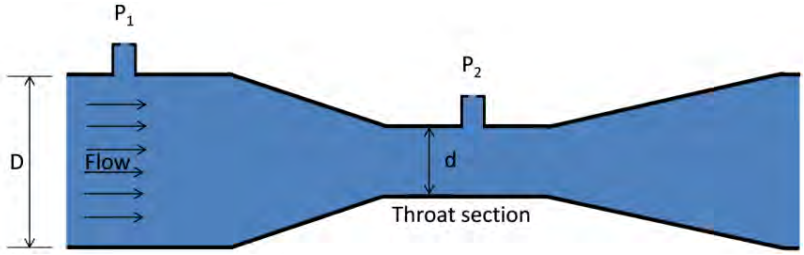

Figure 14: Venturi flow meter

The venturi thus introduces less pressure loss than an orifice, resulting in the discharge coefficient C_d being closer to unity, typically 0.95 [2]. Furthermore, the gradual design of the venturi suggests that it is less sensitive to wear than the orifice. Hence, the venturi can be used in either dirty gases or liquids. In addition, it requires shorter upstream diameter length compared with an equivalent orifice. As with the orifice meter, the reference average flow velocity V_{ave} of a fluid flowing with a density ρ can be calculated by

$$V_{ave} = C_d \frac{A_2}{A_1} \sqrt{\frac{2(P_1 - P_2)}{\rho(1-\beta^4)}} \tag{10}$$

where A_1 and A_2 are the upstream and throat section cross-sectional areas respectively.

The ratio of the throat section diameter to the upstream diameter of the venturi is given by β. The pressures upstream and at the throat section of the venturi tube are denoted by P_1 and P_2 respectively.

A noteworthy advantage of the venturi meter, unlike the orifice meter, is that it does not require flow profiling upstream of the meter. On the other hand, unlike the orifice meter, the venturi meter is large in size, typically six diameters long, and more expensive to manufacture. However, it has a limited measurement range of typically 3:1, similar to that of an orifice meter [2].

e) Pitot tube:

The pitot tube is a simple device that allows for the measurement of the flow pressure in a moving fluid. This device is a section of tube that measures the total pressure at the tip and the static pressure at the side of the tube as shown in Figure 15.

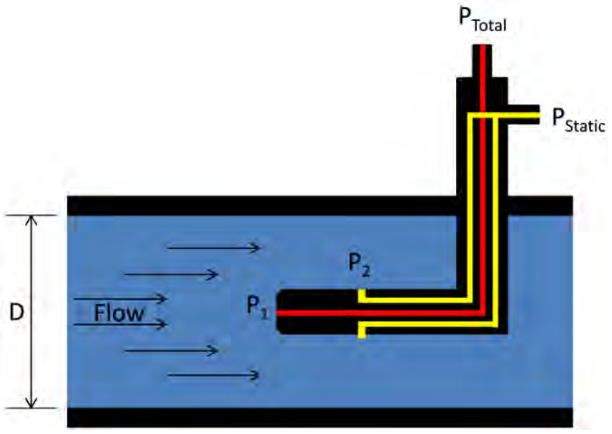

Figure 15: Basic pitot-static tube

Reading this differential pressure and applying the continuity Equation (1) and Bernoulli's Equation (2), allows for calculation of the flow point velocity V of the fluid flowing with a density ρ as indicated by Equation (11),

$$V = C_d \sqrt{\frac{2(P_1 - P_2)}{\rho}} \tag{11}$$

where C_d is the flow coefficient that takes into consideration the pitot tube geometry and the flow condition.

2.3 Site constraints and flow meter criteria

A major constraint for the research was the position of the existing measurement locations. The recommended flow meter would have to be installed at the existing measuring pit where the original orifices were located. This is due to the fact that the CW ducts are usually underground and covered with concrete, inhibiting access to other potential measurement locations.

The permissible included angles between the traverses were obtained with the aid of a CAD model construction of the flow meter pits in Eskom power stations, as shown in Figure 16. The traverse angles were based on the physical constraints around the meter pits.

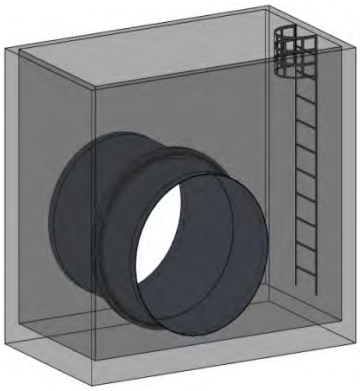

Meter pit CAD model
(PS-01)

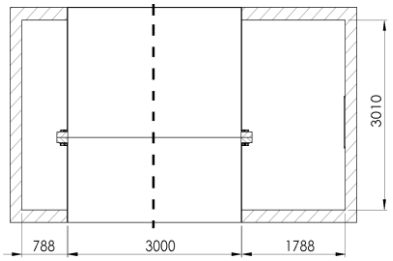

Meter pit top view
(PS-01)

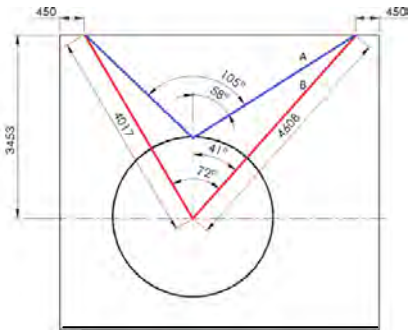

Meter pit radial cross-section
(PS-01)

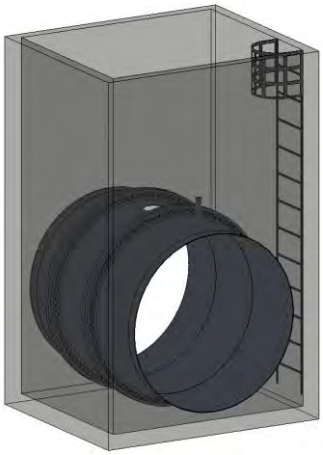

Meter pit CAD model
(PS-02)

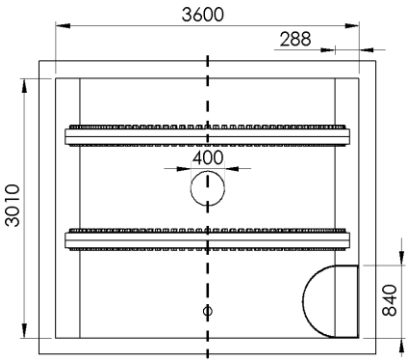

Meter pit top view
(PS-02)

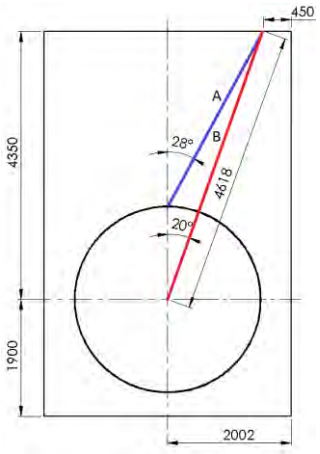

Meter pit radial cross-section
(PS-02)

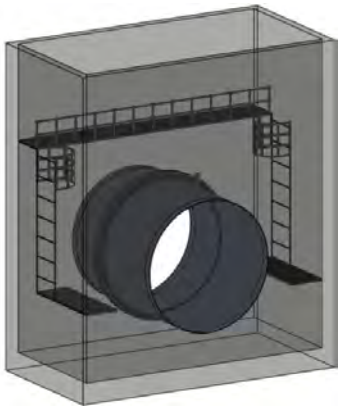

Meter pit CAD model
(PS-03)

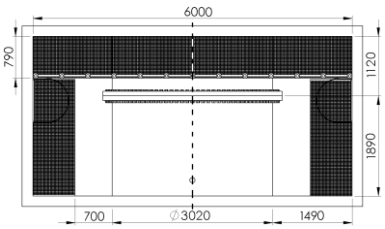

Meter pit top view
(PS-03)

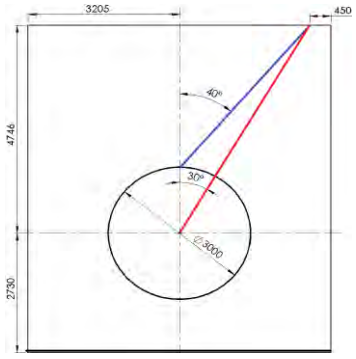

Meter pit radial cross-section
(PS-03)

Figure 16: Meter pit CAD models

On completion of the CAD models, the traversing angles shown in Figure 18 were chosen, where the bending axis definition is described in Figure 17.

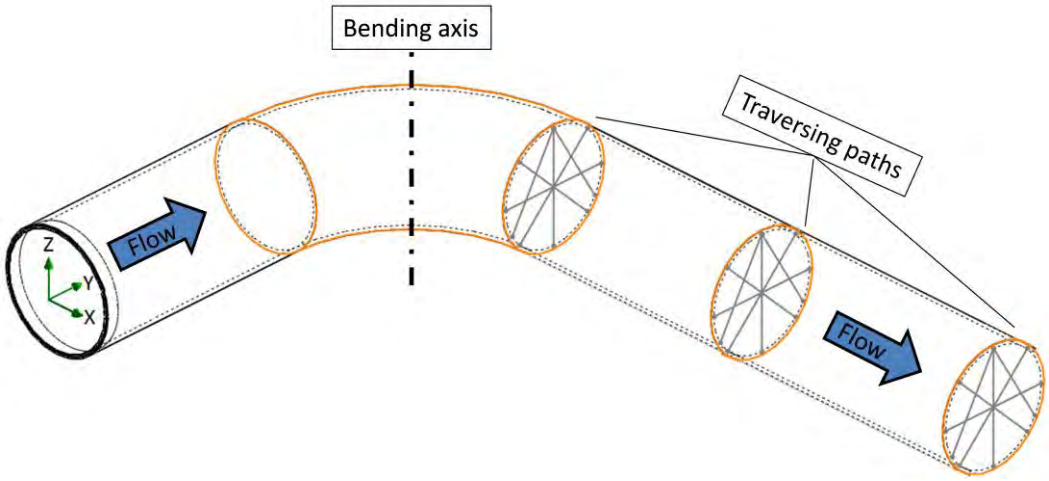

Figure 17: Definition of bending axis

Below are the various traversing paths that were mentioned above.

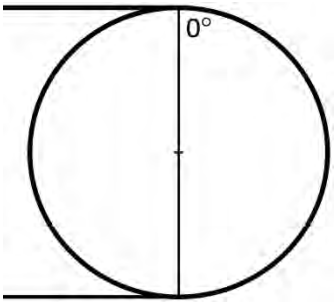

Single traverse parallel to bending axis (0°)

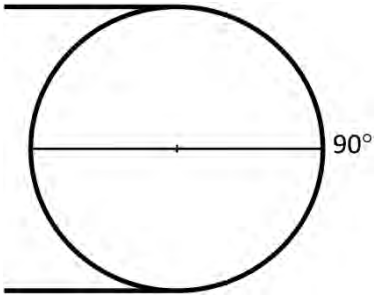

Single traverse perpendicular to bending axis (90°)

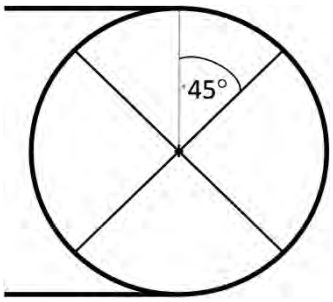

Traverses at ±45° to bending axis

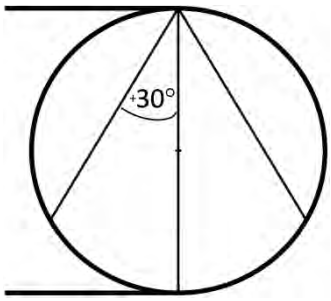

Two chord traverses at ±30° to the bending axis and single traverse parallel to bending axis

Figure 18: Probe traversing paths

It was evident during site visits that most of the power stations did not have taping points along the proposed traversing paths. In order to implement the local flow measurement technique, it might therefore be necessary to introduce tapping points on certain CW ducts. However, some power stations were found to have at least one tapping point that satisfied one of the traversing paths, as indicated in Figure 19 below.

In addition, space for the taping points further limited the geometric profile of the probe to be utilized.

(a) *(b)*

Figure 19: Existing taping point on site (a) at 0° to the vertical (Hendrina PS) (b) at ± 45° to the vertical (PS-04)

The exterior spaces around the CW ducts are covered in concrete, limiting the choice of flow measurement locations. By implication, the developed flow measurement technique had to allow for such constraints.

Figure 20: CW duct covered in concrete (PS-01)

As previously stated, Eskom currently has stretched energy reserves and for that reason the outage time required for the installation, maintenance and removal of the flow meter was an important consideration.

In addition, the following considerations were taken into account when selecting the measuring device:

- The ability of the flow meter to resist blockages due to flow sediment and debris;
- The construction and installation requirements of the flow meter;
- The standardization and calibration of the flow meter.

Other considerations which were less pertinent in this application were the possibility of vandalism and the impact of the device on the environment.

Furthermore, it was noted that every industrial application required a specific and suitable flow measurement device. It was therefore also important to consider the following critical criteria: the flowing medium, density, pressure and temperature. In addition, it was imperative to identify the required: flow rate accuracy, flow rate range, the measurement repeatability, minimum to maximum turndown, hydrodynamic entrance length and economic considerations, referring to initial acquisition costs, maintenance and operating costs.

2.4 Selection of technology

Various types of flow meters were studied with the aim of establishing the most suitable flow meter for application in CW ducts. The study of the various flow meters was further based on the existing technology and not necessarily possible options such as pressure tapings before and after a 90° bend. A summary of the flow meters studied is provided in Table 1, which include the advantages and disadvantages of the flow meters with respect to the CW duct of 3m in diameter

Table 1: Summary of flow measurement techniques

Technique	Flow medium	Uncertainty	Advantages	Disadvantages
Coriolis mass flow meter	Gas and liquid	±0.1 to 0.3%	No pressure loss	Expensive, space constraints (installation)
Electromagnetic flow meter	Liquid	±0.2 to 2%	No pressure loss	Expensive, requires auxiliary power
Ultrasonic flow meter	Gas and liquid	±0.5 to 5%	No pressure loss	Expensive, requires auxiliary power
Gear meter	Gas and liquid	±0.2 to 2%	Medium pressure loss	Moving parts, debris may cause damage
Turbine flow meter	Gas and liquid	±0.15 to 1%	Medium pressure loss	Only low velocity, not practical, moving parts, debris may cause damage
Vortex shedding meter	Gas and liquid	±0.5 to 2%	Medium pressure loss	Complex post-processing
Hot-wire anemometer	Gas and liquid	±0.5 to 1%	Cheap, Low pressure loss	Fragile
Orifice	Gas and liquid	±0.5 to 2%	Cheap	High pressure loss
Venturi	Gas and liquid	±0.5 to 1.5%	Low pressure loss	Expensive, space constraints (installation)
Pitot tube	Gas and liquid	±0.5 to 2%	Cheap	Geometry (insertion tapping), port blockage

While the coriolis flow meter is a universal meter, it cannot be recommended because of site constraints such as lack of adequate space for the U-tube modification.

Like the coriolis meter, the electromagnetic flow meter requires adequate space for installation, hence it too is unsuitable.

The clamp-on-ultrasonic flow meter is relatively easy and quick to install and requires no pipe modifications, unlike the coriolis meter. However, it requires flow conditioning upstream and downstream of the sensors and these flow meters may produce erroneous measurements when installed incorrectly. Therefore this flow meter is not recommended for this application.

The positive displacement flow meter is suitable for most industrial applications but the size of the pipeline needed and a space constraint deem it unsuitable for this application.

One of the major disadvantages of the turbine flow meter is that it is susceptible to damage caused by particulates and debris in the fluid. Although the turbine meter is relatively inexpensive, it would be a challenge to install a flow meter without a multi-unit shut down. In addition, the mechanical and structural parameters of the flow meter prescribe operating velocities, thus limiting its application, so it cannot be recommended in the context of this research.

The vortex shedding meter is accurate when properly calibrated and installed in a clean fluid with a uniform velocity profile. Like the differential pressure flow meters, they reduce the flow cross section area. Vortex shedding meters are also expensive and their sensitive electronic sensors are not practical for very large pipe diameters, three metres in this context. As a result, the vortex shedding meter cannot be recommended in this context.

Due to its fragile sensor, the hot-wire anemometer is suitable only for gas flow application. Again, this instrument is not suitable for this application because the fluid used is water which may contain debris.

The orifice flow meter is relatively cheap but it introduces a permanent pressure drop in the pipeline, thus resulting in an increase in the pumping power required. Furthermore, orifice meters have in the past presented great challenges for Eskom power stations. For this reason, they have been removed, as discussed in Chapter 1.

The venturi flow meter introduces a less significant pressure drop compared with the orifice meter. However, it is more expensive and requires more pipeline modification due to its size. Due to the physical constraints and the challenge of modifying the CW ducts, the venturi is not suitable.

After consideration of physical site constraints, unknown flow profiles and the expected relative cost of implementation, it was decided that the pitot tube flow meter is a suitable option.

2.4.1 Selection of pitot tube

After careful review of the advantages and disadvantages of various meters, it was concluded that the pitot tube was the most suitable flow-measuring device to determine the CW flow rate in the CW ducts. Also taken into account were the physical constraints and the inability to confirm accurately the flow profile at the measurement meter pit on site. The pitot tube is cheaper than most flow meters and requires minimum main line modifications. Installation of these devices can be done online as shown later in Chapter 3.5. In other words, Installation of these devices can be done without shutting down the plant. Furthermore, it is possible to determine the flow profile at the meter pits in at least one plane or axis across the CW duct.

While the pitot tube is an intrusive flow meter, it produces very little permanent pressure loss. Furthermore, it requires neither flow profiling nor major pipeline modifications. An important advantage is that the pitot tube can be installed and serviced online. In addition, it is capable of achieving accurate flow measurements. For these reasons, the pitot tube was selected as the most suitable flow meter to be focused on in this research.

3. Pitot Tube Detail Literature Review

There is a large variety of pitot tubes, with applications for various industries. However, pitot tubes such as the static pitot tube and multiport pitot tube are widely used for both gas and liquid measurements. This chapter presents a deeper study regarding the various types of pitot tubes and their operation.

3.1 Types of pitot tubes

Simple pitot tube and static pitot tube

The simple pitot tube measures only the total pressure in the flow, hence an independent static reading is required to obtain the local flow velocity. Contrary to the simple pitot tube, the static pitot tube measures only the flow static pressure.

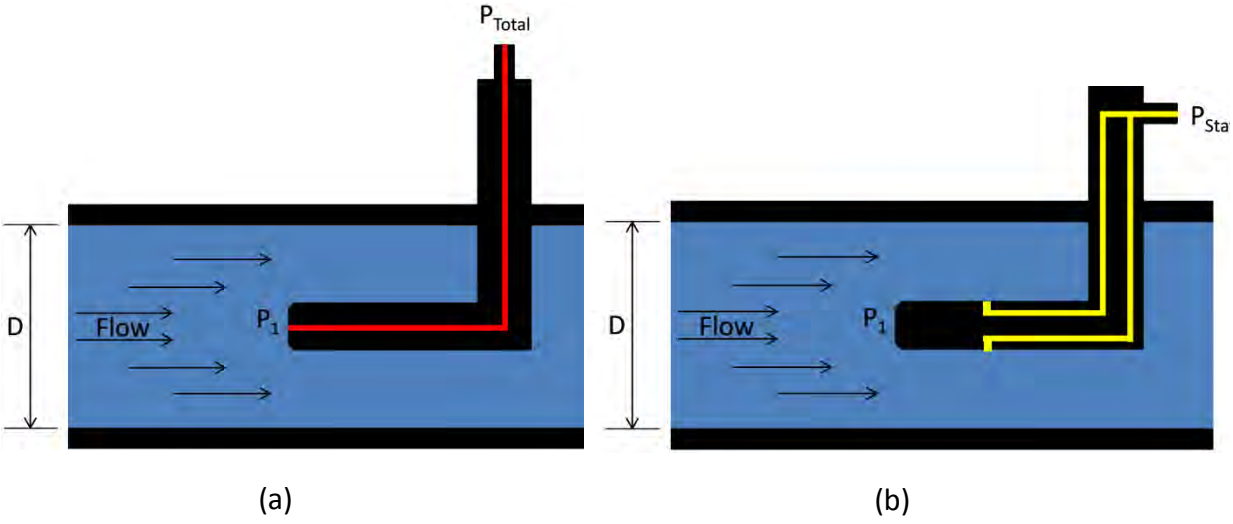

Figure 21: Pitot tube (a) Simple type (b) static type

However, the two are often combined to form a pitot-static tube which measures both the total and static pressure to obtain the local flow velocity.

Pitot-static tube

The most common type of pitot-static tube is one with an ellipsoidal nose, shown in Figure 22, and it is generally unshielded. If aligned properly, these probes can achieve accurate flow measurements. However, they are sensitive and produces errors for unsteady, accelerating or fluctuating flows. This is due to the fact that pitot-static tubes have a significant dynamic resistance to change in flow conditions.

Furthermore, the pressure ports are susceptible to blockage by the suspended particles transported by the fluid.

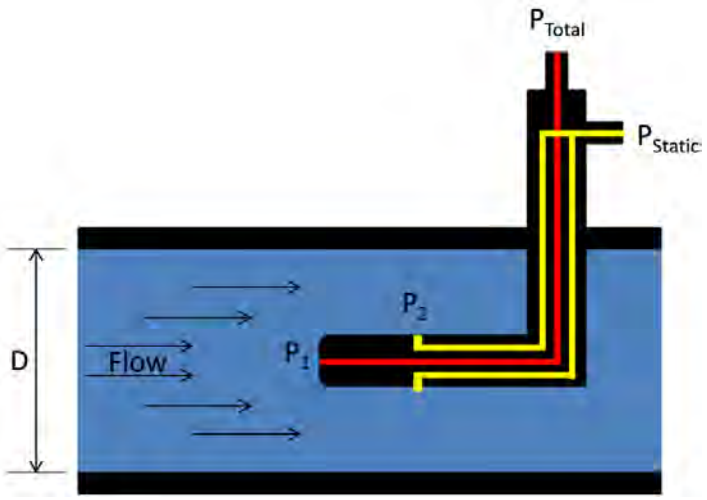

Figure 22: Pitot-static tube

The blockage may result in erroneous measurements, in particular the total pressure readings. Thus it is not recommended that these probes are used in environments contaminated by smoke, dust or silt, for example.

The pitot-static tube principle is extended in the multiport pitot tube, which is essentially a number of pitot-static tubes configured as the multiport pitot-tube with individual pressure transducers, a solenoid arrangement and the averaging pitot tube.

A multiport pitot-tube with individual pressure transducers is likely to escalate the cost of the measurement setup as more equipment is required. Nonetheless, an important advantage of this tube is that it is not necessary to traverse the probe up and down to obtain different local velocities thereby generating a flow profile. In short, this arrangement measures different local velocities simultaneously.

Like the individual pressure transducer arrangement, the solenoid arrangement measures different local velocities without the need to move the probe up and down across the duct, but requires only one pressure transducer.

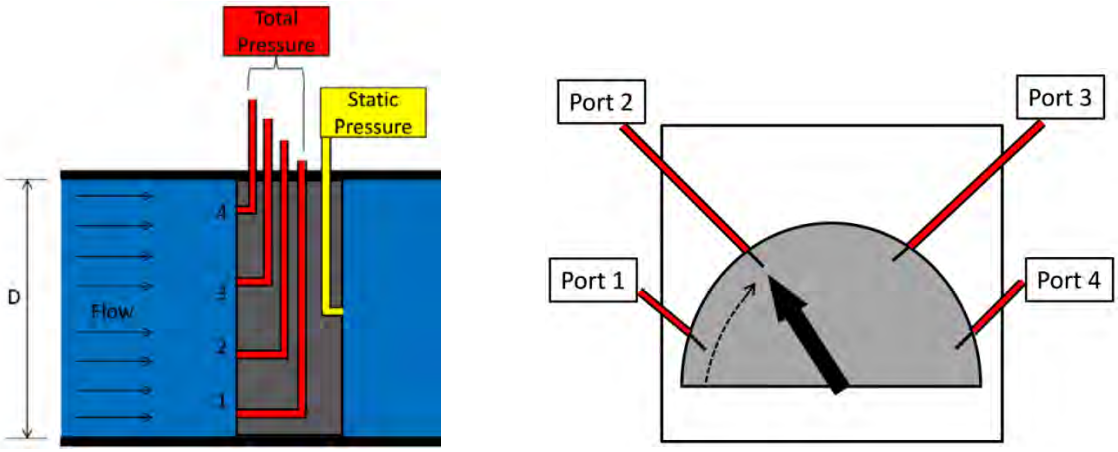

Figure 23: Multiport pitot tube (a) with individual pressure transducers (b) with solenoid configuration

As a result of the solenoid configuration, local velocities are recorded one at a time. The port arrangements for this configuration are exactly the same as in individual pressure transducers, but the physical implementation process differs.

The multiport averaging pitot tube , commonly referred to by the trademark Annubar®, spans the duct cross-section and measures the average velocity based on measurement of dynamic pressure at specified locations in the duct. The working principle of the multiport averaging pitot tube is well documented in literature [6] and was also reported on in Chapter 2.

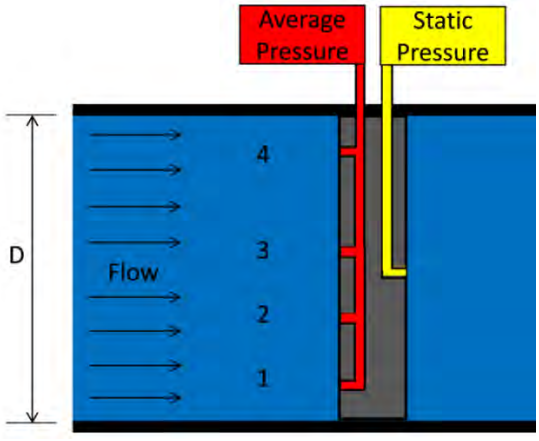

Figure 24: Multiport averaging pitot tube

The multiport averaging pitot tube consists of two chambers. The upstream chamber has multiple pressure-sensing ports to measure the average total pressure; single or multiple series ports measure the downstream pressure of the probe stem, as shown in Figure 24.

The cross-sectional area is divided into a number of equal areas. The upstream sensing ports of the multiport averaging pitot tube are placed at the centroid of these areas on both sides of the symmetric axis.

The shape of the multiport averaging pitot tube can differ from cylindrical to square with rounded corners. The square with rounded corners or the diamond shape, aids to counteract the boundary layer separation problems that are associated with cylindrical-shaped multiport averaging pitot tube. In other words the point of separation remains constant for large range of Reynolds numbers. The multiport averaging pitot tube has the advantage of producing a pressure difference which is slightly larger than simply the difference between total and static pressure, i.e. it is more sensitive. However, multiport averaging pitot tubes require specific calibration coefficients which are sometimes Reynolds-number dependant.

Type 'S' probe

As stated above, pitot-static tubes are not recommended for use in a dusty environment. By contrast, use of the type 'S' (Stauscheibe) probe, which is also referred to as the reverse pitot-static probe, is recommended in applications such as smoke stacks. This probe consists of two impact holes, made of stainless steel, located at 180° to each other as shown in Figure 25 below.

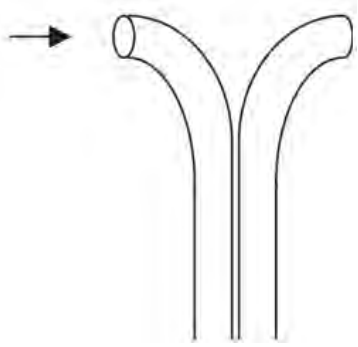

Figure 25: Type S probe

The hole facing the flow measures the total pressure while the other hole, which is aligned with the downstream direction of the flow, measures the static pressure.

Kiel probes

Unlike the pitot-static tube, the Kiel probe is a shield flow measurement probe that determines only the total pressure of the flow. The shield causes these probes to be insensitive to yaw and pitch. Kiel probes share the same disadvantages as pitot-static tubes because the operating principles of these tubes are similar.

Although there is a plethora of types of pitot tubes, Figure 26 shows only some of the measurement probes that were available during the experiment phase of this research.

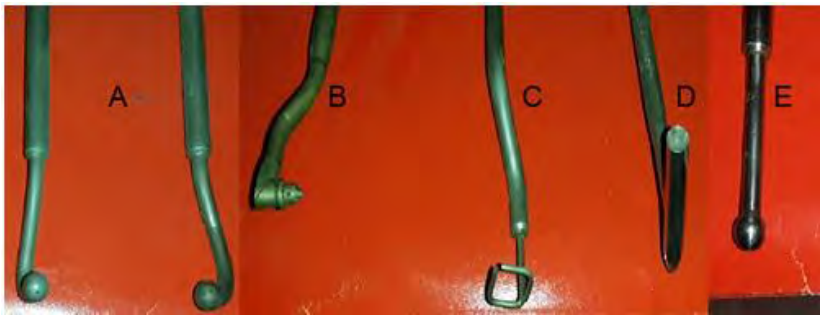

Item	Velocity measurement probe description	Function
A	Five-hole spherical head probe	Flow direction, static and total pressure measurement
B	Five-hole cone probe	Flow direction, static and total pressure measurement
C	Claw probe	Flow direction
D	Kiel probe	Total pressure measurement
E	Cylindrical five-hole spherical probe	Flow direction, static and total pressure measurement

Figure 26: Different types of velocity measurement probes

Figure 27 shows typical shapes for other pitot tubes that are utilized in industry.

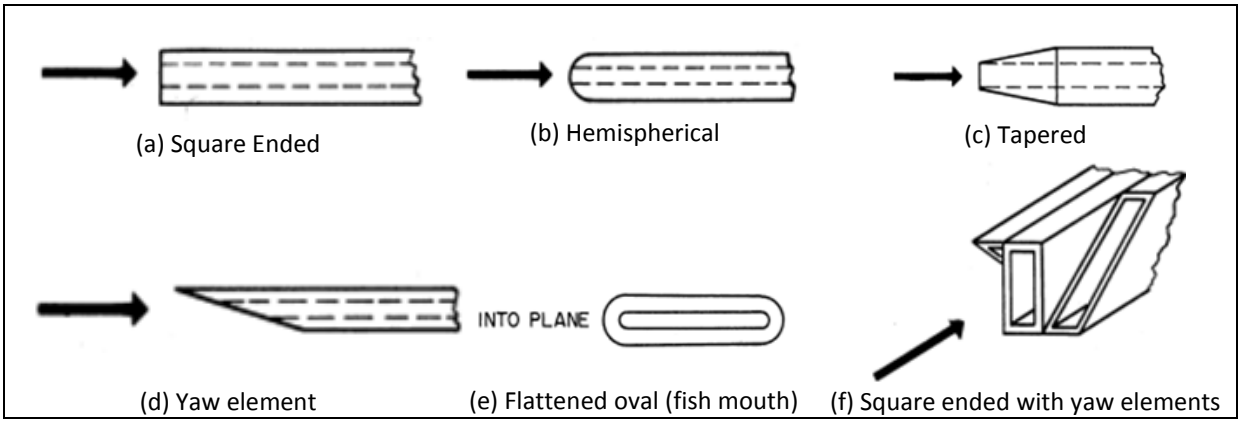

Figure 27: Typical head shapes for pitot tubes [7]

3.2 Pitot tube design considerations

Pitot tube design considerations aim at avoiding numerous corrections to the flow rate measurements. These considerations also provide the necessary mechanical criteria to ensure the structural integrity of the probe.

3.2.1 Probe geometry

The focus will be on pitot-static tubes with a cylindrical head attached in a perpendicular manner to a stem which typically passes through the wall of a pipe such as the one shown below, which is based on ISO 3966-2008.

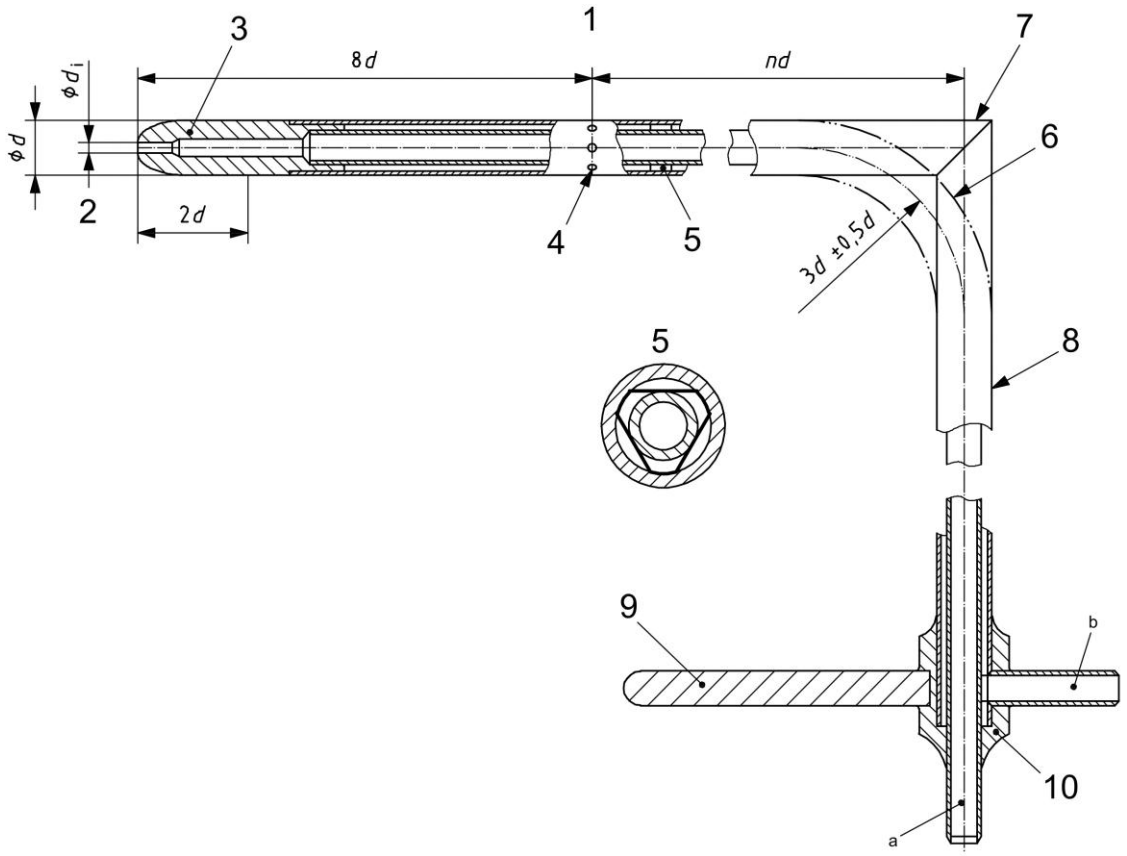

1	Head	4	Static pressure holes	7	Mitred junction	10	Pressure tapping
2	Total pressure hole	5	Spacer	8	Stem	a	Total pressure
3	Modified ellipsoidal nose	6	Alternative curved junction	9	Alignment arm	b	Static pressure

Figure 28: NPL type pitot-tube with modified ellipsoidal nose [8]

The length of the head is generally between 15d and 25d, where d is the head diameter [8].

Static-pressure holes are drilled around the circumference at one or two cross-sections along the head, to ensure that in the absence of leakage, the registered pressure is transferred through the head and stem to a point outside the conduit. A smaller tube, concentric with the head and stem, transfers the total pressure, registered by a hole facing the flow direction at the tip of an axially symmetrical nose integral with the head, to a point outside the conduit.

An alignment arm, fitted to the end of the stem, facilitates alignment of the head when it is obscured by the conduit wall. The nose (including the total pressure hole) should be shall be aligned with the axis of the pipe.

There are two additional types of pitot tube that have a comparable design, namely the AMCA Type pitot tube and CETIAT Type pitot tube.

The AMCA Type pitot tube has eight equally distributed holes with diameter 0.13d, not exceeding 1 mm diameter, and these holes are away from edges [8]. The CETIAT Type pitot tube has a nose radius r^a=d which is useful only in avoiding cavitation when the pitot tube is used in liquids [8].

There various types of pitot tubes however a cylindrical probe was used in this research. The reason for the selection is that a cylindrical probe has a simple geometry compared to the other pitot tubes. The next chapter and going forward focused on a cylindrical probe.

3.2.2 Probe structural integrity

This section provides a guideline to ensure structural integrity of the probe stem in relation to exerted drag forces and resultant bending moments.

In order to achieve structural integrity, the final probe diameter must be such that the ratio d/D of the pitot tube diameter d to the conduit diameter D does not exceed 0.02. This limits error on the rate of flow which results from the velocity gradient and from the stem blockage effect [8]. However, in difficult flow conditions, a ratio of up to 0.04 may be admissible, provided that the necessary corrections for blockage effect and velocity gradient are made. This limit value may indeed be necessary for the avoidance of vibration of the tube in very high velocity flows.

In the case of a cylindrical probe constructed from a material with a yield strength σ_y and a thickness *t,* it is possible to estimate and recommend the minimum outer radius of the probe to avoid a catastrophic failure in a fluid with a mass density ρ. To achieve this, it is necessary to determine the maximum projected area of the stem of the probe, the drag force acting on the probe and the resultant bending moment.

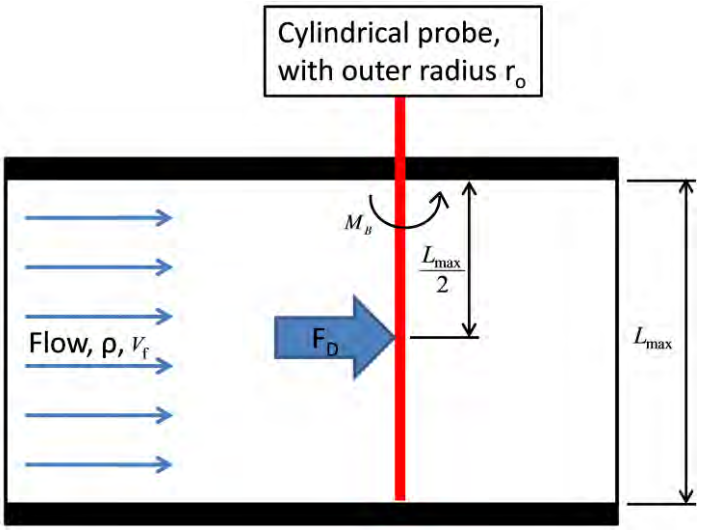

Figure 29: Force diagram

The maximum projected area when the probe is fully inserted through the centre of the duct to the opposite wall can be obtained from

$$A_{\max\_projected} = 2 \cdot r_o \cdot L_{\max} \tag{12}$$

where r_o and L_{max} are the outer radius of the probe and the maximum probe insertion depth respectively. L_{max} can be replaced with the pipe inner diameter D. The resultant maximum drag force acting on the probe for a given average flow velocity V_f is defined as

$$F_D = C_D \cdot \frac{1}{2} \cdot \rho \cdot A_{\max\_projected} \cdot V_f^2 \tag{13}$$

$$F_D = C_D \cdot \frac{1}{2} \cdot \rho \cdot 2 \cdot r_o \cdot L_{\max} \cdot V_f^2 \tag{14}$$

where C_D is the drag coefficient of the geometry of the probe body. The coefficient is often dependent on Reynolds number, but for a cylinder in fully turbulent flow, an average value of 1.2 can be used [3].

An approximate approach was taken to determine maximum bending moment on the probe. This was achieved by applying the drag force at the midpoint of the probe when fully inserted through the centre of the duct to the opposite wall. A more robust approach would be to assume some flow profile and integrate this over the length of the probe. An overly-conservative approach would be to apply the drag force at the tip of probe.

$$M_B = F_D \cdot \frac{L_{\max}}{2} \tag{15}$$

By substituting Equation (14) with Equation (15), the bending moment on the probe becomes

$$M_B = C_D \cdot \frac{1}{2} \cdot \rho \cdot r_o \cdot {L_{\max}}^2 \cdot {V_f}^2 \tag{16}$$

Equation (17) can be used to determine the second moment of area of an annulus (I) which basically measures the resistance to bending of the cross-section of a geometry.

$$I = \frac{\pi\left(r_o^4 - r_i^4\right)}{4} \tag{17}$$

By applying safety factor N_{sf} to the yield strength of the material, the allowable σ_B is represented by Equation (19)

$$\sigma_B = \frac{\sigma_y}{N_{sf}} \tag{18}$$

$$\sigma_B = \frac{M_B y}{I} \tag{19}$$

By substituting Equation (16) with Equation (17), the allowable σ_B, for $y=r_o$, becomes

$$\sigma_B = \frac{4C_D \cdot \rho \cdot r_o^2 \cdot L_{\max}^2 \cdot V_f^2}{\pi\left(r_o^4 - r_i^4\right)} \tag{20}$$

Since $r_i = r_o - t$, the maximum bending stress on a probe traversed all the way to the opposite duct wall can also be represented as

$$\sigma_B = \frac{4C_D \cdot \rho \cdot r_o^2 \cdot L_{\max}^2 \cdot V_f^2}{\pi\left[r_o^4 - \left(r_o - t\right)^4\right]} \tag{21}$$

Equation (21) can be manipulated to solve for the minimum outer radius of the probe. Figure 30 is an illustration of Equation (21) whereby it shows the relationship between the minimum probe outer radius for given wall thickness t and average flow velocity V_f.

For illustrative purposes of Equation (21), consider a probe with a yield strength of σ_y = 100MPa, N_{sf} of 2 [9] and corresponding allowable bending stress of σ_B = 50MPa, and with water flowing in a 395mm pipe at an average velocity V_f.

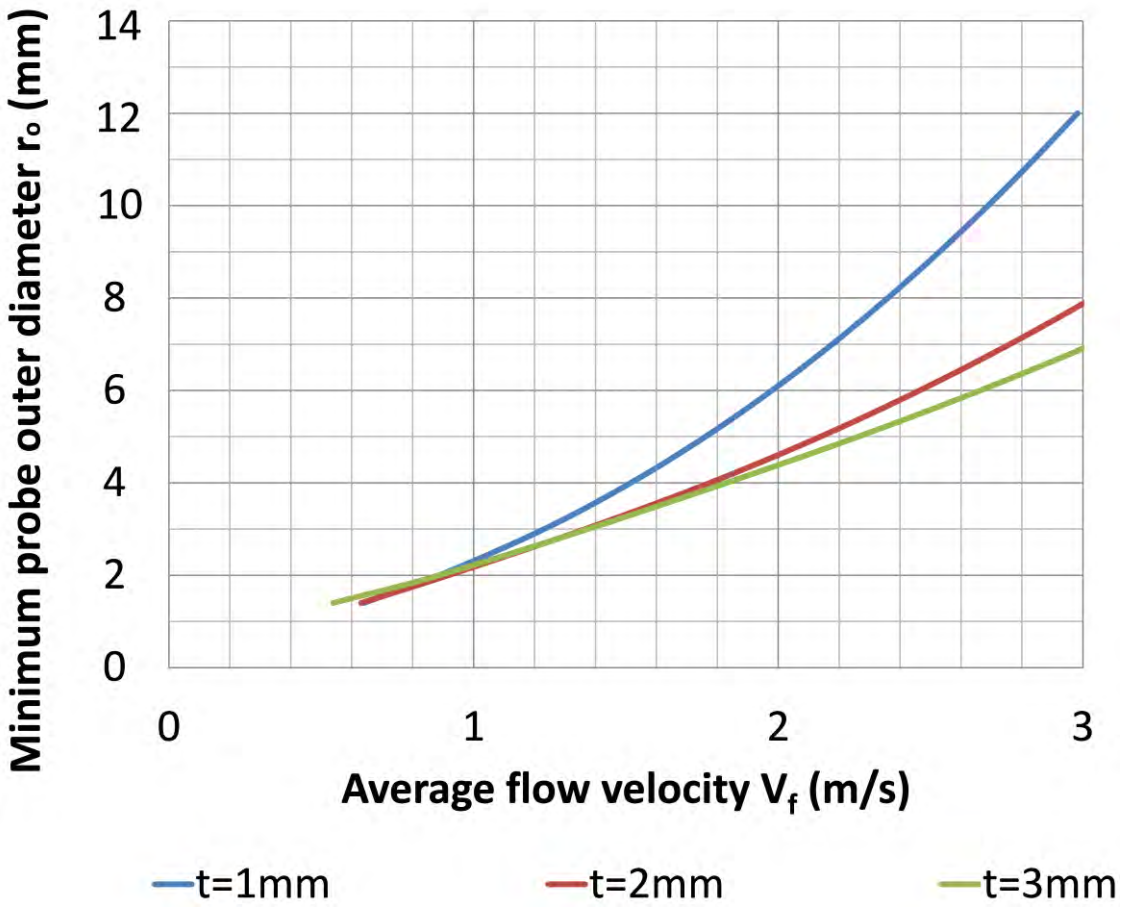

Figure 30: Required probe outer radius vs. average flow velocity

The plots in Figure 30 show that for a given σ_y, the size of the required minimum outer radius of the probe r_o, to avoid mechanical failure, decrease with an increase in the wall thickness of the probe.

3.3 Flow measurement uncertainty

A flow rate measurement cannot be one hundred percent accurate owing to certain parameters with an unknown influence on the flow rate measurement. Two methods are used to evaluate the individual components of an uncertainty. These are Type A and Type B evaluations. The former uses a series of readings from statistical methods and the later uses other methods such as engineering judgement [10]. The sources of uncertainty are sometimes classified as random or systematic and no corrections can be made to remove the random components of uncertainty [10].

These parameters generally influence the measuring principle of the device. The origins of the errors include the following:

- the behaviour of the instruments in a disturbed flow;
- the number and position of the measuring points;
- the methods of integration used;
- flow alignment; and
- probe vibration.

It will be shown later, in Chapter 8.4 of this report, that the vibration of the probe introduces outlying velocity measurements. These outlying measurements distort the velocity profile, thus causing flow rate measurement errors.

It is possible to reduce the uncertainty of a measurement by increasing the number of radial measurement points. However, swirls around the pitot tube may affect its operation and there is unfortunately limited information pertaining to the effect of the swirling flow on pitot tubes [11].

The method used to properly align the probe to flow is that of rotating the probe stem so that the two static pressure taps read the same pressure. This means that the probe is aligned with the direction of the flow [11]. The uncertainty of the flow measurement attributed to swirl is assumed to increase with the swirl angles. In the absence of precise data, the uncertainty percentage resulting from swirls is assumed to be ±5 % of the maximum value, in degrees, of swirl angle observed in the measuring section. It is worth mentioning that the uncertainty becomes less reliable for swirl angles above 20° [11].

3.4 Calibration

The accuracy of a local velocity measurement is affected by elements such as the blockage effect, the velocity gradient, turbulence and the head loss. These require correction factors which are not always exactly known. Such corrections are often only applied only when perfectly accurate measurement is required or when errors are extensive [8].

The pitot tube requires calibration in order to account for instrument errors, probe angle of attack, shape of probe (blockage effects), and near wall measurements. In this instance, the uncertainties of the inputs into the velocity-area integration method must be recorded and considered.

The possible sources that contribute to the uncertainty of measurement include:

- Calibration uncertainty of the pressure transducer;
- Insufficient averaging time of the transducer signal;
- Insufficient settling time after movement of the probe; and
- The temperature of the fluid which is needed in order to determine its density and dynamic viscosity.

The blockage factor is generally defined as the ratio of the area blocked by the probe to the actual cross-sectional area of the pipe. Thus, the blockage factor F_b can be calculated by

$$F_b = \frac{4}{\pi}\left(\frac{d}{D}\right) \tag{22}$$

Depending on the diameter d of the probe relative to the pipe diameter D, the blockage effects can introduce significant errors into the measurements. This is attributed to the fact that the flow velocity increases locally at the point of measurement due to the reduced cross-sectional area. Equation (22) also holds for L-type probes.

3.5 Installation and operation

It is important that care be taken to avoid locating the traverse plane downstream of any adjustable fitting for which the geometry may change (e.g. a flow control valve), especially if several different flow rates have to be measured [11]. Swirls have an enormous effect on the response of pitot-static tubes and may persist over extended distances. For that reason, whenever possible, the traverse plane should not be downstream of a swirl-inducing configuration [11].

Where this is impossible, a device such as a flow straightener can be used to improve flow conditions. However, when there is reason to believe that the flow is asymmetric, the minimum number of radii where measurements are taken should be six.

In order to determine the alignment of the probe with the local direction of the flow, the probe stem can be rotated about its axis so that the static pressures from the pressure taps are equal [11]. As already stated in Chapter 2.4, the pitot tube can be installed online through an installation process called hot tapping.

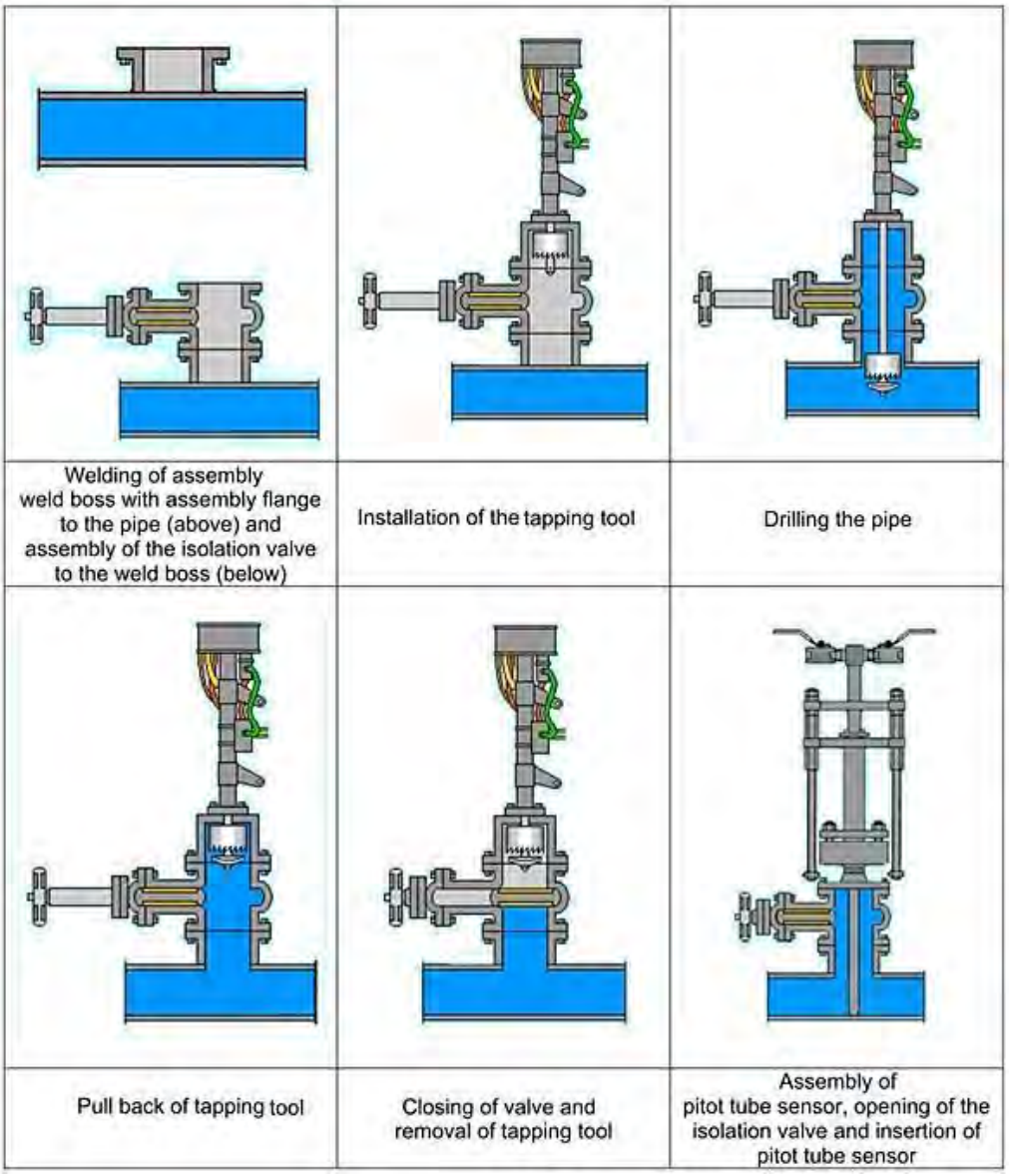

Figure 31: Hot-tapping process [12]

This process involves drilling through a main pipe in an operation without causing leaks. This is achieved by drilling through a fitting with an isolating valve. The fitting is generally welded on to the pipe, resulting in the fitting's forming part of the traversing mechanism of the pitot tube. This concept is shown in Figure 31.

Caution should be applied during this the hot tapping process as debris resulting from the drilling process could damage the condenser or CW pump impeller. It is therefore recommended that the Eskom standard for hot tapping of cooling water system ducts be utilized [13].

The pitot tube does not require any special maintenance, but it is important to ensure, before and after the measurements, that the following points in particular are tested [8]:

- the pressure sensing holes and their connecting tubes are not blocked;
- there is no leakage between the chambers inside the pitot tube which receive the total pressure and the static pressure;
- the tube has not been bent or its nose damaged;
- the tube is clean; and
- the head of the pitot tube is absolutely perpendicular to the supporting stem.

Since the determination of the velocity is related to the differential pressure, it is imperative that the connections:

- to the pressure gauge are as short as possible;
- are absolutely leak-tight (porous or cracked rubber tubes etc. are not permissible); and
- ISO 2186 provides additional requirements for consideration.

4. Flow Phenomena in Ducts

The fundamental principles governing the flow of fluid in a pipe should be understood before a local flow meter can be used with confidence. Relevant fundamental principles include the difference between laminar and turbulent flow, Reynolds number and the importance of the velocity profile of the flow.

4.1 Flow profiles

Flow meters are generally used to measure flow velocities, either as local or as bulk velocities. Local velocity refers to velocity at a point across the diameter of a particular pipe whereas bulk velocity is an averaged velocity of the fluid across the cross-sectional area of a pipe. This distinction makes it clear that local velocities provide more information on the shape of the flow profile and may indicate any abnormalities in the flow pattern across the diameter of a pipe. It is therefore important to understand the type of flow velocity that a particular flow meter can measure.

Fluid motion in a pipe can be characterized as laminar, transitional, or turbulent.

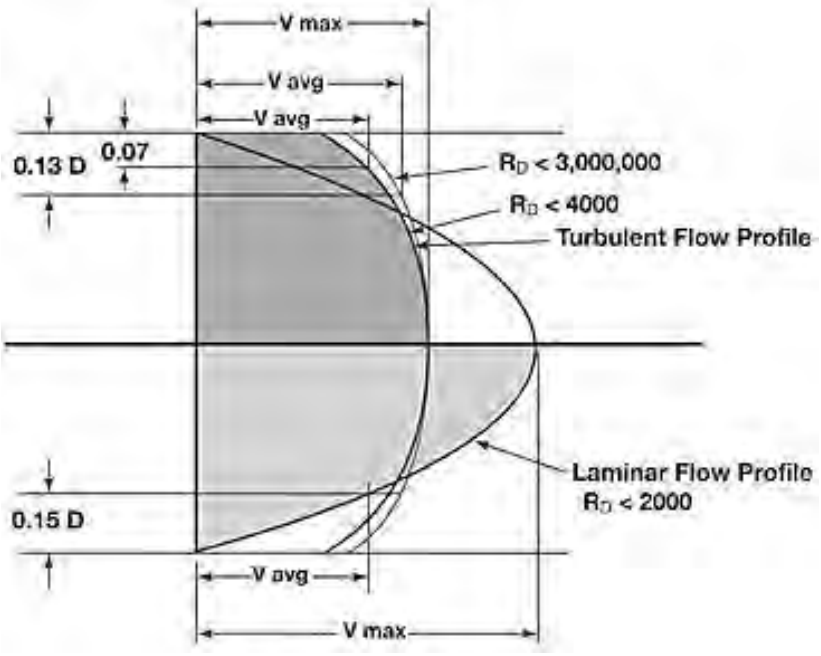

Figure 32: Velocity profiles in laminar and turbulent flow [14].

In laminar flow, the fluid travels as parallel layers (known as streamlines) that do not mix when moving in the direction of the flow. If the flow is turbulent, the fluid does not perfectly travel in parallel layers, but moves in a disorganized manner with only the average motion of the fluid being parallel to the axis of the pipe [2].

Unlike what occurs in laminar flow, the expressions for the velocity profile in a turbulent flow are based on both analysis and measurements. As such, these expressions are semi-empirical in nature with constants determined from experimental data [3].

The working fluid velocity plays a major role in determining the flow regime of fluid inside a pipe. This is illustrated by the introduction of a dimensional number called the Reynolds number, which can be defined as the ratio of the inertial forces of the fluid to the viscous forces of the fluid, given by

$$\mathrm{Re}_D = \frac{V_{avg} D}{\upsilon} = \rho \frac{V_{avg} D}{\mu} \tag{23}$$

where: V_{avg} is the fluid flow average velocity; D is the duct inner diameter; v is the fluid kinematic viscosity; and ρ and μ are the density of the fluid and its dynamic viscosity respectively. The inertial forces are a function of the fluid flow velocity and duct geometry whereas the viscous forces are directly influenced by the dynamic viscosity and density of the fluid medium or kinematic viscosity.

In the flow of fluid through a completely filled conduit, gravity does not affect the flow pattern, nor does the pressure if the fluid is considered incompressible.

Laminar flows in a duct can be defined as flows with insignificant disturbances in the flow motion. They are typically characterized by smooth streamlines and occur when $Re_D < 2300$ in pipes. By contrast, turbulent flows can be defined as flow with disturbances and non-uniform fluid motion. They are typically characterized by velocity and occur when $Re_D > 4000$ in pipes [3].

Most flows encountered in practice are turbulent with typical speeds of $2\,{}^{m}/_{S}$ for water in pipes. The calculations and analysis conducted in this research validate the proposed notion that turbulent flows exist in cooling water ducts at an operating temperature and pressure of 45 ℃ and 145 kPa respectively. The following calculation, using data collected from existing cooling tower performance tests confirms this statement.

It follows that the dynamic viscosity and density of the water is $\mu = 596.072 \times 10^{-6} Pa.s$ and $\rho = 990.232\ {}^{kg}/_{m^3}$.respectively [15]. Given the duct diameter, $D = 3m$ and the typical average flow velocity, $V_{avg} = 2\ {}^{m}/_{S}$, it was found that the Reynolds number is

$$\begin{aligned} \mathrm{Re}_D &= \rho \frac{V_{avg} D}{\mu} \\ &= 990.232 \frac{(2)(3)}{596.072 \times 10^{-6}} \\ &= 9.96 \times 10^{6} \end{aligned} \tag{24}$$

Symmetric or uniform profile can be described as a flow pattern that is similar near a given axis of the cross-sectional area of a pipe. Such profiles can be created by flow straighteners such as a Zanker, a Tube bundle or an Étoile straightener as shown below.

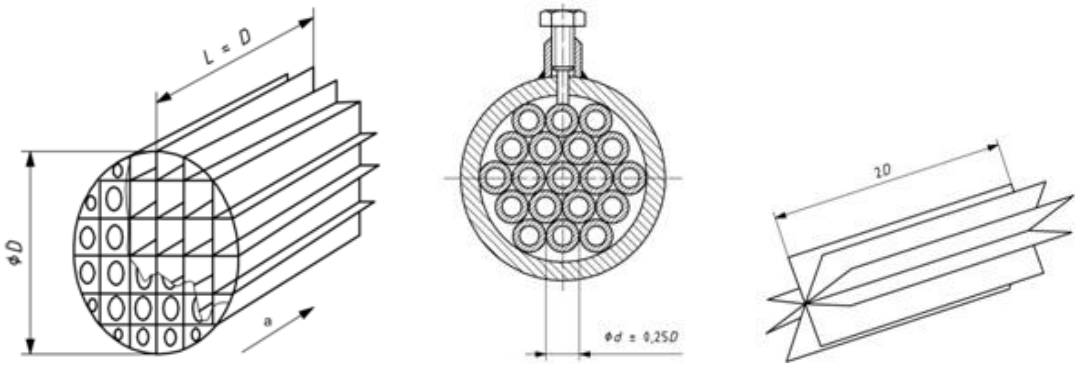

(a) (b) (c)

Figure 33: Flow straightener [11] (a) Zanker (b) Tube bundle (c) Étoile

Asymmetrical or non-uniform flow profiles can be attributed to flow disturbances that exist in the flow path such as a bend or valve which distorts the upstream profile, thus changing the shape of the downstream profile. Other components such as pumps can also generate swirls or distortions to the upstream profile. This phenomenon is however not desirable as already in mentioned Chapters 3.3 and 3.5 of this report.

Fully developed flow profiles for laminar and turbulent flow are flow profiles that are obtained at the end of a relatively long pipe, which eradicate any changes to the flow profile caused by pipe bends and fittings [2].

In order for the performance of a differential pressure flow meter such as an orifice to be credible, flow conditions should be fully developed and the velocity profile known (or assumed symmetrical).

Understanding and quantifying the internal surface roughness is an important aspect when studying flows in conduits. In particular, the surface roughness effects are pronounced in turbulent regimes, other the hand, neglected for lamina regimes. Equation (24) shows that the flow conditions on site are turbulent hence the effects of surface roughness on the flow profile were studied.

With that in mind, the CW ducts are steel liners which are 8mm to 12mm thick and encased in concrete. As a consequence, an internal inspection of the duct could not be conducted. Nonetheless the effects of the relative roughness on the flow profile were studied. This study is shown later in Chapter 7.5.

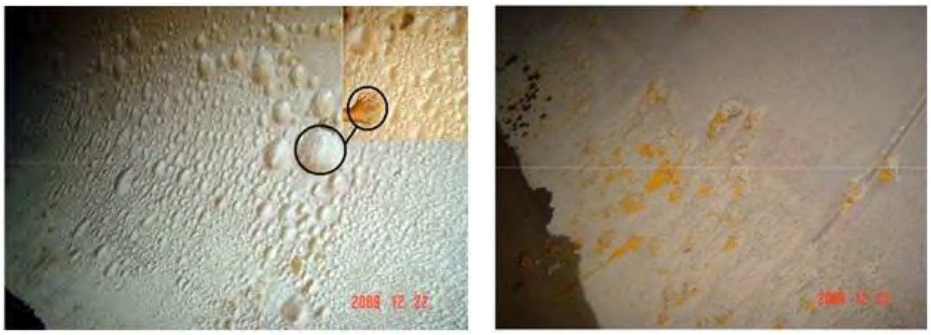

Figure 34: Blistering of Copon EP 2300 coated surfaces inside CW duct (Lethabo Power Station) [16]

The domes on the inner surface of the CW duct were created by Sulphate Reducing Bacteria (SRB) which corroded the steel ducts and contributed to surface roughness and more debris. These bacteria use sulphur and not oxygen for respiration thus reduce the sulphur content in the CW water.

During an inspection done in 1998 at Lethabo power station CW ducts, the blisters were recorded to have a diameter in excess of 350mm. These blisters were generally found to be filled with a mixture of CW water and superficial corrosion particle off the CW duct wall. Furthermore in another inspection conducted at Lethabo power station during December 1992 and January 1993, the depth of the pitting on the CW ducts were recorded as 2 to 3 mm [17]. In addition, inspections conducted in the CW ducts at Duvha power station, recorded the depth of the pitting of the order of 1 to 5 mm [18].

The SRB or scale build up would be a concern if the flows in the CW ducts were laminar because a laminar flow profile is unaffected by the roughness of the pipe wall. However it is later shown that flows in the CW ducts, during normal operation, are turbulent in nature hence the effects of the CW duct inner surface roughness were documented in Chapter 7.5.

In turbulent flow, inertia forces are dominant, pipe wall effects are more and the velocity profile of the flow is flatter, with the velocity at the centre being about 1.2 times the mean velocity [2]. The exact flow profile in a turbulent flow depends on pipe wall roughness and Reynolds number. Unlike what happens in laminar flow, the friction factor in turbulent flow is a strong function of surface roughness [3].

4.2 Disturbance due to 90° bends

The CFD modelling tool used in this research was SolidWorks 2013 Flow Simulation. It is understood that there are better CFD packages in the market however for purposes of this research, the chosen CFD modelling tool was deemed sufficient. The CFD analysis conducted in this study was to obtain indicative flow profiles that exist in the CW dust.

The purpose of the CFD simulations was not to predict the flow patterns inside the CW ducts but to rather obtain realistic velocity profile data that could be used in developing the mathematical algorithms. However the mesh size of the CFD model was varied and various Reynolds numbers were considered. This was limited by the computer capability.

In order to verify the CFD model that was developed in this research, the flow profiles and the phenomena that exist in CW ducts were studied. The CFD model was compared to findings in literature that included experimental work.

The study of fluid motion in a pipe bend and corresponding head losses is well documented in [19], [20], [3] and this enabled the comparisons mentioned above. The results obtained from the CFD simulation were used as inputs into the numerical algorithm and it was therefore imperative to gain confidence in the CFD model.

To achieve this, the calculated flow profiles were compared against those in existing studies, one of which was experimental work done by Rütten et al. [21]. They conducted an experiment to investigate the oscillatory phenomenon in separate turbulent flows through a 90° bend with a curvature ratio of one and Reynolds number of 5000 and 10 000.

Figure 35 and Figure 36 have the y-axis set to the time average velocities and the x-axis set to the a ratio of the probe position to the pipe diameter. The inner bend is at *x/D*=0 and the outer bend is at *x/D*=1.

According to the CFD model and the experimental results, the flow profile in the entrance of the bend is different from the profile of a fully developed flow in a pipe.

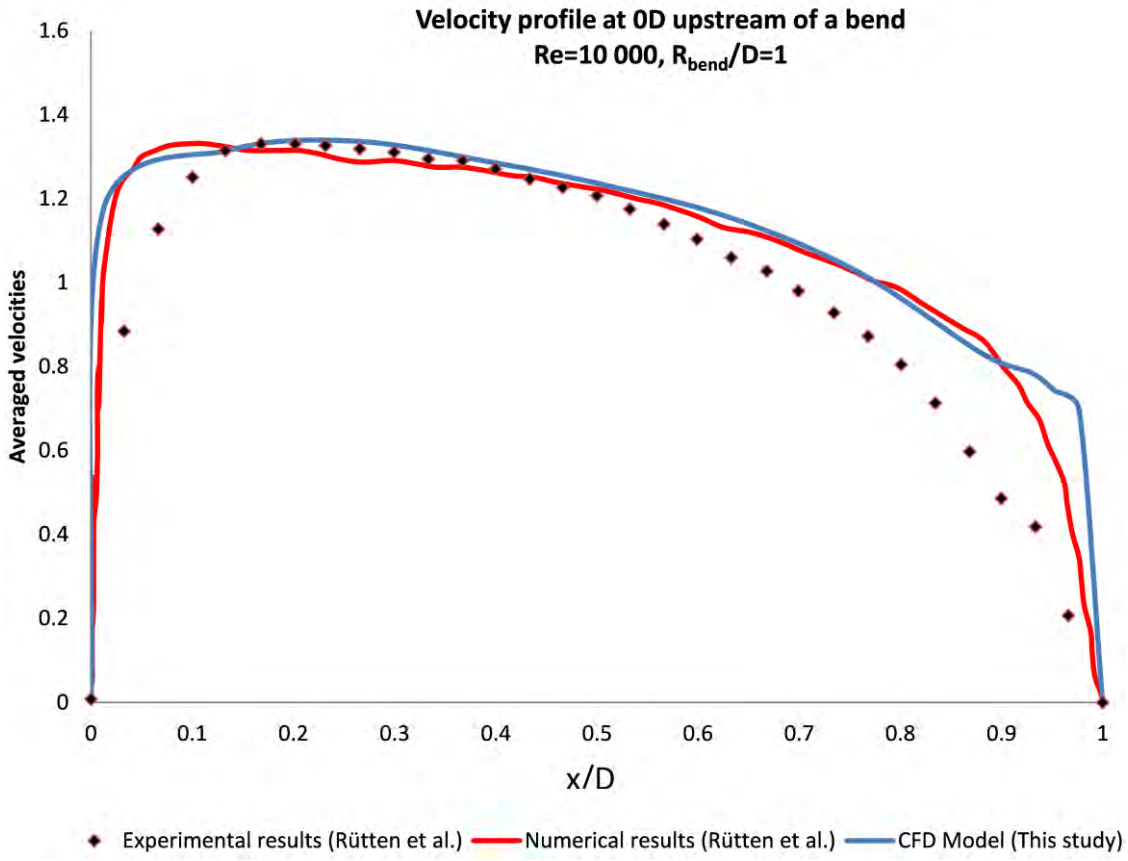

Figure 35: CFD model results (this study) vs. numerical and experimental results by Rütten et al. [4]. (0D upstream of a bend Re=10 000, R/D=1)

As flow enters a bend, the outer side of the bend (*x/D*=1) experiences local flow deceleration whereas local flow velocities are accelerated at the inner side of the bend (*x/D*=0). This means that axial turbulence intensities are higher in the outer side of the bend and lower in the inner side of the bend.

The opposite is true for the flow leaving the bend as indicated in Figure 36.

The results as shown in both Figure 35 and Figure 36 indicate a correlation between the CFD model and work or experiments done by Rütten et al.

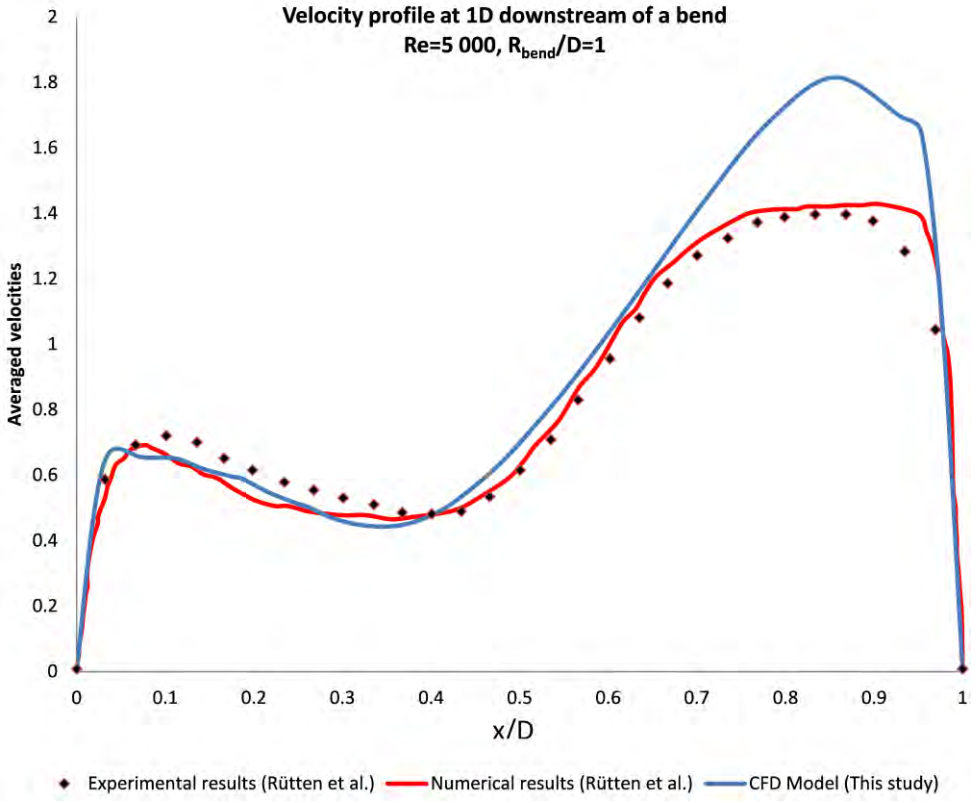

Figure 36: CFD model results (this study) vs. numerical and experimental results by Rütten et al. [4]. (1D downstream of a bend Re=5 000, R/D=1)

Experimental investigations by Rowe [22] also indicate that the fluid accelerates inward as it enters a bend due to the pressure gradient across the bend which aims to balance the centrifugal force generated by the trajectory of the fluid. In this case, the forces act at a perpendicular to the main direction of the flow, distorting the axial velocity profile and transferring the higher velocities to the outer side of the pipe. This is also shown in Figure 36.

The difference between the experimental results and the CFD results can be attributed to the fact that the CFD simulations were forced to be steady while the flow in the experiment may not necessarily be steady. The grid resolution in the CFD models may not perfectly represent the correct physical characteristics or phenomena. Furthermore, the boundary conditions in the CFD model may not be exactly those of the physical experiment.

Rowe [22] performed an experiment to investigate transition flows similar to the flows that were measured by Squire [23]. Squire considered the angle of yaw in relation to the pipe axis and the total pressure. The velocity distributions by Rütten et al, in plane of symmetry and across the pipe, were compared, as shown in Figure 37 and Figure 38.

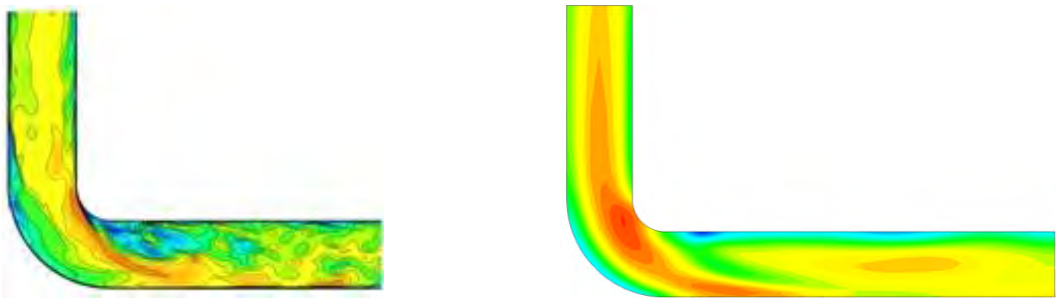

(a) (b)

Figure 37: Instantaneous flow field with the velocity distributions in the plane of symmetry. (Re=5000, R/D=1). (a) Rütten et al. (b) This study

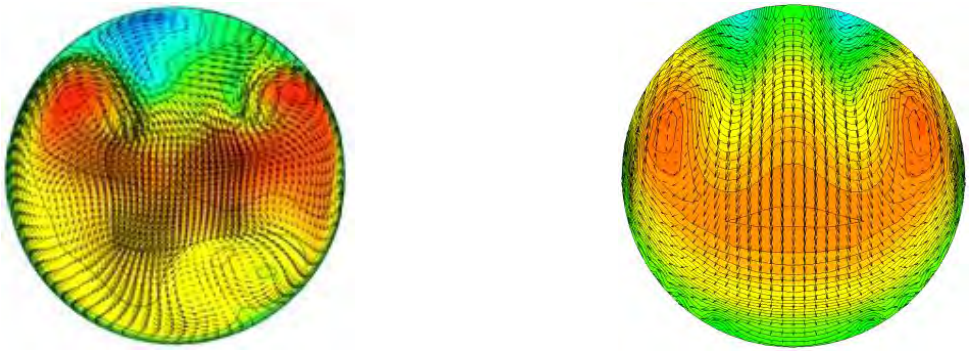

(a) (b)

Figure 38: Instantaneous flow field with the velocity distributions in the cross section at the end of the bend. (Re=5000 and R/D = 1). (a) Rütten et al. (b) This study

where R is the mean radius of the 90° bend.

Moreover, the CFD results as shown in Figure 38 (b) confirm the conclusions made by Rowe [22] and Squire [23]. Figure 40 illustrates the secondary flows resulting from the fluid flowing through the bend. According to the diagrams mentioned, the flow direction is inwards along the pipe boundary and outwards in the core of the pipe, resulting in a maximum flow velocity towards the external arc of the bend [19].

The secondary flows persist in the planes that are perpendicular to the bending axis of the pipe [24], as shown in Figure 39.

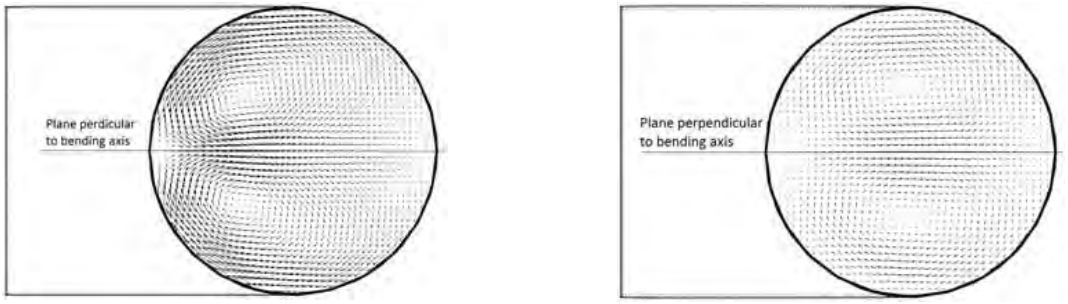

(a) (b)

Figure 39: Secondary flow patterns in the cross section for (Re=5000 and R/D = 1) at (a) 1D after the bend (b) 6D after the bend

It is also evident from Figure 39 that the flow tends to become fully developed further downstream of the bend provided the pipe has a constant cross-section and a bend of constant radius. The recirculation generated by the bend, above and below the plane perpendicular to the bending axis, as shown by Figure 39 (a), is concentrated towards the inner wall of the bend. With distance from the bend, the recirculation shift towards the centre of the pipe as shown by Figure 39 (b).

As a result of fully developed flow, the flow velocities remain constant with distance along the axis of the pipe. The flow in the core of the pipe possesses high velocities and has high momentum and therefore attempts to continue flowing in its initial straight path. This phenomenon can also be illustrated by a flowing river, where the outer bed of the river is deepened due to higher velocities at the outer bank.

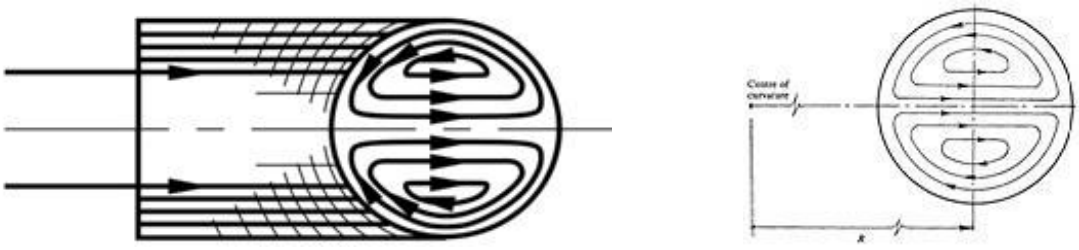

(a) (b)

Figure 40: Secondary flow patterns. (a) Figure 4.77 [19] (b) Figure 1 [25]

In addition, the fluid closer to the top and bottom of the pipe walls moves more slowly than the fluid along the central plane [24]. This is also true for experiments performed by Sudo et al. [26]. These secondary patterns will be present at any distance downstream of a 90° bend up to the next flow disturbance.

It is evident from the figures and explanations provided above that the CFD model used in this research produces results that are consistent with the existing literature. These CFD model results are therefore a true reflection of what is likely to occur in industry and provide reliable input data to the numerical algorithms developed in this research. From the flow patterns shown in the previous figures, it is evident that the maximum flow around a bend exists towards the outer side of the pipe when close to the bend.

5. Algorithms to Calculate Total Flow from Local Measurements

At the outset of this research, it was important to understand the possible flow regimes that might exist in the CW duct in order to analyse and develop mathematical models of fluid flow in pipes. The different flow regimes discussed in Chapter 4 were studied to assist in defining the appropriate methodology of developing a mathematical algorithm and technique to estimate flow measurement uncertainties. With an already calculated Reynold's number of ($Re_D = 9.96 \times 10^6$), which is much greater than 4300, it was concluded that the flow in CW ducts was turbulent. This suggests that the methodology will focus on and investigate techniques suitable for turbulent flow in large pipes.

For symmetric flow there are pre-existing standards such as the Standard for Liquid Flow Measurement [27] to calculate the flow rate through a pipe, where integration techniques, such as Log-linear or Log-Chebyshev techniques, are applicable. In this research, the use of these techniques may be invalid owing to the unknown flow profile. Accordingly, it was necessary to develop an algorithm for flow profiles that might be asymmetrical.

For verifying the algorithms, a symmetric profile was initially considered.

5.1 Symmetric profile

Numerous empirical velocity profiles exist for turbulent pipe flow. Among these, the simplest and the best known is the power-law velocity profile [3] expressed as:

$$\frac{u}{u_{\max}} = \left(\frac{y}{R}\right)^{\frac{1}{n}} \tag{25}$$

where *u* is the average flow velocity, u_{max} is the maximum flow velocity and *y* is the radial points across a pipe with radius *R*, with *y=0* at the pipe outside, and *y=R* at the centre.

Alternatively, Equation (25) can also be represented as:

$$u = u_{\max}\left(1 - \frac{r}{R}\right)^{\frac{1}{n}} \tag{26}$$

where the exponent *n* is a constant that is dependent on the Reynolds number as shown in Figure 41.

It is evident that the exponent increases with an increasing Reynolds number, thus creating a turbulent velocity profile that is fuller than the laminar profile.

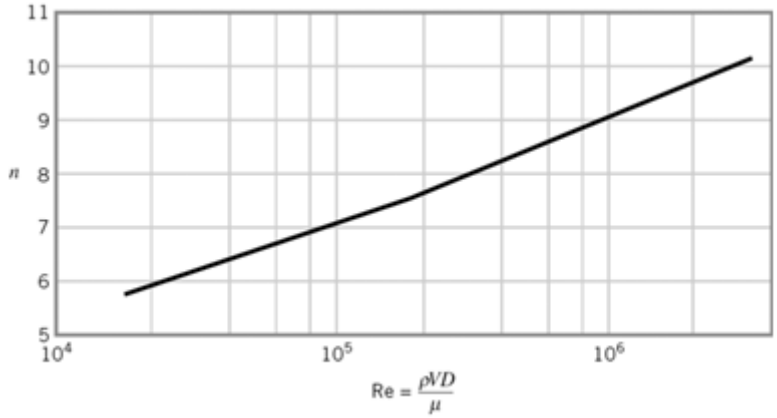

Figure 41: Exponent (n) for power-law equation [3]

The exponent value of $n = 7$ generally approximates many flows in practice [3], thus giving rise to the term "one-seventh power-law velocity profile". The other power-law velocity profiles are shown in Figure 42.

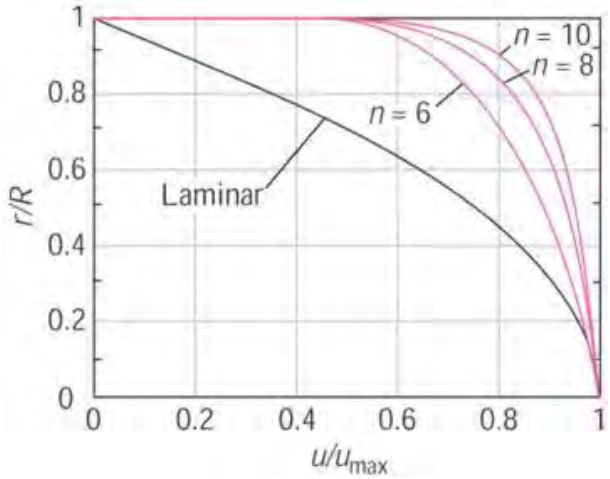

Figure 42: Power-law velocity profiles [3]

Using Equation (25) or (26), it is possible to use the Standard for Liquid Flow Measurement since the pipe cross section may be divided into equal areas. Furthermore, the definite integral of the theoretical flow profile can be estimated by using the Riemann sums and limits. This is simply the area under the graph which is used to calculate the mass flow rate.

There are different types of Riemann Sums: the Left, Midpoint, Right, Lower and Upper Riemann Sum as shown in Figure 43.

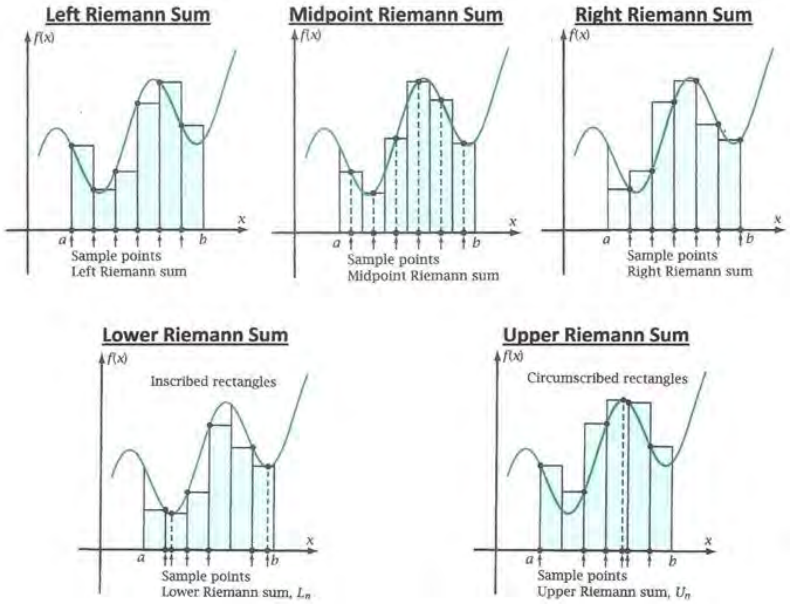

Figure 43: Five types of Riemann Sum [28]

The mathematics developed in this research to apply the Riemann sum was based on the Midpoint Riemann Sum.

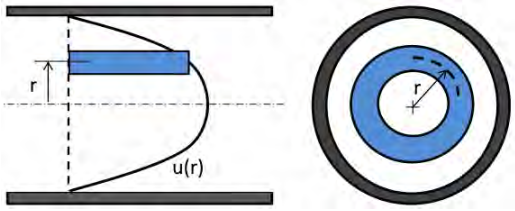

Figure 44: Flow from velocity distribution

The exact total mass flow rate M_{exact} of a theoretical velocity profile given by *u(r)* is

$$\begin{aligned} M_{exact} &= 2\pi \cdot \rho_w \int_0^R u(r) \cdot r \cdot dr \\ &= -\tfrac{7}{4}\pi \cdot \rho_w \cdot R \cdot u_{\max} \left(1 - \frac{r}{R}\right)^{8/7} \Bigg|_{r=0}^{r=R} \\ &= \tfrac{7}{4}\pi \cdot \rho_w \cdot R \cdot u_{\max} \end{aligned} \tag{27}$$

The midpoint rule was used to estimate total mass flow rate for n number of measurement points or annulus segments.

$$M_{estimate} = 2\pi \cdot \rho_w \sum_{i=1}^{n} u(r_i) \cdot \Delta r_i \tag{28}$$

where $u(r_i)\Delta r_i$ represents the height and base of the rectangles and ρ_w the fluid mass density. The annuli were summed to obtain an estimated total mass flow rate.

5.2 Asymmetric profile with traverses crossing the centre-line

Since symmetrical profiles are virtually non-existent in practice, the focus shifted to developing an algorithm applicable to asymmetric flow profiles. Figure 45 indicates a pseudo block diagram aimed at highlighting the methodology and the fundamental equations that were followed to develop the algorithm.

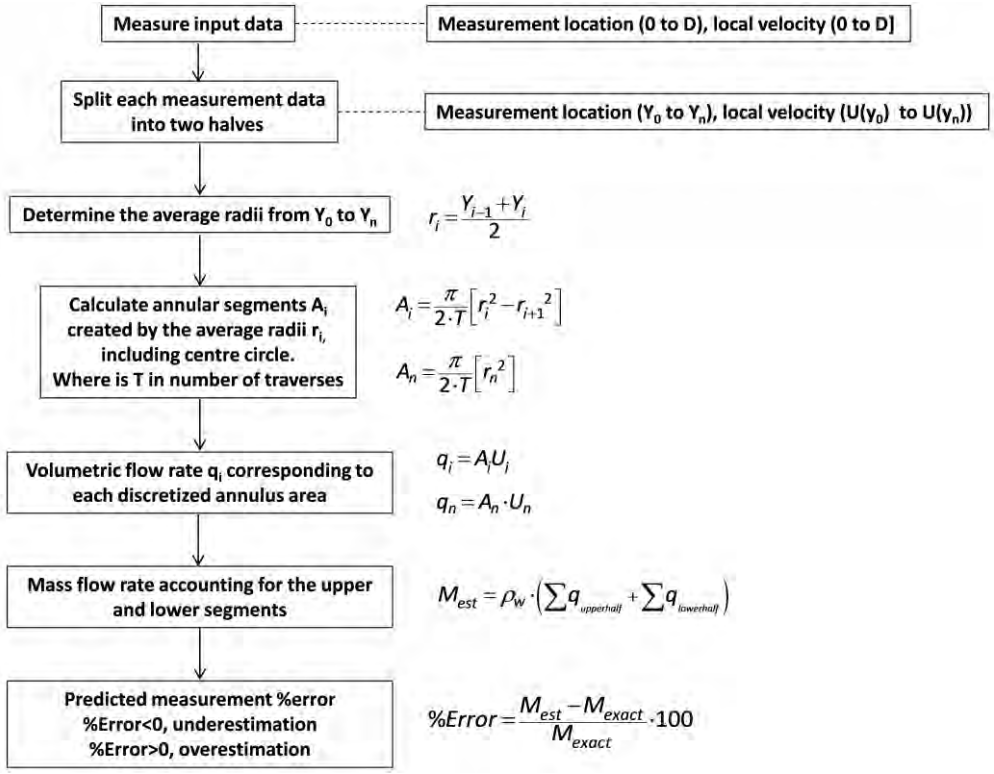

Figure 45: Pseudo block diagram explaining the centre traverse algorithm

This pseudo algorithm is only applicable for traverse through the centre of the pipe diameter. Single and double traverse paths will be described next in more detail.

a) Traverse through the centre parallel to bending axis or perpendicular to bending axis

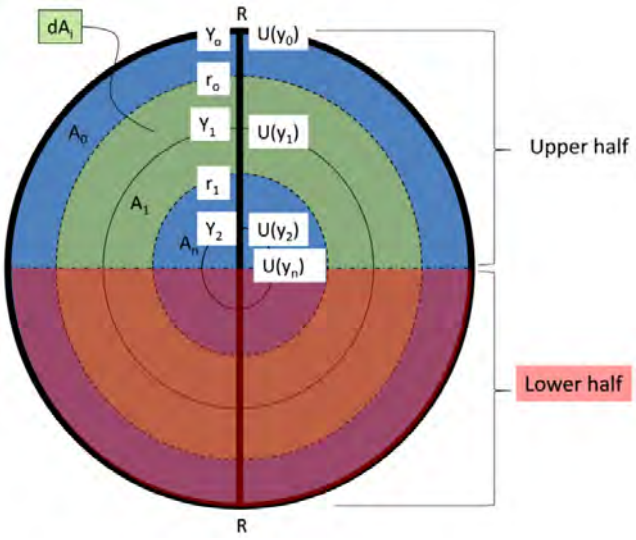

Figure 46: Single traverse through the centre of pipe

In developing this algorithm the pipe was divided into two and the flow rate through each half was calculated. The algorithm takes input data (measurement location and point velocity) and splits the data creating two half segments. A challenge encountered in developing this algorithm was making certain that the centre circle segments are accounted for, irrespective of the input data. This was resolved by using the raw input data to interpolate or force a centre point so as to ensure accountability of the centre flow rate.

The volumetric flow rate of the annulus is computed by multiplying the area of the annulus segment by the corresponding midpoint velocity. The total mass flow through each segment was determined by taking the Riemann sum of all the annuli volumetric flow rates, and then summing the two halves.

The algorithm can accept any spacing between measurement points. This is useful as one often needs to take more samples close to the wall to capture the rapidly changing profile there.

b) Two traverses at 45 ° and 90° to centre line and any included angle

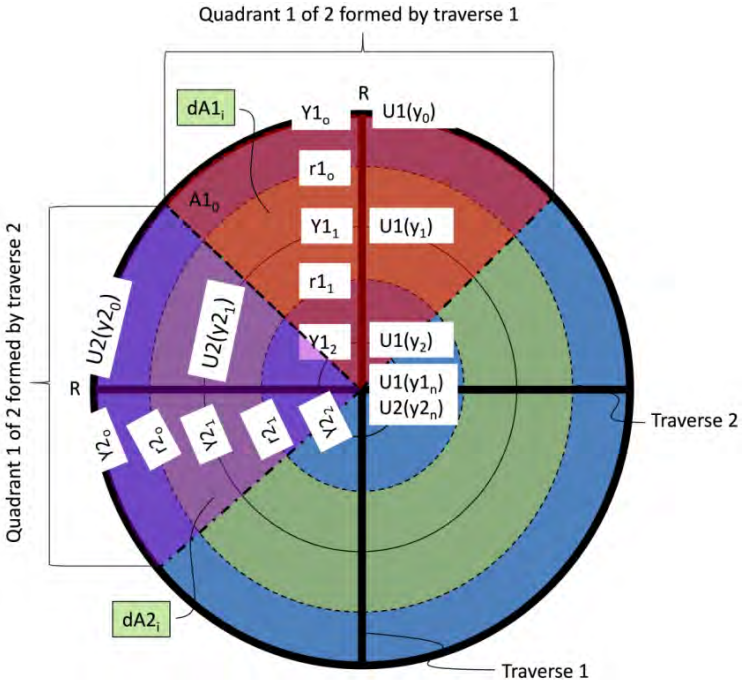

Figure 47: Two traverses with a 90° included angle

A similar approach to that of a single traverse was adopted for a double traverse. The difference in this algorithm is that it considers two matrices, Data1 and Data2, formed by Traverse 1 and Traverse 2 respectively. These matrices contain two columns, the first column representing the measurement locations and the second containing the corresponding point velocity measurement in unit length per time (m/s).

The pseudo diagram shown in Figure 45 was applied in this approach but instead of only two segments, four sectors were created. Hence, the duct cross-section is divided into four quadrants where two quadrants utilize one traverse and the remaining two quadrants utilize the second traverse. This algorithm also required a centre point as explained in this section 5.2 (a).

A similar methodology to that described in Chapter 5.2(a) was followed to determine the volumetric flow rate through each quadrant and the total volumetric flow rate through the pipe. The algorithm was developed such that the included angle between the two traverses need not be 90°. This is specifically useful for space-constrained scenarios where perpendicular traverses are not possible (see Figure 16 as an example).

5.3 Asymmetric profile with chord-wise traverses

The chord-wise approach was developed based on traverses T_a ,T_b and T_c where traverses T_a and T_c form chords, as shown in Figure 48. The three traverses create four regions where the Riemann Sum was utilized for tessellated areas or segment areas.

In order to develop the numerical algorithm for the chord-wise traversing approach, it was necessary to discretize the centre region and also the chord regions. Various simple geometries were studied to establish the most appropriate geometry to create n number of tessellated areas shown by Figure 48 (a).

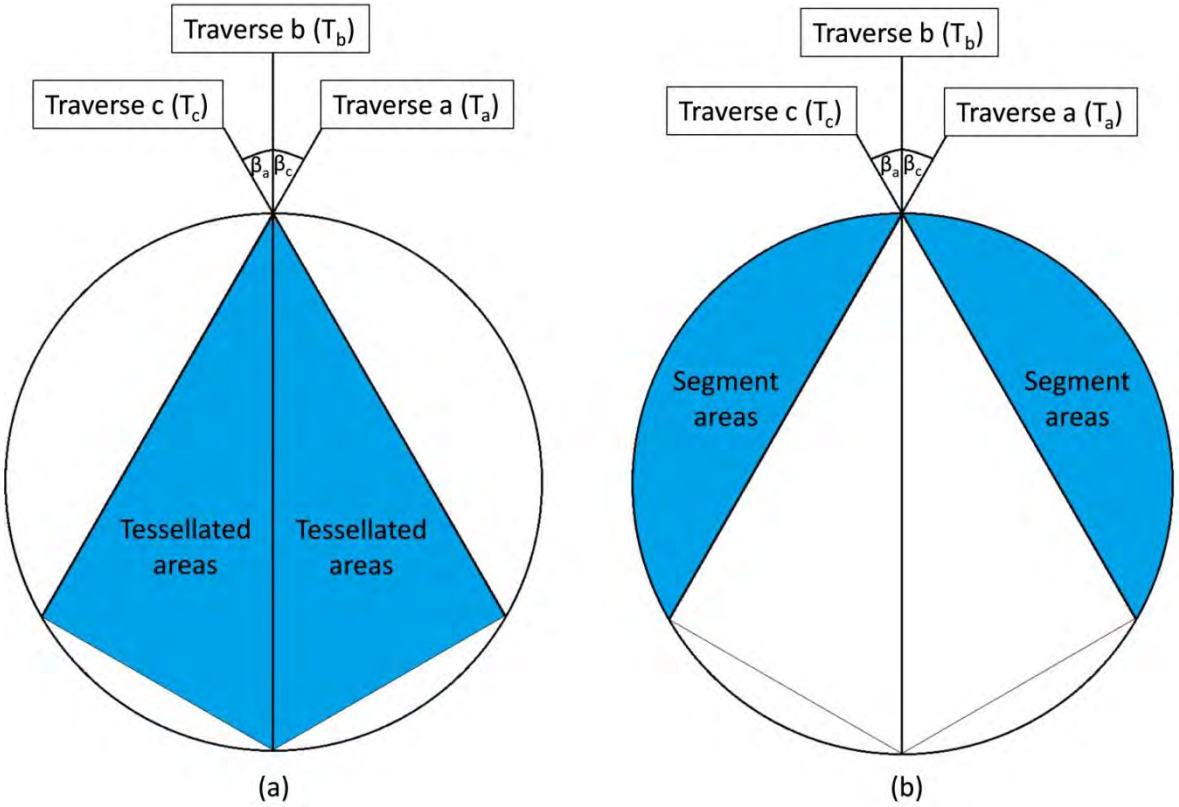

Figure 48: Chord-wise traverse (a) tessellated areas (b) segment areas

In the case of Figure 48 (b), the areas created by the chords were discretized using annulus segments.

For the tessellated areas, they can be approximated with quadrilaterals or triangles. The various types of quadrilaterals and their geometric definition are given below.

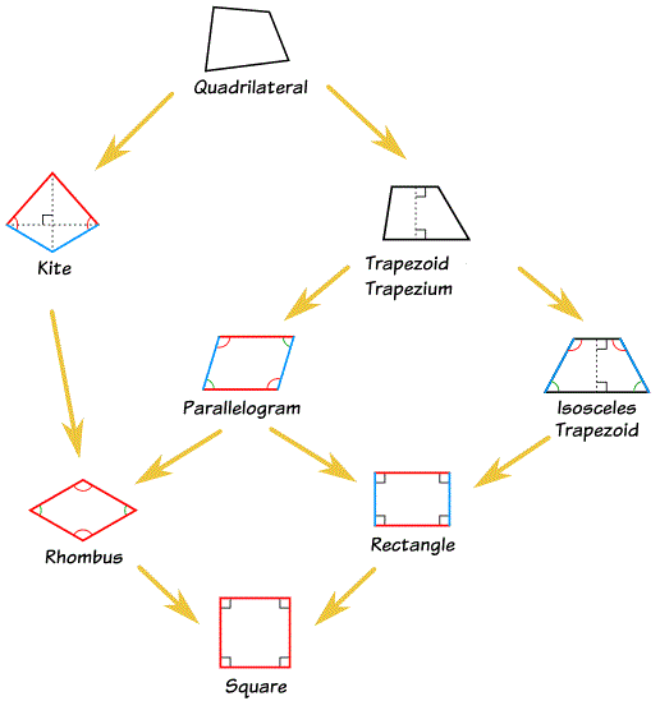

Figure 49: Types of quadrilaterals [29]

Table 2: Summary of the quadrilaterals considered

Geometry	Quadrilateral criteria enabling the use of the geometry to tessellated area
Kite	Two pairs of equal adjacent sides
Trapezium	One pair of parallel sides
Isosceles trapezium	A trapezium with two sides equal
Rhombus	Two pairs of parallel sides with all sides equal in length
Rectangle	Two pairs of parallel sides at right angles
Square	A rectangle with all sides equal in length

After finding none of the quadrilaterals listed in Table 2 suitable for creating tessellated areas of the complete region, it was decided to introduce triangles to discretize the cross-sectional area.

An immediate advantage of using a triangular geometry is that its area can be calculated anywhere in space for known vertices coordinates. This was achieved through the use of vector algebra.

To development the algorithm, a single triangle in 2D, was considered. The area of a triangle in 2D is given as [30]:

$$A = \frac{1}{2}\left\| V_1 x V_2 \right\| \tag{29}$$

where V_1 and V_2 are vectors connecting vertices 1 to 3 and 1 to 2 respectively, as shown in Figure 50.

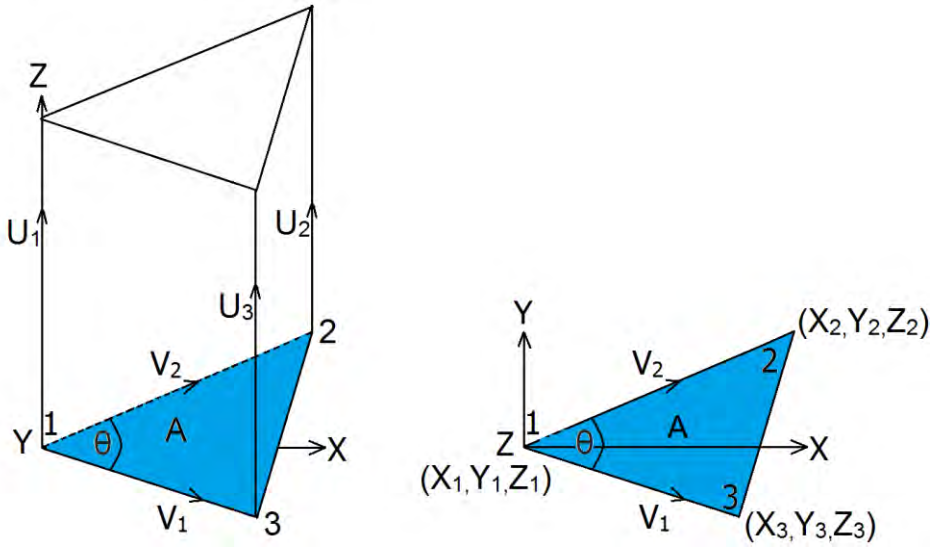

Figure 50: Single projected triangle

Substituting the variables shown in Figure 50, Equation (29) becomes

$$A = \frac{1}{2}\left\| \begin{pmatrix} x_1 & y_1 & 1 \\ x_2 & y_2 & 1 \\ x_3 & y_3 & 1 \end{pmatrix} \right\| \tag{30}$$

thus making it possible to calculate the area of a triangle in 2D.

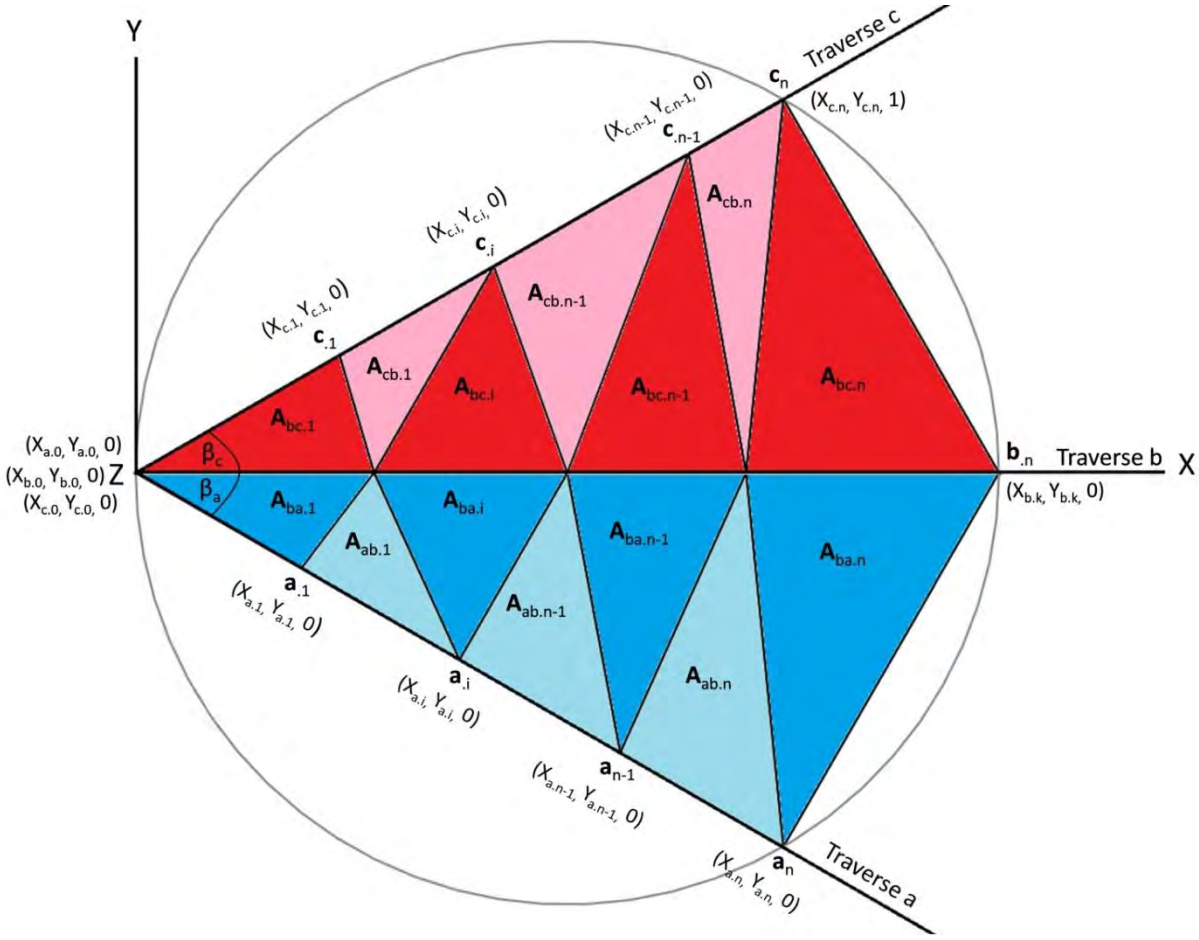

Figure 51: Treatment of the centre area with tessellated triangles

The measurement points along Traverse a, Traverse b and Traverse c are denoted by a, b and c respectively. The two chord traverses form an angle ±β with the centre traverse or Traverse b. The coordinates of the vertices along Traverse a can be obtained by

$$\begin{aligned} Xa_i &= a_i \cdot \cos(-\beta_a) \\ Ya_i &= a_i \cdot \sin(-\beta_a) \end{aligned} \tag{31}$$

Similarly, by replacing a with c and β_a with β_c, it is possible to determine the coordinates of the vertices along Traverse c. Since Traverse b was chosen to lie on the X-axis, its vertices coordinates are simply the measurements points along its traverse.

The area A_{ba} refers to the area of a triangle with two vertices along Traverse b and one vertex along Traverse a. Similarly, area A_{ab} refers to a triangle created by two vertices along Traverse a and one vertex along Traverse b. The same applies for areas A_{bc} and A_{cb}.

By substituting Equation (31) with Equation (30), the area of the discretized tessellated triangles along traverse a and b is respectively given by.

$$Aab_i = \frac{1}{2}\left\| \begin{pmatrix} Xa_i & Ya_i & 1 \\ Xa_{i+1} & Ya_{i+1} & 1 \\ Xb_i & Yb_i & 1 \end{pmatrix} \right\| \tag{32}$$

$$Aba_i = \frac{1}{2}\left\| \begin{pmatrix} Xb_{i-1} & Yb_{i-1} & 1 \\ Xb_i & Yb_i & 1 \\ Xa_i & Ya_i & 1 \end{pmatrix} \right\| \tag{33}$$

Similarly by replacing *a* with *c* and β_a with β_c the area of the discretized tessellated triangles along traverses c and b can be calculated i.e. A_{ab} and A_{bc}.

The corresponding volume of each tessellated triangle is the cross-sectional area multiplied by the average vertical height, which in this case is given by the average flow velocity. See Figure 52.

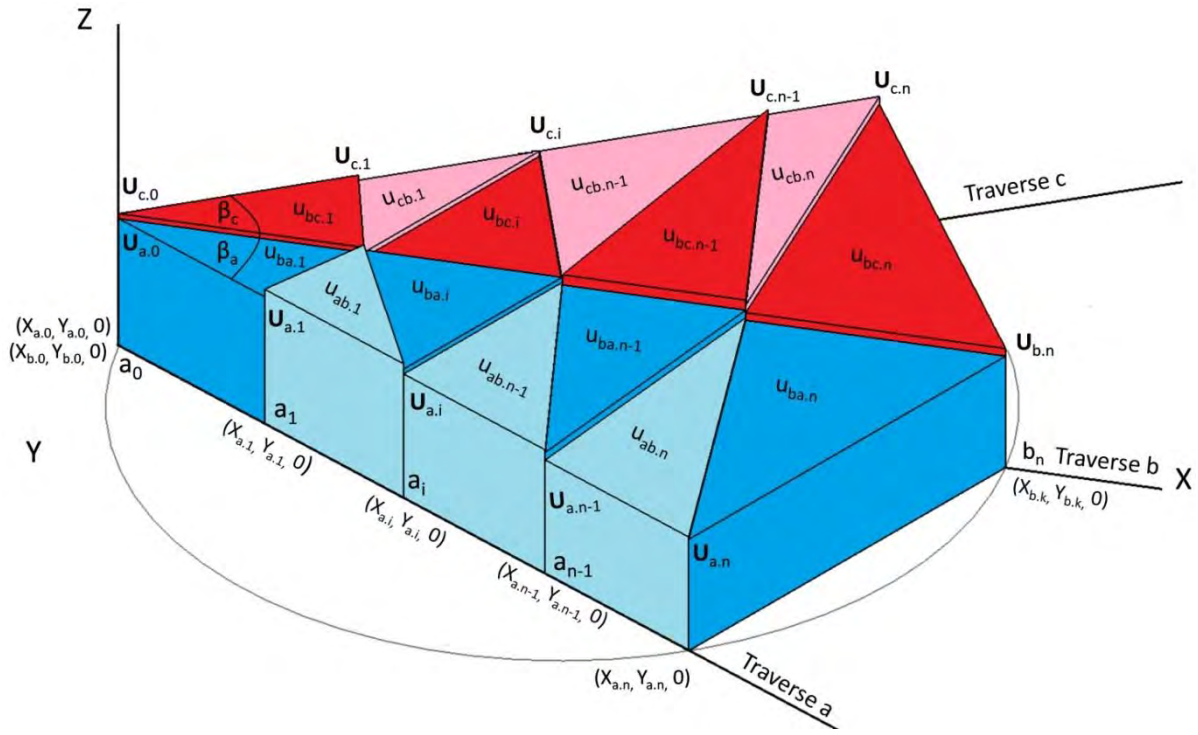

Figure 52: Treatment of the centre volume of the tessellated triangles

The average velocity of each tessellated area along Traverse a and b was calculated from

$$u_{abi} = \frac{Ua_i + Ua_{i+1} + Ub_i}{3} \tag{34}$$

$$u_{bai} = \frac{Ub_{i-1} + Ub_i + Ua_i}{3} \tag{35}$$

By replacing *a* with *c* it is possible to calculate the average velocities along traverse c and traverse b. It was found that simply applying Equations (34) and (35) introduces approximation errors because the equation considers the boundary velocity as zero. Therefore the last average velocities along traverses a and b were replaced by

$$u_{ab_{n-1}} = \frac{Ua_{n-1} + Ub_{n-1}}{2} \qquad \text{and} \tag{36}$$

$$u_{ba_n} = Ub_{n-1} \tag{37}$$

The same was done for the last average velocities along traverses c and b.

It was understood that this approach of taking the average flow velocity at the vertices might not necessarily be the best approach. This is because the flow does not necessarily have a flat upper surface as modelled by the tessellated triangles but rather has a skew-like or tilted surface. Therefore a better approach would be to calculate the centroid height of the tilted triangle and use that for calculating resultant velocity U.

The total estimated volumetric flow Q_{est} of the tessellated area was obtained by adding the volumetric flows Q_{ab} , Q_{bc} , Q_{cb} and Q_{bc} which are given by

$$Q_{ab} = \sum_{i}^{n} Aab_i \cdot u_{ab_i} \quad and \tag{38}$$

$$Q_{ba} = \sum_{i}^{n} Aba_i \cdot u_{ba_i} \quad and \tag{39}$$

$$Q_{est} = \left(Q_{ab} + Q_{ba}\right) + \left(Q_{cb} + Q_{bc}\right) \tag{40}$$

Because of the triangular tessellation scheme, it was necessary to enforce a rule that the number of measurement points along all traverses is the same. However, their spacing need not be equidistant.

The treatment of the side segments was based on the principle of an area of a segment which is defined as

$$A_{seg} = \frac{1}{2}\left(R^2\right)\left(\alpha - \sin\alpha\right) \tag{41}$$

where R is the radius of the circle and α the angle that subtends the chord at the origin.

Figure 53 shows how the segments were discretized into annular segments. In this case, only the data along traverses a and c were considered, where the discretized measurement locations along traverses a and c are represented by xa and xc respectively.

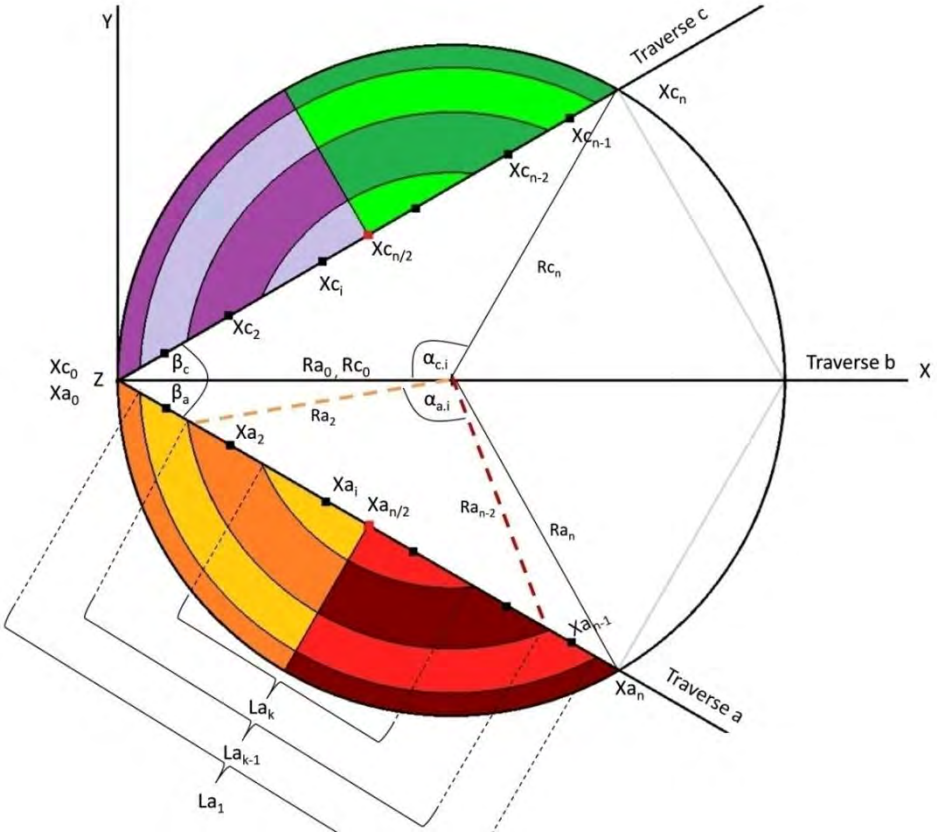

Figure 53: Treatment of the two remaining segment areas

The algorithm was developed by creating sectors of radius Ra_i and Rc_i from which the lengths La and Lc of the discretized segments is obtained by

$$La_i = \left|xa_{n-i+1} - xa_i\right|$$
$$Lc_i = \left|xc_{n-i+1} - xc_i\right| \tag{42}$$

The midpoints, xa and xc, of the discretized measurement locations along traverse a and traverse b are given by

$$xa = Xa_{i-1} - Xa_i$$
$$xc = Xc_{i-1} - Xc_i \tag{43}$$

The angles α_a and α_b that subtend the sector from which the area of the discretized segments is obtained, are calculated by

$$\alpha_{a_i} = \arccos\left[\frac{\left(Ra_i\right)^2 + \left(Ra_i\right)^2 - \left(La_i\right)^2}{2 \cdot Ra_i \cdot Ra_i}\right]$$
$$\alpha_{c_i} = \arccos\left[\frac{\left(Rc_i\right)^2 + \left(Rc_i\right)^2 - \left(Lc_i\right)^2}{2 \cdot Rc_i \cdot Rc_i}\right] \tag{44}$$

where Ra and Rc are given by

$$Ra_i = \sqrt{\left(xa_i\right)^2 + \left(\frac{D}{2}\right)^2 - 2xa_i \cdot \frac{D}{2} \cdot \cos\left(\beta_a\right)}$$
$$Rc_i = \sqrt{\left(xc_i\right)^2 + \left(\frac{D}{2}\right)^2 - 2xc_i \cdot \frac{D}{2} \cdot \cos\left(\beta_c\right)} \tag{45}$$

By inserting Equations (44) and (45) into Equation (41), the area of the each segment becomes

$$A_{seg\_a_i} = \frac{1}{2}\left(Ra_i^2\right)\left(\alpha_{a_i} - \sin\alpha_{a_i}\right)$$
$$A_{seg\_c_i} = \frac{1}{2}\left(Rc_i^2\right)\left(\alpha_{c_i} - \sin\alpha_{c_i}\right) \tag{46}$$

Therefore the area of the annular segments up to the midpoint of traverse a and traverse c, is given by

$$A_{seg_a\_annulus} = \frac{1}{2}\left(A_{seg\_a_i} - A_{seg\_a_{i+1}}\right)$$
$$A_{seg_c\_annulus} = \frac{1}{2}\left(A_{seg\_c_i} - A_{seg\_c_{i+1}}\right) \tag{47}$$

As in calculating the volume of the tessellated areas, the volume of each discretized annular segment was determined by multiplying its area with the corresponding height. In this case though, the height (velocities) were taken as the point velocities along traverse a and traverse c as illustrated by Figure 54.

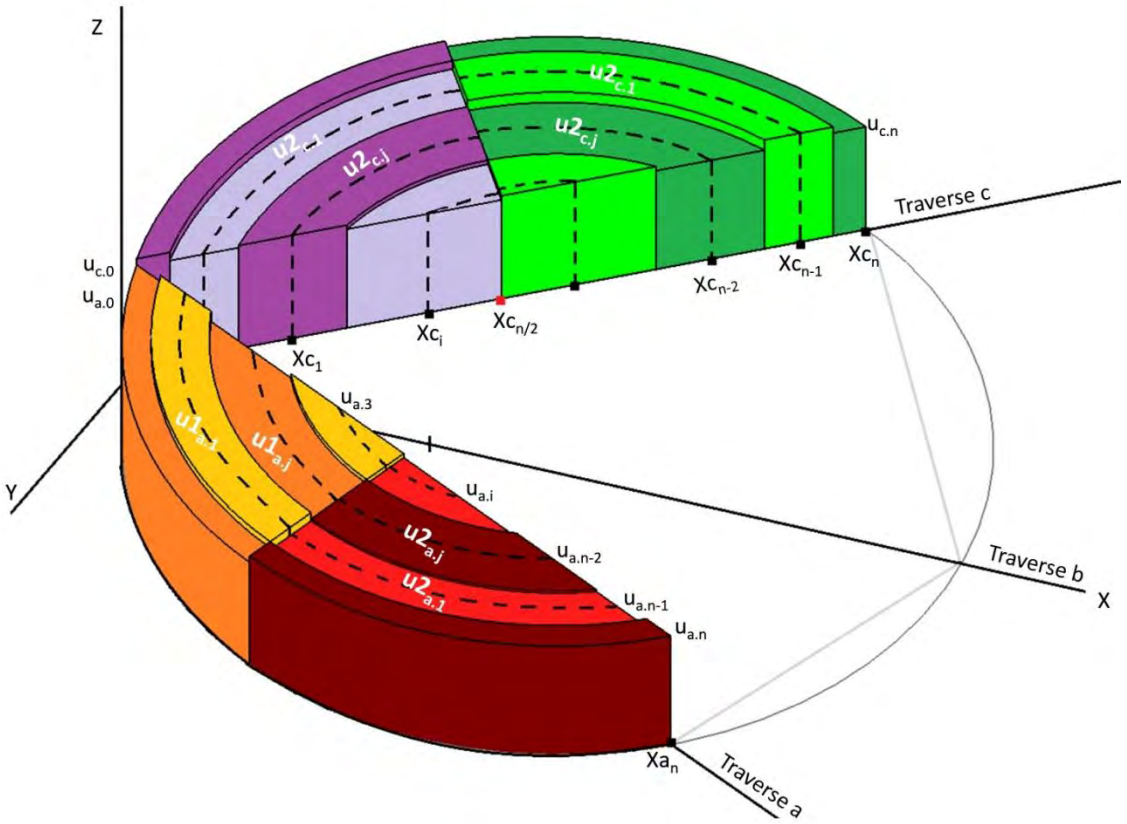

Figure 54: Treatment of the two remaining segment volumes

The sum of the volumetric flow rate along Traverse a and Traverse c is then given by

$$Q_a = 2 \cdot \sum A_{seg_a\_annulus_i} \cdot U_{a_i}$$

and (48)

$$Q_c = 2 \cdot \sum A_{seg_c\_annulus_i} \cdot U_{c_i}$$

To this point, all the areas of the cross-section of the pipe have been accounted for except the two thin bottom segments. These areas were assumed to be negligible compared to the overall area of the pipe due to the zero slip conditions on the wall. This means that the velocity close to the pipe wall is close to zero. However, it was understood that neglecting these areas might introduce approximation errors.

6. Algorithm Validation and Testing

6.1 Reference data

Experimental tests are not necessarily the best way of determining exact flow, and neither is plant data. The use of the power law for symmetric flow and analytical integration thereof was therefore used to arrive at exact mass flow (Equation (27)). A visual representation of the process of verifying and validating the algorithms is shown in Figure 55 , Figure 57 and Figure 58. In addition, the representation aim to ensure that the algorithms are mathematically sound. Hence the convergence of the *%Error* shown in Figure 56 and Figure 57 were monitored and shown in Figure 59.

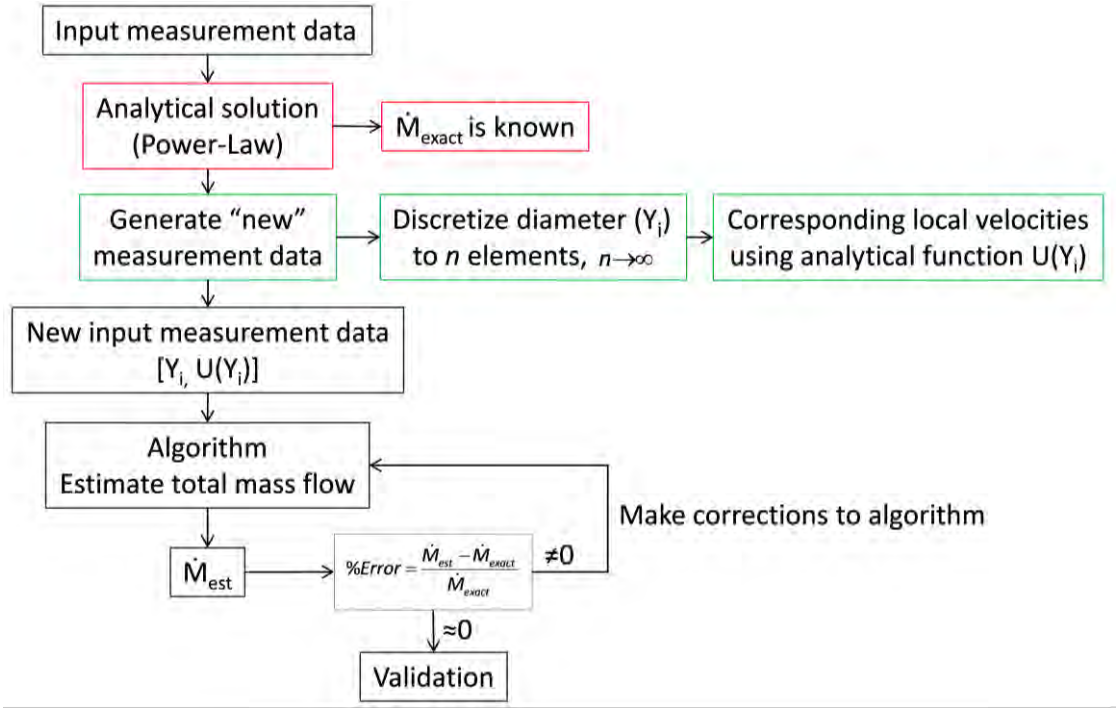

Figure 55: Sequence of verifying the mathematical model using an analytical solution

Using the above process, both the single and double traverse algorithms were verified to be 100% correct when the number of measurement points approaches infinity.

The chord-wise algorithm was tested using a 3D tessellated CAD model with a known exact volume. Figure 56 shows how the author verified the chord-wise technique by comparing the estimated volume of a 3D model to the exact volume obtained from the CAD model. In essence, the 3D model is a representation of the volumetric flow rate through a pipe.

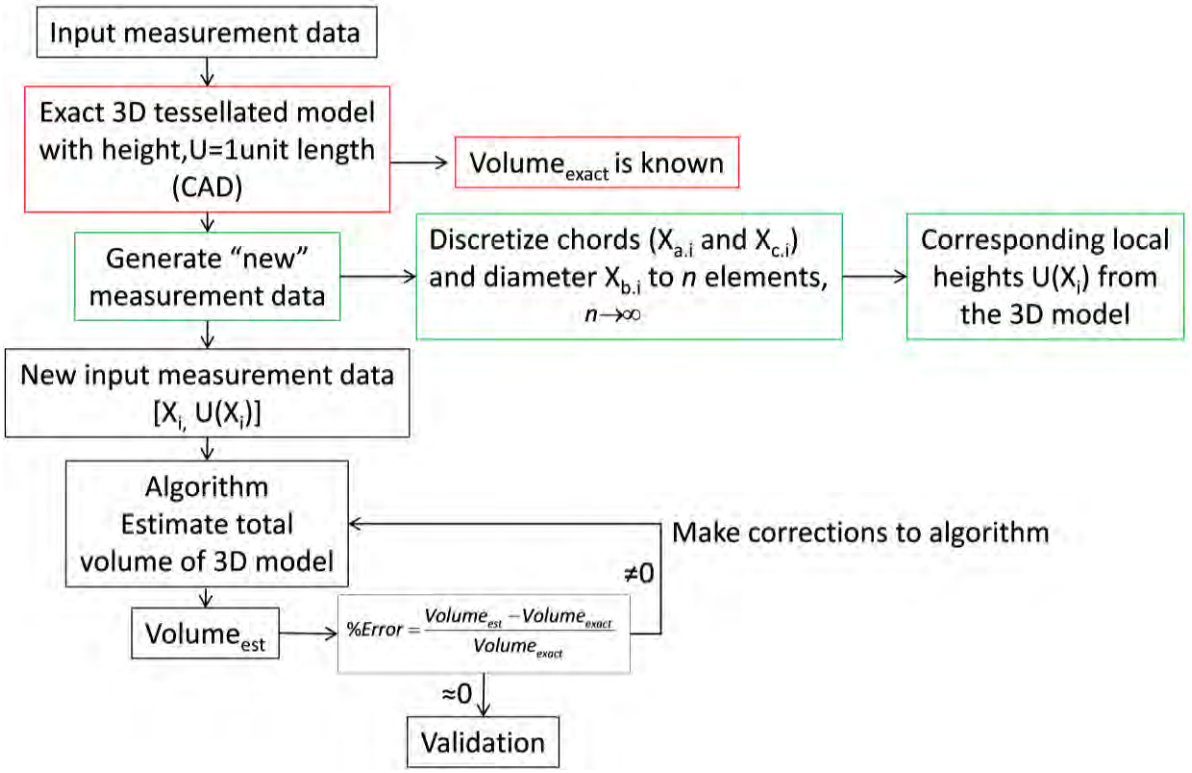

Figure 56: Sequence of verifying the mathematical model using a 3D tessellated CAD model

The chord-wise traverse algorithm was verified to be 100% correct when the number of measurement points approaches infinity. This is shown by Figure 59.

After verification of the algorithm using the analytical solution, the algorithm was adapted to conduct CFD test cases indicated in Figure 60. CFD was used to create an asymmetric flow profile, but still having an exact known flow.

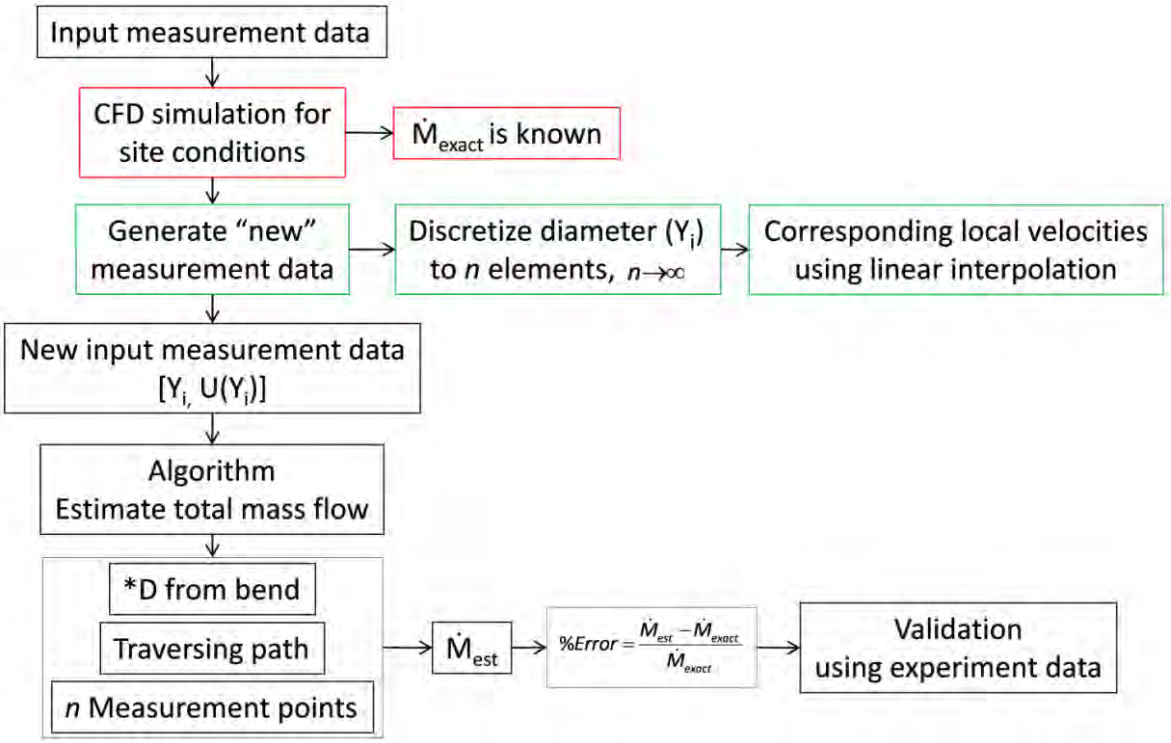

Figure 57: Sequence of verifying and applying the mathematical model using a CFD model

An experiment was conducted to corroborate the algorithm. This is later discussed in Chapter 8. The approach to this exercise is indicated in Figure 58.

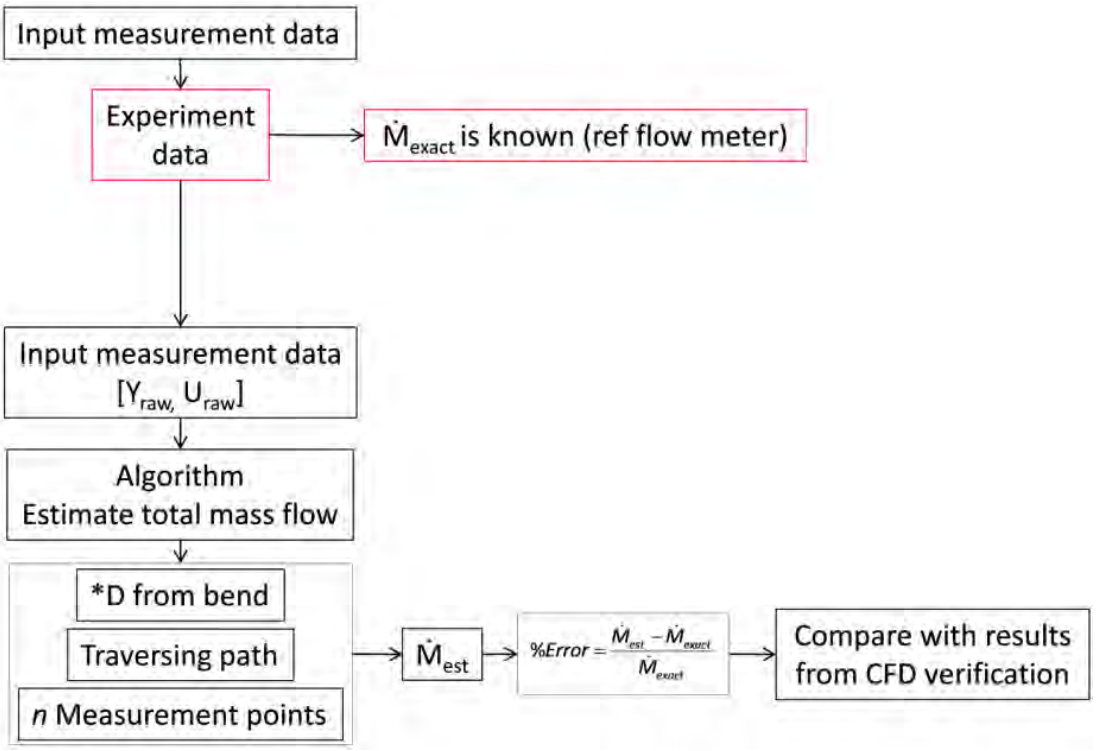

Figure 58: Sequence of validating the mathematical model

6.2 Validation of algorithm against symmetric flow

Figure 59 shows the results of the algorithm verification using an analytical solution as well as CFD model for a single traverse and two traverses. The chord-wise approach was verified using a 3D CAD model representing the symmetric profile.

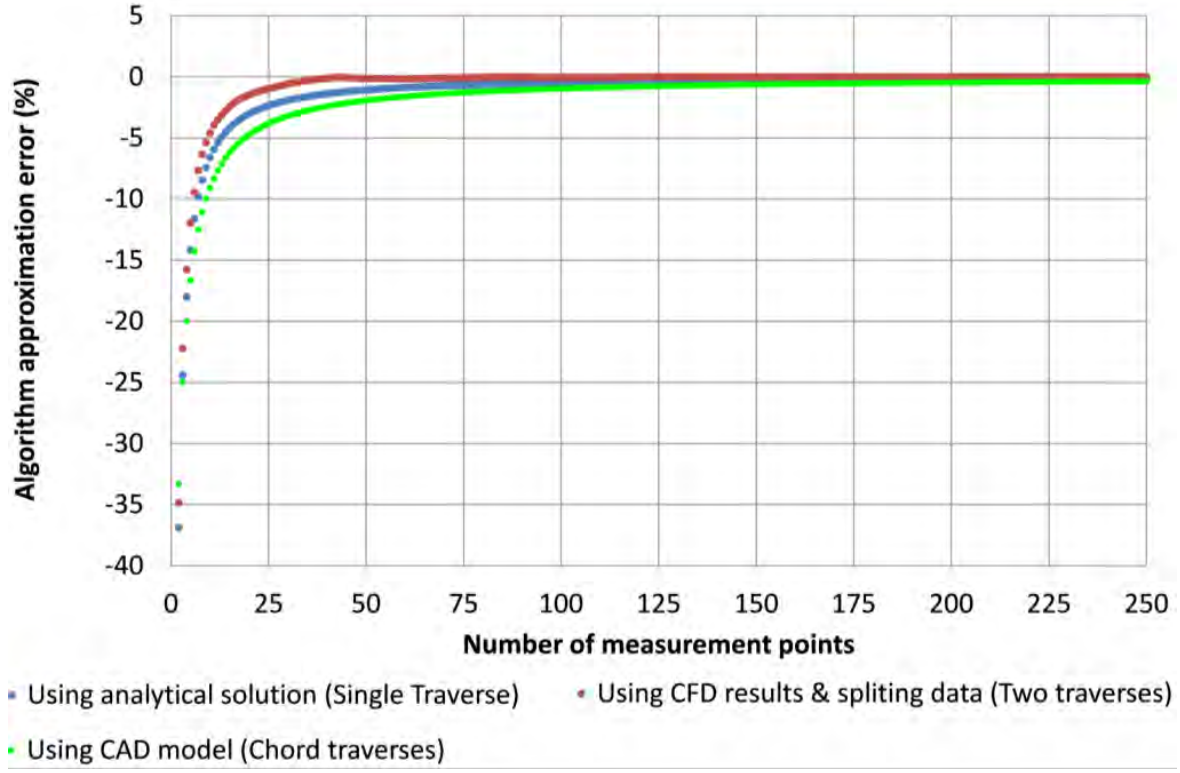

Figure 59: Algorithm test results on a symmetric flow profile

The results show that all three algorithms contain no possible mathematical errors because the algorithm approximation error tends to zero with infinite number of measurement points.

During the development of the three algorithms, linear interpolation was used to discretize the pipe cross-sectional length along which the traverse was made. However, the algorithms can be improved by using spline interpolation rather than linear interpolation. In this way, the errors introduced by sharp corners can be avoided.

6.3 Testing algorithms on asymmetric flow

In order to perform CFD simulations and apply the developed algorithms, it was important first to identify the Reynolds number range for the simulations. The range of Reynolds numbers was obtained by considering the typical pipes that exist on site and a typical average flow velocity of 2m/s [31]. A summary of the simulation test cases that were considered is shown in Figure 60.

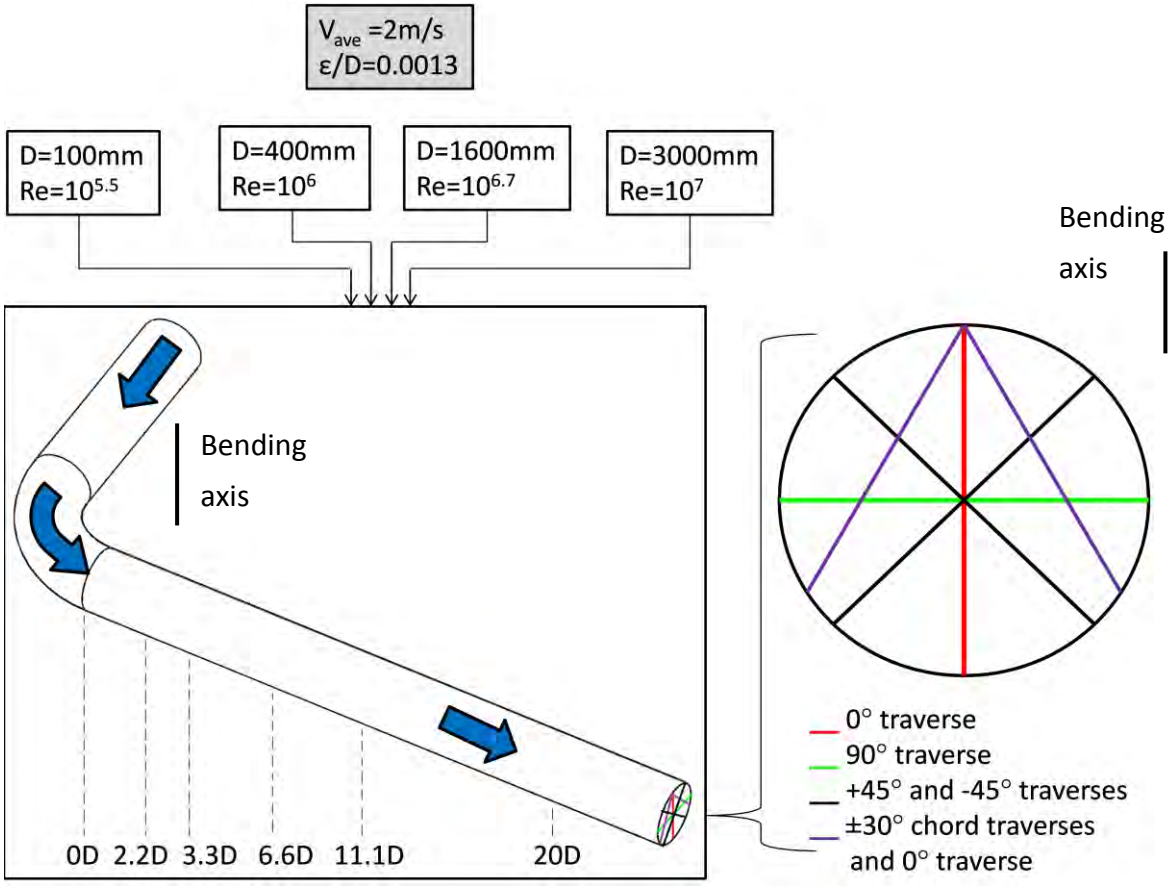

Figure 60: CFD Simulation test cases

It is further shown in Figure 60 that more simulation test cases were conducted at a distance closer to the 90°. This was to test the usefulness of the algorithms for conditions where the flow profile was expected to be asymmetrical.

It is important to note that only the axial velocity component was considered during the CFD simulation. The reason for this was that the algorithms were developed for an inline point velocity measuring technique.

6.4 Results from test cases

The following are results obtained from the test cases showing the expected measurement uncertainty for a given number of measurement points.

Only the results obtained for the $Re=10^7$ are shown in Figure 61, Figure 62 and Figure 63 because the Reynolds number is the typical Reynolds number in the CW ducts as calculated by Equation (24). The results for other Reynolds numbers can be found in the Appendix.

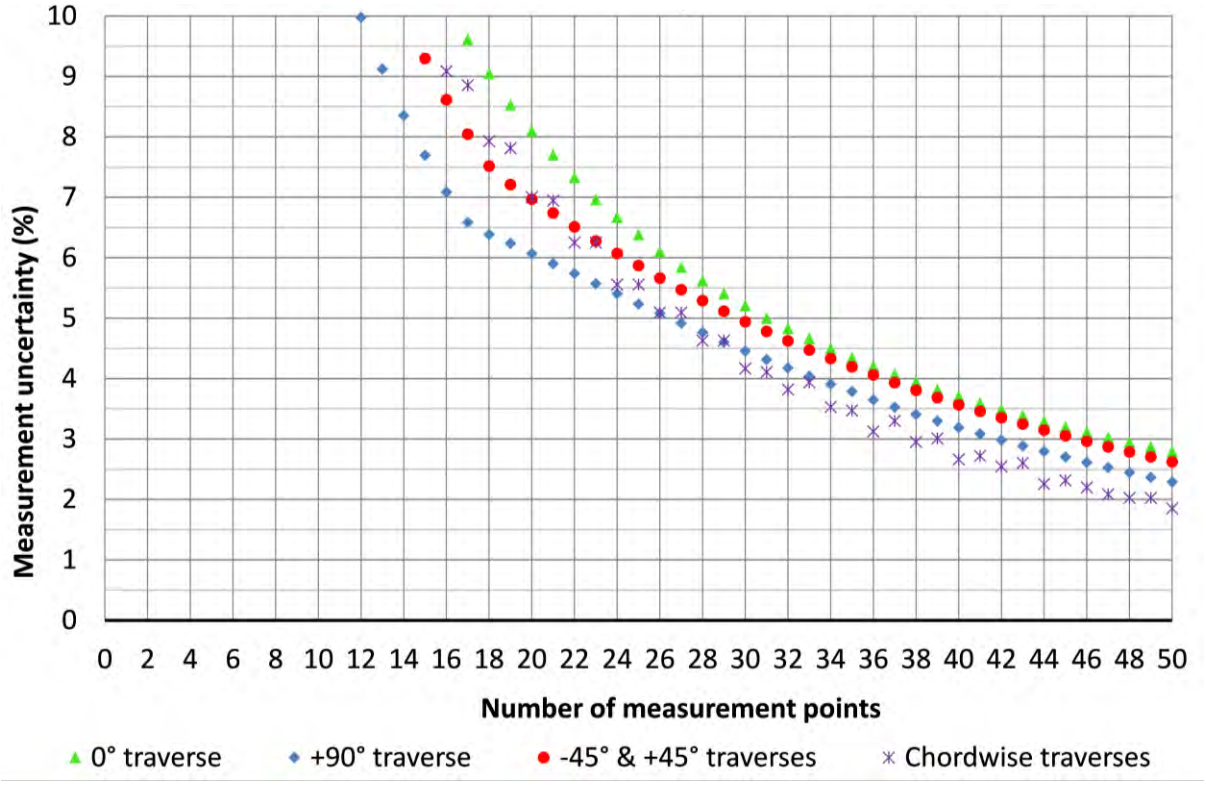

Figure 61: Measurement uncertainty for a given number of measurement points for traversing paths at 0D downstream of bend, $Re=10^7$ and $\varepsilon/D=1.3x10^{-3}$

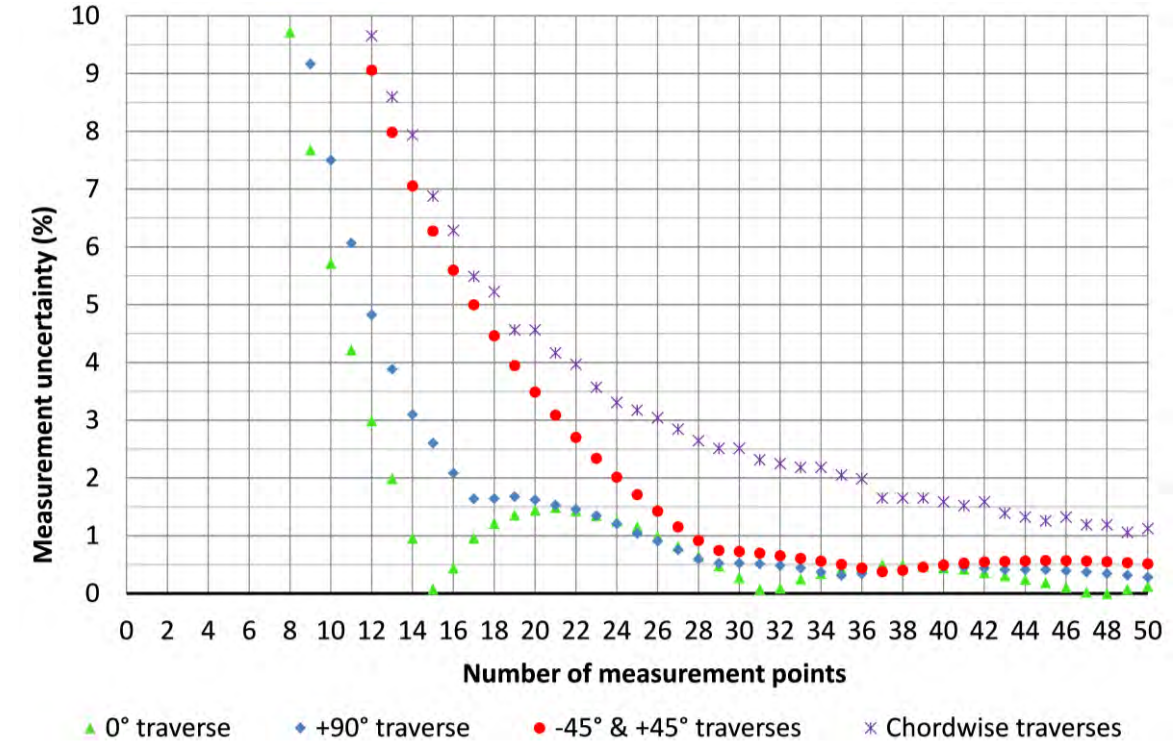

Figure 62: Measurement uncertainty for a given number of measurement points for traversing paths at 2.2D downstream of bend, Re=10^7 and $\varepsilon/D=1.3x10^{-3}$

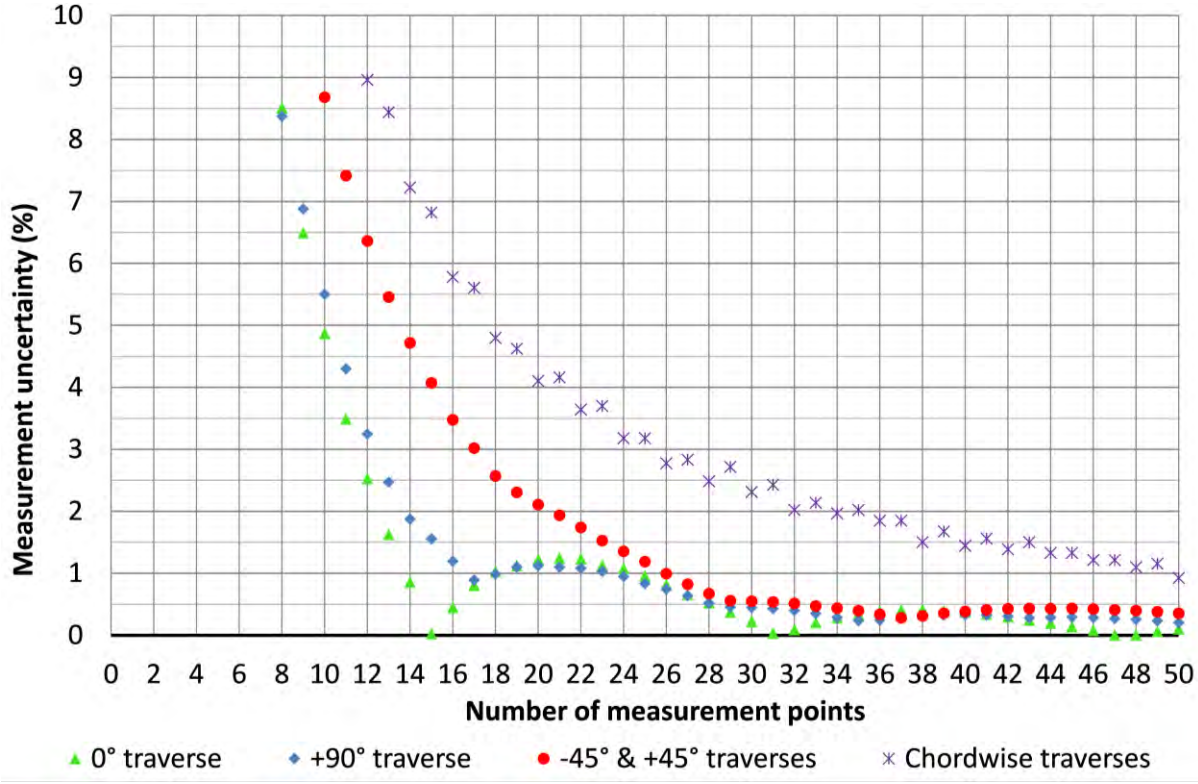

Figure 63: Measurement uncertainty for a given number of measurement points for traversing paths at 20D downstream of bend, Re=10^7 and $\varepsilon/D=1.3x10^{-3}$

7. Applicability of Algorithms

The results obtained from the CFD simulation test cases indicate that the algorithm approximation error, in all test cases, tends to decrease somewhat hyperbolically with an increase in the number of measurement points. The rate of convergence, though, differs from one traversing path to the other as already shown in Figure 59. In addition, the distance downstream of the 90° bend also contributes to the convergence of the numerical solution. For this reason, the CFD simulation results were studied to determine the applicability of the algorithms for single, multiple and chord-wise traverses.

7.1 Single traverse

When flow rate measurements are conducted at a known distance downstream of a 90° bend, it is possible to recommend the type of single traverse suitable for measurement. In this case, it is important to establish the plane of bending since a 0° traverse may produce different approximation results from a 90° traverse. The most accurate conditions are presented in Table 3.

Table 3: Single traverse recommendation

Log(Re)	0D	2.2D	3.3D	6.6D	11.1D	20D
5.5	90°	0°	0°	0°	0°	0°
6	90°	0°	0°	0°	0°	0°
6.7	90°	0°	0°	0°	0°	0°
7	90°	0°	0°	0°	0°	0°

The CFD simulation results indicate that for flow rate measurements at 0D downstream of a 90° bend, it is better to utilize the 90° traverse as it offers a better approximation compared to a 0° traverse. This can be attributed to the fact that, closer to a bend, a 90° traverse is more likely to intersect a region across the pipe where the maximum velocity (V_{max}) is measured. This reasoning is further discussed in section 8.3.2 and shown in Figure 85.

Table 3 also shows that it is better to utilize the 0° traverse with an increase in distance downstream of a 90° bend. This can be attributed to the fact that the flow profile tends to be fully developed and symmetric about the vertical axis. This is indicated in Figure 64.

7.2 Multiple traverse

Following the single traverse at 0° or 90°, a study was also conducted where two single traverses were simultaneously utilized to measure the flow rate. The purpose was to determine which orientation of these multiple traverses should be recommended. It was found that using two traverses at 0° and 90° to the vertical offers no additional advantage over the average of the accuracy obtained using the 0° and 90° traverse. Either the 0° or 90° traverse is thus recommended.

However, utilizing the two single traverses at an angle of ±45° to the vertical offers the smallest static error and number of inconsistencies compared to all other traverses. These errors are as a result of any reason or assumption made in the algorithms. The errors remain constant from some number of discretized elements to infinity. Refer to Figure 67. The least static error mentioned, may be attributed to the fact that the two traverses have a higher probability of intersecting points of maximum velocity for all flow conditions and distance downstream of the bend. See Figure 83.

7.3 Chord-wise traverse

It was found that the chord-wise traverse does not have an advantage over any of the traverses studied for given flow conditions and flow rate measurements downstream of the 90° bend. Furthermore, the chord-wise traverse technique produces consistent static error, and the errors are the largest among all traverses. This was already discovered in section 6.2.

7.4 Distance from bend

Based on the investigations, it was noted that the 90° traverse offered better results closer to the bend. In other words, for a given flow condition and number of measurement points, the 90° traverse renders the least approximation errors. On the other hand, for flow rate measurements taken further away from the bend, a multiple traverse of two traverses at ±45° to the vertical plane should be used.

7.5 Static error compensation

In Chapter 5, it was noted that certain assumptions and mathematical and geometrical techniques utilized in developing the algorithms might introduce approximation errors. These errors result in no improvement to the numerical solution with infinite discretized elements. This is referred to as the static error, which can be compensated for if known.

Reynolds number is likely to be the major parameter which affects the static error, apart from distance from the bend. An investigation was done to determine whether the velocity profiles changed for the chosen Reynolds number. It was found that the chosen Reynolds number range did not produce significantly different velocity profiles for a given distance from the bend. The flow profile comparisons at various Reynolds numbers for a 0° traverse are shown in Figure 64 and for 90° in Figure 65.

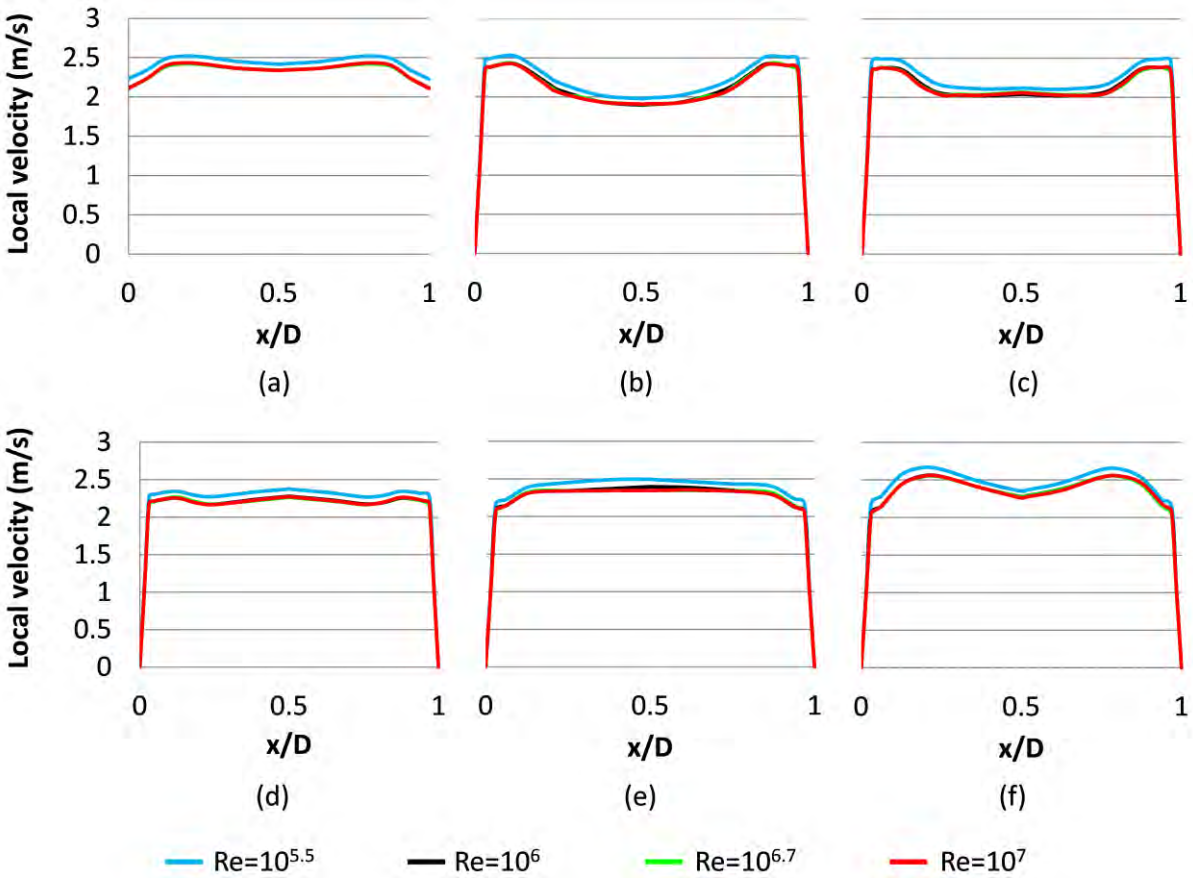

Figure 64: Flow profile comparison at various Reynolds numbers for 0° traverse at (a) 0D (b) 2.2D (c) 3.3D (d) 6.6D (e) 11.1D (f) 20D

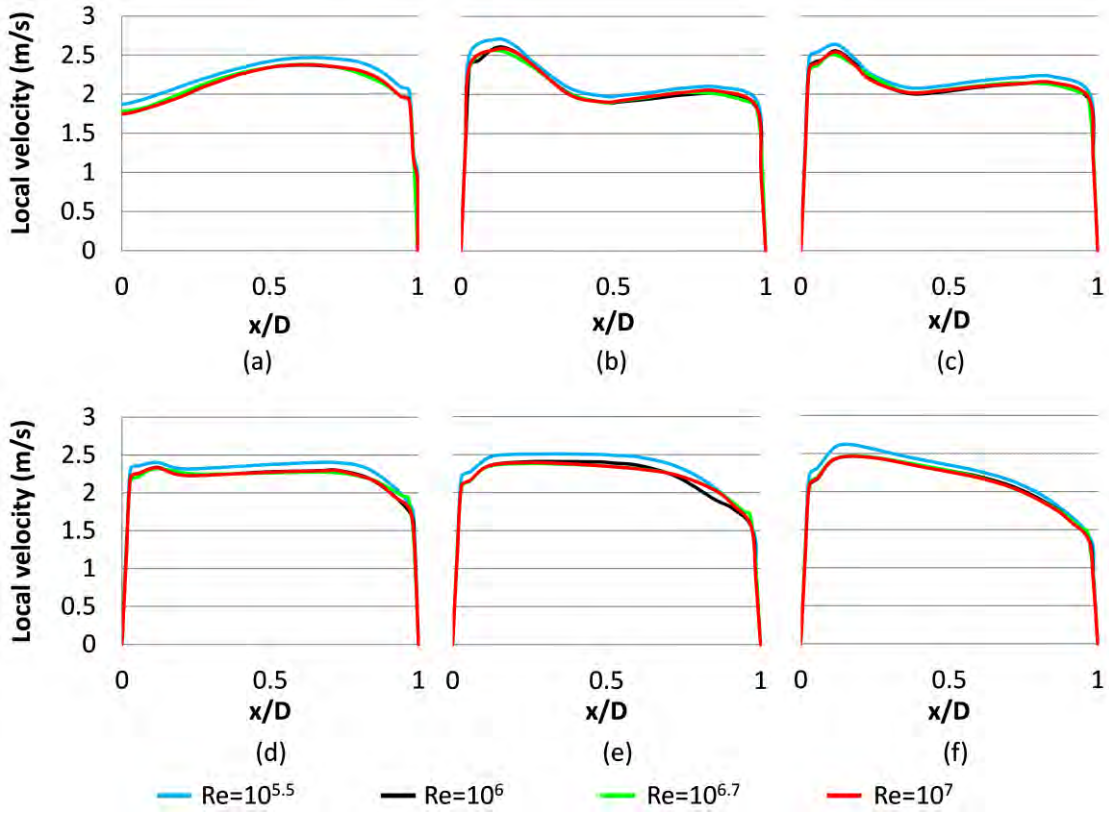

Figure 65: Flow profile comparison at various Reynolds numbers for 90° traverse at (a)0D (b) 2.2D (c) 3.3D (d) 6.6D (e) 11.1D (f) 20D

It was therefore expected that the static errors at the different Reynolds numbers might not be significantly different.

Furthermore, an investigation conducted to determine the effect of the relative roughness of the pipe ε/D, showed that the assumed internal surface roughness did not significantly change the flow profile. The study was performed at arbitrary distances 0D and 6.6D downstream of the bend with a Reynolds number of 10^7, which is typical of the CW flow. This was done because information on the internal surface roughness of the CW duct was not well documented. The relative roughness range of the internal surfaces of the pipe was based on the typical internal surface roughness in industry [20] .

A significant change in the velocity profile as a result of incorrect assumptions about relative roughness might introduce incorrect approximation. However, Figure 66(a) and (b) show that for the chosen relative roughness range, flow profiles do not change significantly. Selecting a relative roughness within the studied relative roughness range was appropriate.

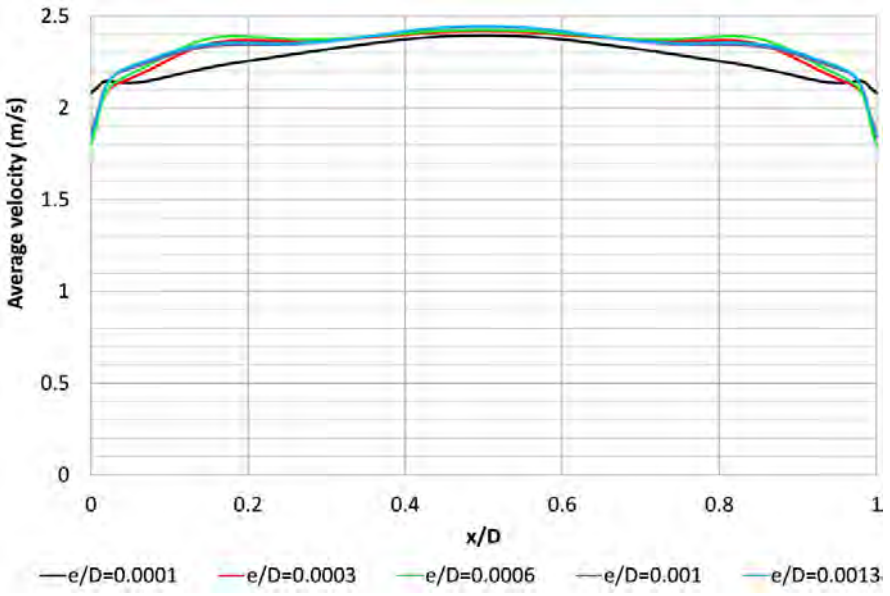

(a)

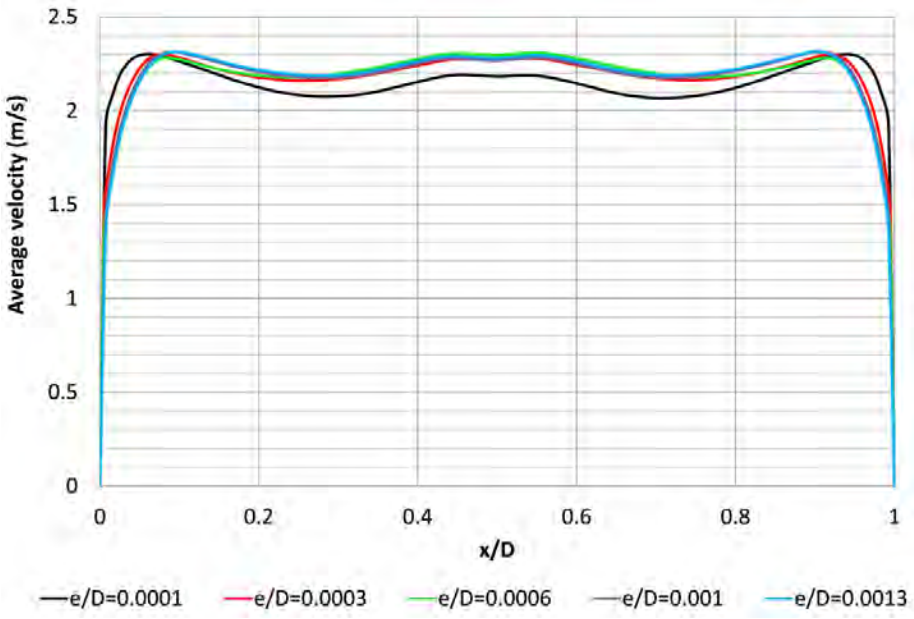

(b)

Figure 66: Comparison of different flow profiles downstream of a 90° bend for different relative roughness (0° traverse, Re=10^7) (a) at 0D (b) at 6.6D downstream.

The following were therefore found to be possible contributors to the introduced errors:

- The traverses do not entirely capture the dynamics of the flow;
- Flow re-circulations occur closer to the bend;
- There is an inherent interpolation error; and
- Algorithm approximation results from assumptions made (chord-wise technique).

Figure 67 shows the static error for a given measurement location. The experimental result could therefore be compensated using this known static error to achieve a more accurate result. The compensated flow rate can be calculated by applying the compensation percentage , comp%, to the measured flow rate as shown by Equation (49)

$$M_{correct} = \frac{M_{measured}}{(1+comp\%)} \tag{49}$$

For example: If 10 measurements are taken with a 0° traverse, the error compensation is -5%. If the calculated mass flow is 100kg/s, the compensated mass flow is 105.26kg/s.

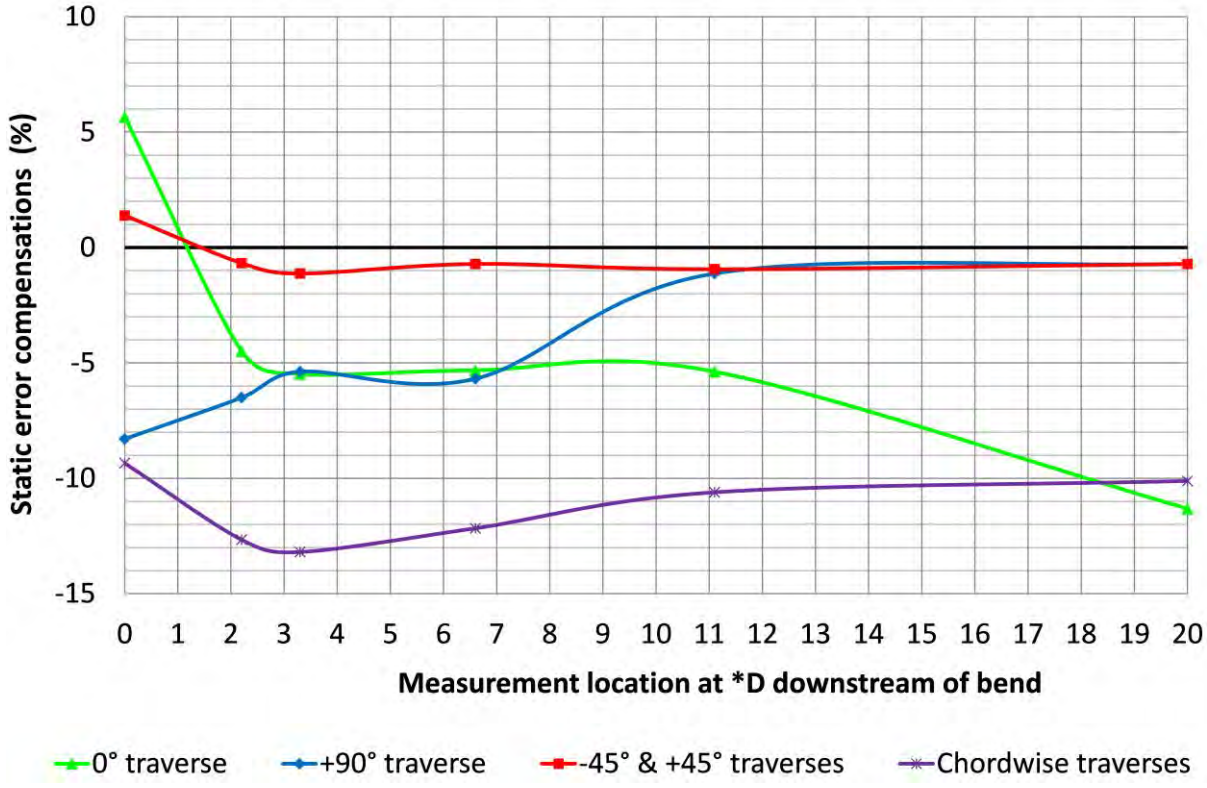

*Figure 67: Static error vs. Measurement location at *D downstream of a 90° bend, Re=10^7 and $\varepsilon/D=1.3x10^{-3}$*

It was found that at least 32 measurement points, equally spaced, would produce a measurement accuracy equal or less than 1% for all but the chord-wise traverse. This however is not valid for measurements at 0D and 2.2D after a 90° bend.

8. Physical Test

8.1 Purpose of testing

A technique of traversing probes was identified and a numerical model was developed for identifying expected flow measurement accuracy. The methodology developed investigated the dependency of flow measurement accuracy on the number of traverses across the CW duct, traverse paths, the number of measurement points along the traverse and the measurement position downstream of a 90° bend.

From the results, a set of static error compensation curves was developed, and it is suggested that one might be able to produce more accurate results using this method of compensation.

To test this idea, a physical test is needed. The physical test not only introduces numerical integration errors, but also measurement errors and flow uncertainties.

The physical tests were performed at the Eskom Water Flow Calibration Laboratory in Rosherville, which is accredited according to SANS 17025.

Due to the size of actual CW ducts (typically three metres) and high mass flow rates (typically 14 000kg/s), dimensional similarity could not be attained for the experimental work. However, the experiment was conducted in such a way that a similar flow regime was achieved, i.e. turbulent flow. This would ensure that similar flow profile trends were attained. In addition, the measurement points were equally spaced in order to satisfy the algorithms.

8.2 Test setup

In preparation for the test setup, the parameters that strongly affect or influence measurement principles were carefully controlled.

The multiple measurement positions along the length of the pipe were achieved by manufacturing a pipe spool piece with access points for all three considered traversing paths.

The internal diameter of the pipe was accurately measured using a micrometer, as shown in Figure 68, and found to be 395mm.

(a) *(b)*

Figure 68: Pipe diameter measurement (a) micrometer (b) application of micrometer

The outer diameter was calculated from the the circumference measurement using a calibrated tape measure. Calibration was undertaken at a SANAS accredited laboratory, with a calibration uncertainty of typically ± 1mm.

The water flow through the apparatus was controlled by a delivery valve and confirmed by an orifice and electromagnetic flow meter. A yaw-probe type pitot tube, coupled to a differential pressure transducer, was used to measure local flow velocities. The probe location was recorded using a linear transducer connected to the outside of the pipe.

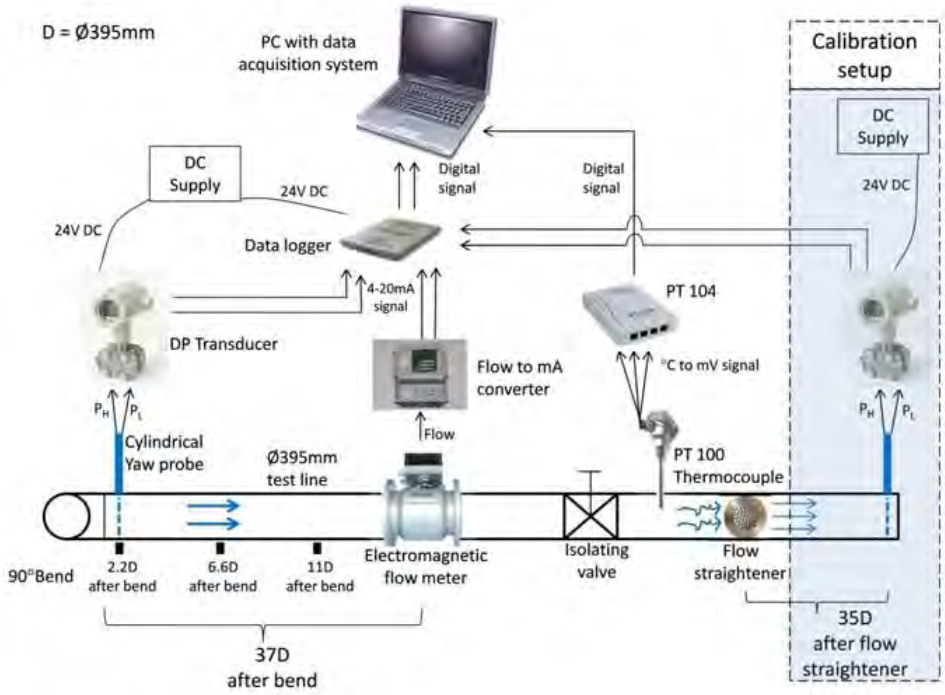

Figure 69: Physical test calibration setup diagram

Noteworthy is that the inlet flow was assumed to enter the 90° bend as fully-developed flow since there was more than 20D downstream of any flow disturbance before the bend.

The actual test setup is shown in Figure 70 (a) where one can see the test jig with a traversing bracket, pressure transducer, displacement measuring system and its display. Figure 70 (b) shows the orientation of test jig relative to the 90° bend.

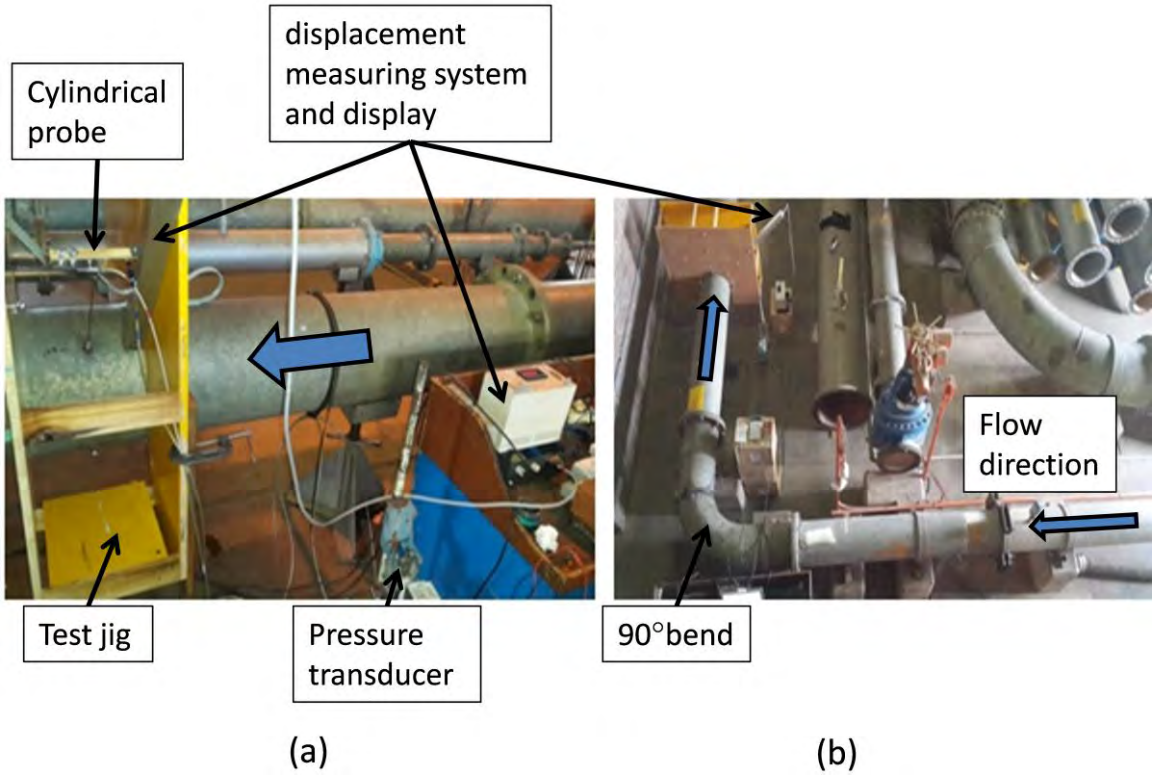

Figure 70: Actual experiment setup (a) calibration (b) physical test

The specially manufactures test spool piece was installed at different axial positions and connected to the bend and other pipe sections using flanges. These flanges ensured that the walls of two coupled pipes were aligned.

The following sign convection, shown in Figure 71, was employed when conducting the tests. This ensured consistency in the observations made and results reported.

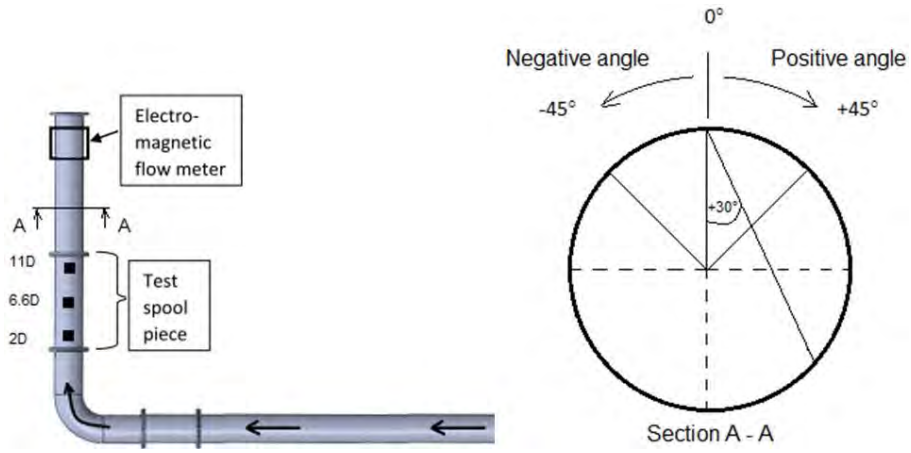

Figure 71: Physical test and sign convention

Prior to any flow measurements, the system was purged of air through the air release valves. Thereafter, flow rate measurements were conducted when the system was operating under steady state conditions.

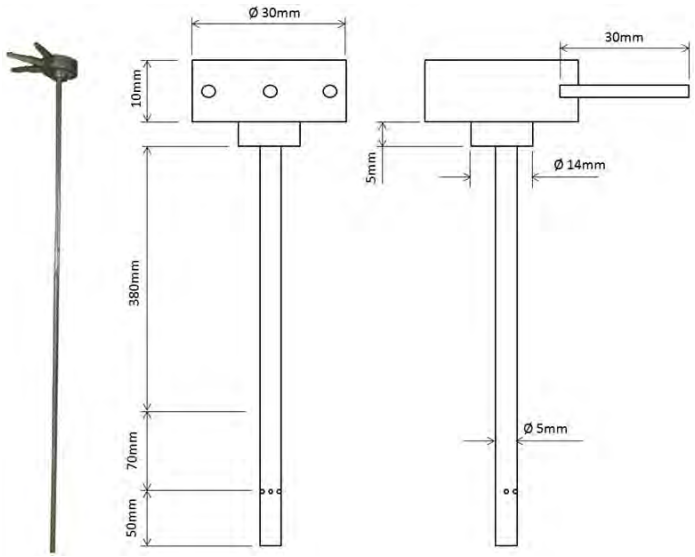

Figure 72: Cylindrical yaw probe

Figure 72 indicates the cylindrical yaw probe that was available for the experiment. The probe has three pressure ports which, when connected to two separate transducers can indicate flow direction. For this test, the two side ports were connected together.

These ports recorded not only the static pressure, but also a dynamic component V* as shown by Figure 73 and Equation (50).

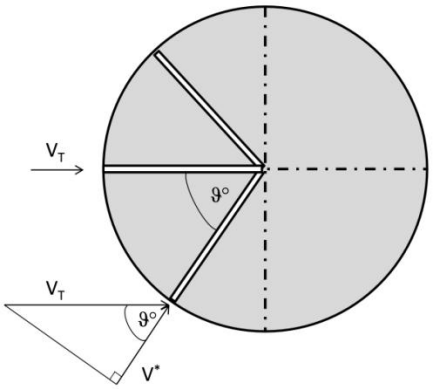

Figure 73: Static pressure correction

The reference flow velocity was calculated using the relationships below:

$$\Delta P = \frac{1}{2}\rho\left(V_T^{\,2} - V^{*2}\right)$$
$$V^* = V_T \cos(\vartheta) \qquad (50)$$
$$V_T = \sqrt{\frac{2\Delta P}{\rho}} \cdot \sqrt{\frac{1}{\left(1-\cos^2\vartheta\right)}}$$

To further ensure consistency and credibility of the experimental results, a test jig was designed and assembled as indicated in Figure 74. This jig ensured accurate probe insertion angle, as well as a platform to clamp the probe at various depths.

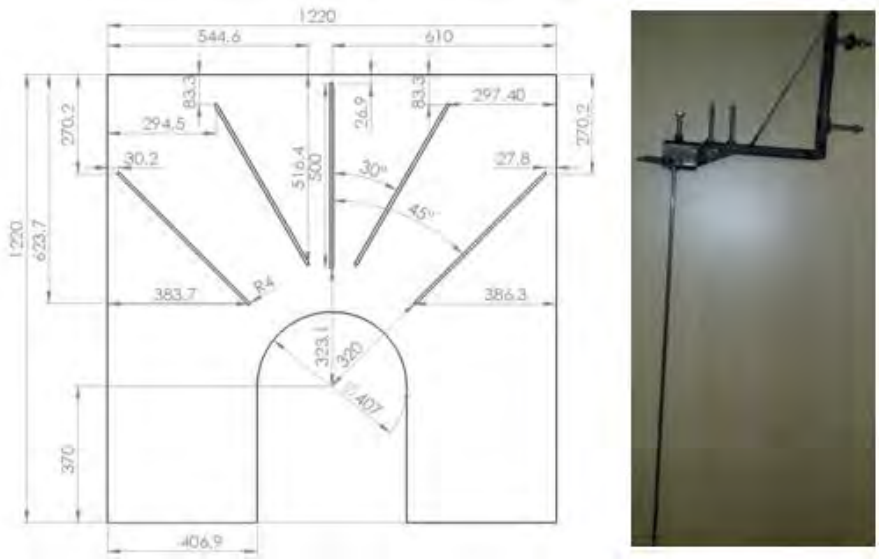

Figure 74: Probe jig panel design and probe traversing bracket

To provide for two traverses in a chord-wise manner and another traverse through the centre of the pipe (see Figure 76), a probe traversing fitting was designed and manufactured from grey PCV. Figure 76 also indicates the functionality of the probe traversing fitting through which the probe was fed for the chord-wise approach.

Figure 75: Probe traversing fitting.

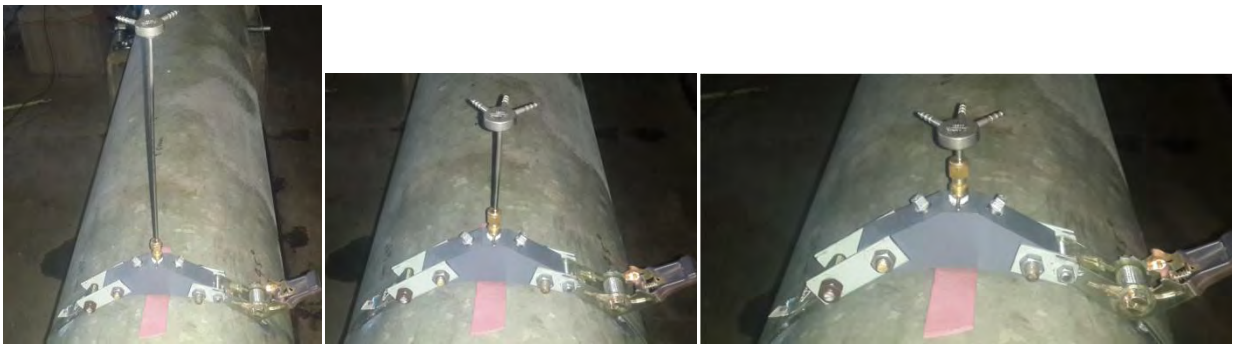

Figure 76: Functionality of the traversing fitting

The instruments shown in Figure 77 were used to perform and successfully complete the physical test.

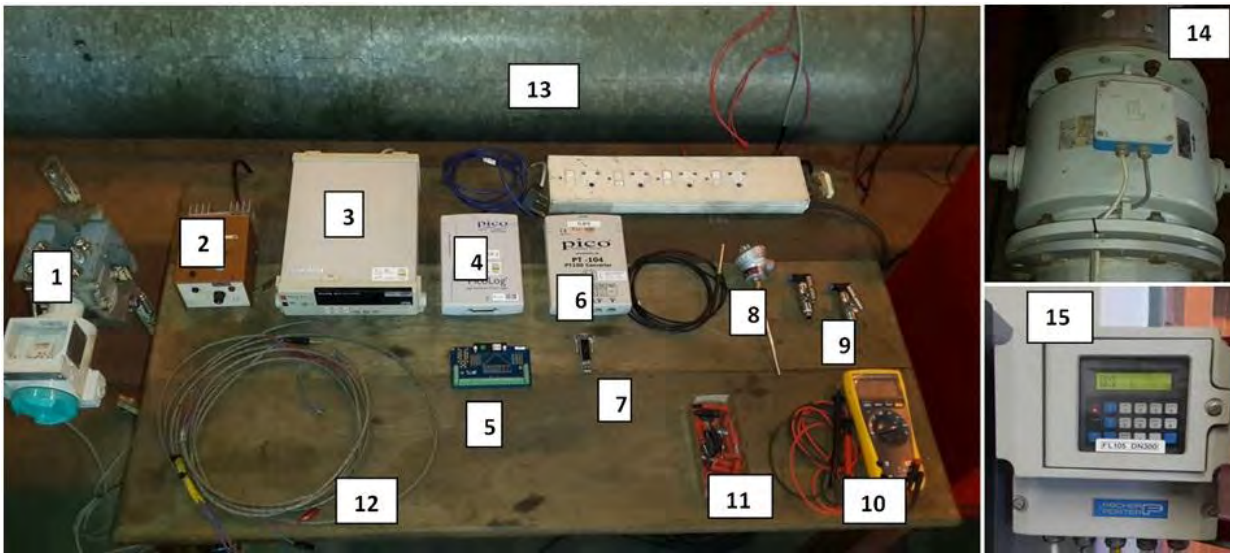

Item	Description	Function
1	DP Transducer	Converts differential pressure into a 4-20mA signal to be measured by the data logger
2	24V DC Power Supply	Current loop power supply (DC current to data logger, DP transducer, PT 100 converter)
3	Digital Multimeter	Used to confirm the measurement reading from the data logger off the pressure transducer
4	Data logger	Measures the different 4-20mA signals from respective converters
5	4-20mA current terminal connector	Connects 4-20mA signals to the data logger
6	PT 104	Converts mV signal from PT 100 thermocouple into a digital temperature signal
7	Serial to USB adaptor	Adapts a serial connection to a USB port
8	PT 100 Thermocouple	Platinum resistor to measure the water temperature (0ºC = 100Ω) and thus calculate the water mass density
9	Valves	To switch between the two yaw probe static pressure/ports
10	Multimeter	Checks continuity in cables
11	Wire end connectors	Wire end connectors
12	Cabling	Transmits the respective signals from measuring components
13	Ø400 mm Test line	Pipe where calibration and experimental measurements will take place
14	Secondary flow meter (electromagnetic meter)	Flow sensor used to confirm the flow rate during test runs
15	Flow to mA converter	Converts flow into mA signal to be measured by the data logger

Figure 77: Physical test instrumentation

Once the flow stability had been achieved, twenty three readings of each measurement point, at intervals of 10 seconds, were recorded and averaged. That averaged reading was considered to be a single, steady-state local measurement. The following tables are a summary of the different types of experiments conducted as a function of traversing path and flow. The average velocity is that which was reported by the magnetic flow sensor.

Table 4: Summary of flow conditions and traversing paths considered downstream of the 90° bend

D_{pipe} 395mm	**36L/s** (V_{ave}=0.3m/s) Re=10^{5}	**108L/s** (V_{ave}=0.9m/s) Re=$10^{5.5}$	**180L/s** (V_{ave}=1.47m/s) Re=$10^{5.75}$	**225L/s** (V_{ave}=2.08m/s) Re=$10^{5.9}$	**325L/s** (V_{ave}=2.65m/s) Re=10^{6}	**395L/s** (V_{ave}=3.23m/s) Re=$10^{6.1}$
+0°	2D, 6.6D, 11D	2D, 6.6D, 11D	2D, 6.6D, 11D	2D, 6.6D, 11D		
+30°	2D, 6.6D, 11D	2D, 6.6D, 11D	2D, 6.6D, 11D	2D, 6.6D, 11D		
-30°	2D, 6.6D	2D, 6.6D	2D, 6.6D	2D, 6.6D		
+45°	2D, 6.6D, 11D, 30D	2D, 6.6D, 11D, 30D	2D, 6.6D, 11D, 30D	2D, 6.6D, 11D, 30D	2D, 6.6D, 11D, 30D	2D, 6.6D, 11D, 30D
-45°	2D, 6.6D	2D, 6.6D	2D, 6.6D	2D, 6.6D		

At one stage the probe got damaged and had to be repaired. This reduced the available time for tests, hence it was not possible to complete all the tests in the matrix (Table 4).

8.3 Test results and processing

8.3.1 Calibration results

Calibration tests were conducted at different flow conditions at 35D away from a flow straightener, as shown in the shaded part of Figure 69. A single vertical traverse was performed, as it can be assumed that the flow is fully developed and symmetrical.

The results obtained from the experiments are shown in Figure 78. The velocity flow profiles are of a parabolic shape, as expected under calibration conditions. However, some abnormalities or outlying velocity measurements were identified. These are indicated as A, B, C and D in Figure 78. The curves for a velocity 2.08m/s and 2.65m/s indicate a distorted flow profile at maximum insertion depth of the probe. This can be attributed to the fact the probe has a 50mm tip offset ,as shown by Figure 72, whereby the tip of the probe makes contact with the pipe inner wall.

During the experiment, it was witness that the probe vibrated at the respective insertion depths represented as distortions in Figure 78. Multiple runs were done to confirm the phenomenon, and it was found that it was not just an accidental measurement error but rather some physical occurrence. Of interest was that the phenomenon seemed to be a function of the probe insertion depth or the exposed probe with its natural frequency.

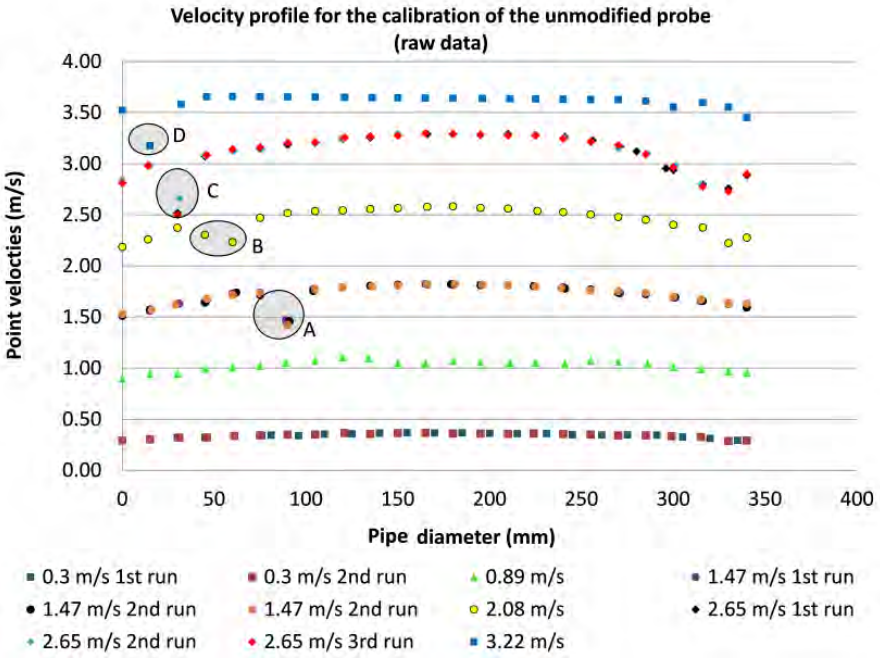

Figure 78: Unmodified probe calibration velocity profiles (raw data)

Furthermore the repeatability of the measurements is consistent with the vibration of the probe and the respective velocity. By comparing the integration of the flow profile including outliers and excluding outliers, it was found that the results where outliers were included, produced a higher mass flow rate error.

It was then postulated that the outlying velocity measurements were due to the probe vibrations as a result of vortex shedding around the probe.

The outlying velocity measurements are therefore not the actual flow conditions, and should be ignored for calibration purposes. A smoothing technique was utilized to produce the results shown in Figure 79. The technique involves mirroring the velocity data along the radius of the pipe such that the flow profile is symmetrical.

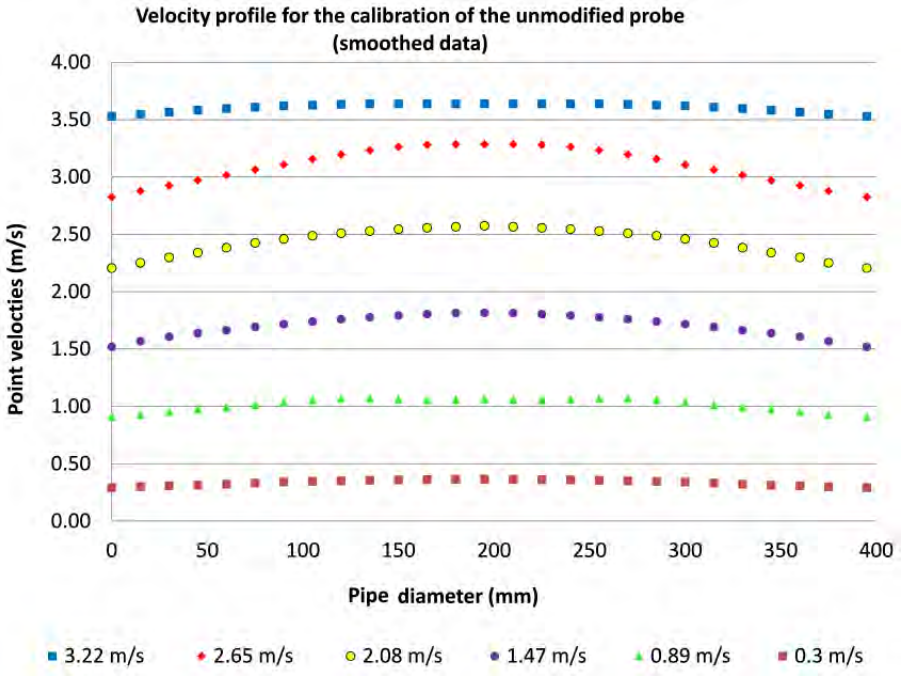

Figure 79: Unmodified probe calibration velocity profiles (smoothed data)

The corresponding pipe Reynolds numbers to the velocities in Figure 78 and Figure 79 are recorded in Table 4.

Figure 80 shows the difference between the reference and measured mass flow rate at various Reynolds numbers Re_{probe_D} i.e. with respect to the probe diameter. The measured mass flow rate was calculated from the smoothed data as a result of the rationale that is explained above.

Also indicated in Figure 80, are the measurement errors, where negative errors indicate that the measured mass flow rate is less than the reference mass flow rate vice versa.

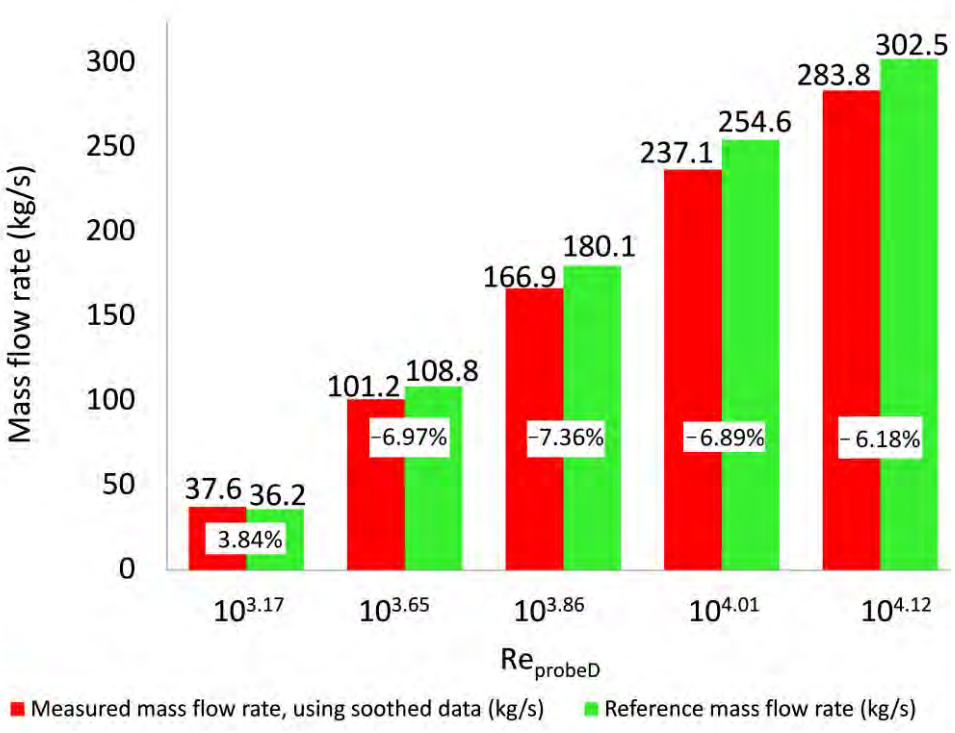

Figure 80: Reference vs. measured (calculated from smoothed data) results

At this point the calibration factor K is introduced, which is the ratio between the measured mass flow and the reference mass flow, for a given range of flow rate. Thus the calibration factors, for the considered range of Re_{probe_D}, were obtained by correcting the measured mass flow rate based on the reference mass flow rate. They are shown in Figure 81.

Figure 81 shows results that are consistent with the results indicated in Figure 80. In other words, K>1 when the measured mass flow rate is greater than the reference mass flow rate. The opposite is true.

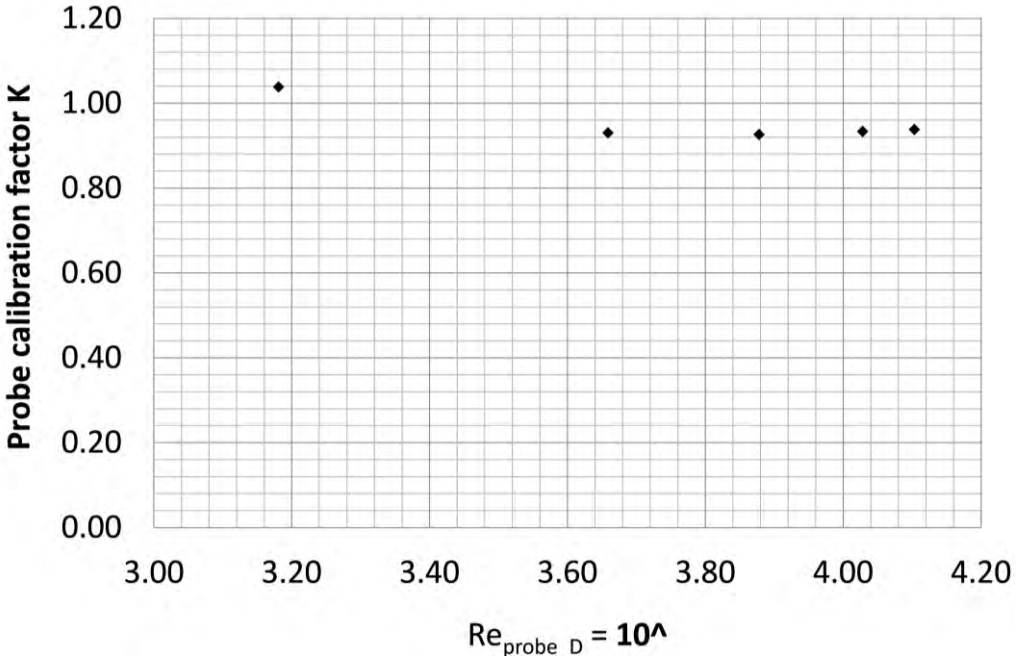

Figure 81: Calibration factor K vs. Probe Reynolds number

The corrected measured mass flow rate. $M_{corrected,}$ is thus

$$M_{corrected} = \frac{M_{measured}}{K} \tag{51}$$

8.3.2 Experimental results

Selected results obtained from the experiments are shown in Figure 82 (a)and (b) and Figure 84. Additional results are provided in the Appendix. Unlike with the calibration of the probe, the Reynolds number Re in the following graphs is based on the duct diameter and not the probe diameter.

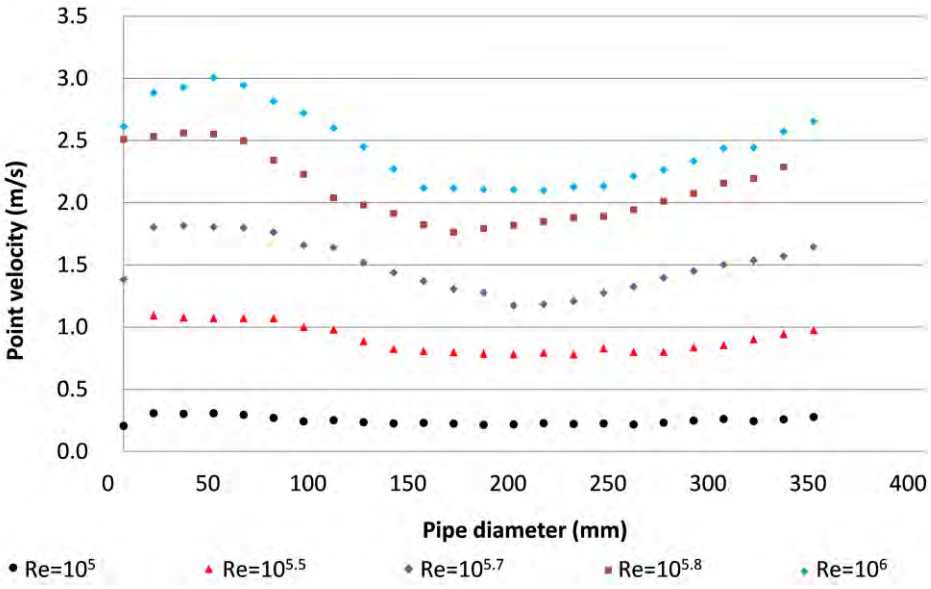

(a)

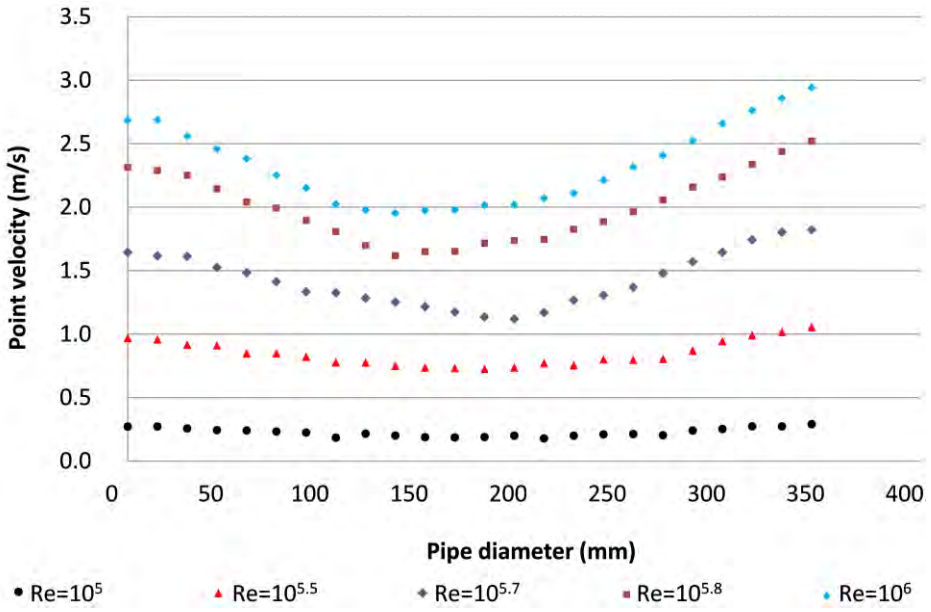

(b)

Figure 82: Experiment flow profile comparison at 2.2D after a 90° bend for (a)-45° traverse (b) +45° traverse

It is clear from Figure 82 that the shapes of the velocity profiles (a) and (b) are a result of the ±45° traverses shown in Figure 83. The high velocity intensities shown as A in Figure 83 result in higher velocity measurements close to the inner wall of the pipe than in those measurements close to the outer wall, as represented in Figure 82 (a).

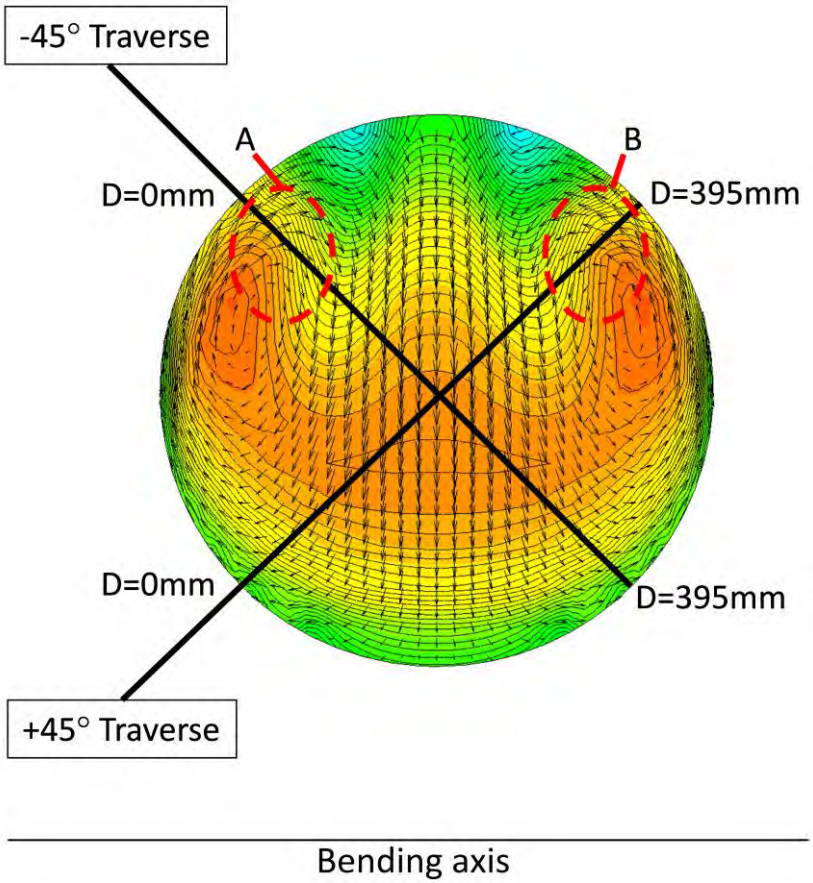

Figure 83: Velocity intensities at 2.2D for ±45° traverses

Conversely, the high velocity intensities shown as B in Figure 83 result in higher velocity measurements close to the outer wall of the pipe than in those measurements close to the inner wall, as represented in Figure 82 (b).

It is important to note that Figure 83 and Figure 84 are meant to illustrate the typical flow profile associated with the two ±45° traverse and the single 90° traverse respectively. The chosen Reynolds number for this CFD illutration, shown by Figure 83 and Figure 85, was $Re=10^6$. This was the safest Reynolds number possible during the physical test to avoid catastrophic damages to the probe. In addition, the aim was to also satisfy the typical Reynolds number on site shown by Equation (24).

The velocity profile results shown in Figure 84 represent the experiment results from a 0° traverse at 2.2D after a 90° bend.

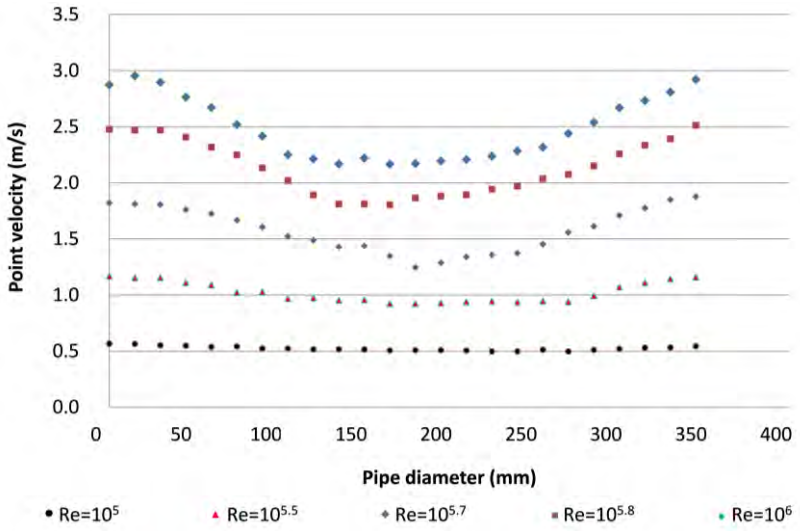

Figure 84: Experiment flow profile comparison at 2.2D after a 90° bend for 0° traverse

There are two velocity peaks close to the inner and outer wall, shown in Figure 84. These peaks are a result of the two high velocity intensities shown as A and B in Figure 85, where the 0° result intersects.

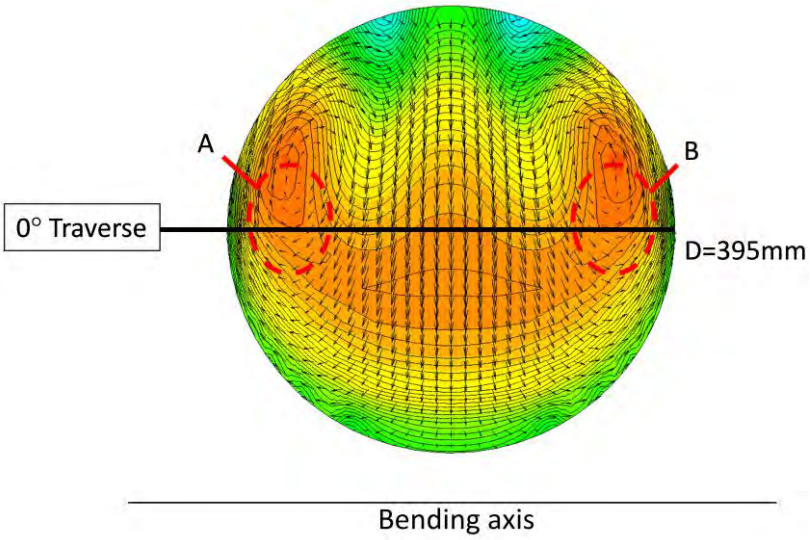

Figure 85: Velocity intensities at 2.2D for a 0° traverse

It can be noted in further test results (see Appendix D) that the respective flow profiles look reasonably similar to that of the profiles at a higher flow velocity. The results further show a flat profile most of the time. This suggests that the algorithms will not make any significant approximation errors.

8.3.3 Processing of results

Not all the results that were obtained made practical sense; hence the following criteria were used to rejected suspect test points:

- Known physical causes: air in a manometer, for example, led to readings being omitted as they were considered false readings [32] and re-measurements being done.
- Flow range limitations: these demanded that care was taken to avoid operating outside the specified flow range of the differential pressure transducer.
- Statistical outliers: test points were examined on the basis of their deviations from the least-squares line. A point that fell outside the specified confidence limit was re-examined together with adjacent points to see if there were any grounds for accepting that point. If not, such a test point would be omitted from the subsequent analysis [32]. A smoothing technique explained in Chapter 8.3.1. was used during the calibration of the probe.
- Outliers that were caused by probe vibrations.

8.4 Probe vibration errors

It was noted that the point velocity measurements indicated by "A", "B", "C", and "D" in Figure 78 were indeed affected by the vibration of the probe. Whenever the probe vibrated vigorously, the vibration points correlated with a sudden inconsistent measurement of the local point velocity. The following paragraphs aims at confirming this observation by relating the vortex shedding frequency with the natural frequency for vibration.

The vortex shedding frequency can be determined from [15]

$$f_{st} = \frac{S_{st} V_{ave}}{d_{out}} \tag{52}$$

The Shrouhal number (S_t) was estimated from Figure 86 for a smooth probe diameter at the respective Reynolds number.

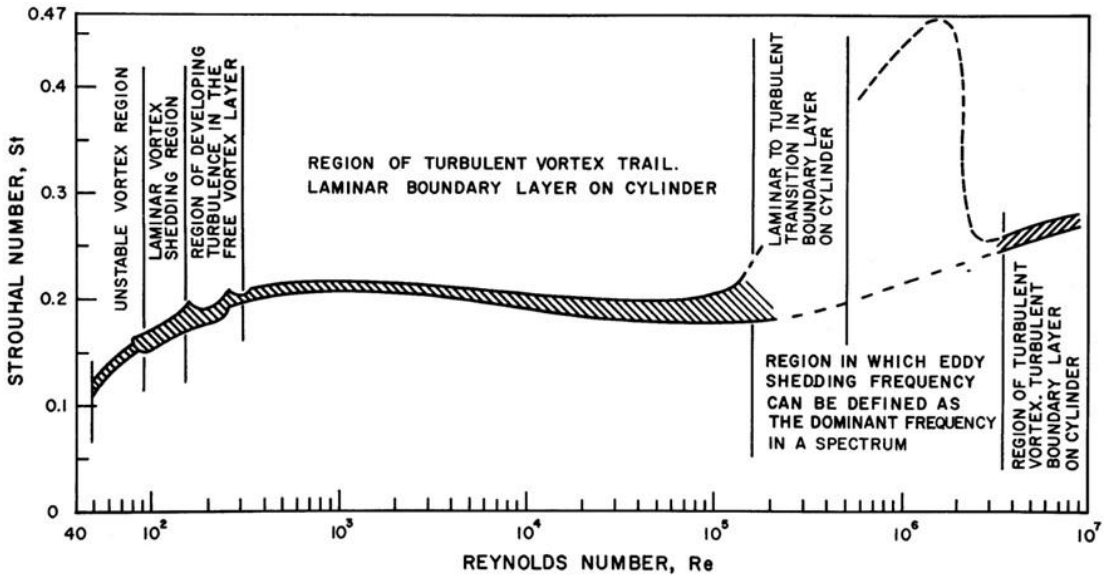

Figure 86: Relationship between Shrouhal number and Reynolds number for circular cylinders [15]

During the course of the tests, the probe got damaged due to the high flow rates and vibrations. The probe was repaired using a permanent stainless steel sleeve and then recalibrated. Unfortunately, this meant that is was not possible to obtain or measure the natural frequency of the unmodified probe. The natural frequency had to be calculated and estimated from measurable data.

The probe was modelled as a cantilever beam as shown below.

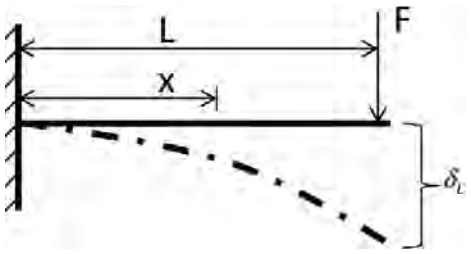

Figure 87: Deflection of a cantilever beam [33]

Consider the cross sectional area of the cylindrical probe with three pressure ports as shown in Figure 88. The probe has an inner radius r_1 and outer radius r_2 with a thickness t, thus representing an annulus with an exposed length L. The probe further has an effective radius r.

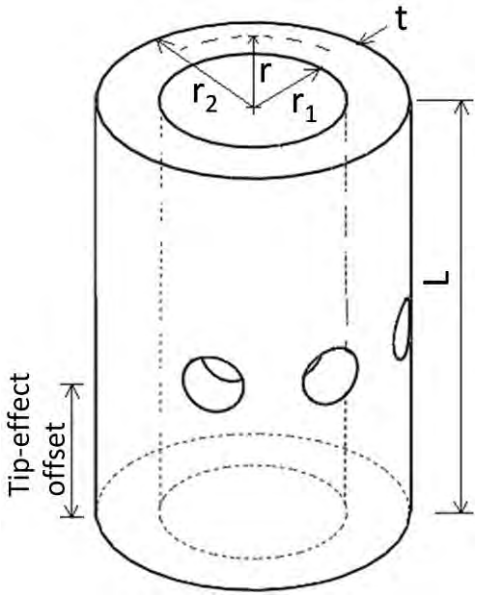

Figure 88: Cross section through cylindrical probe

Assuming the probe was a thin tube, the area moment of inertia for an annulus can be approximated as

$$I = \pi r^3 t \tag{53}$$

The un-damped natural frequency of a cantilever beam with mass *m* is given by

$$f_n = \frac{1}{2\pi}\sqrt{\frac{k_{eq}}{m}} \tag{54}$$

and the equivalent stiffness k_{eq} is given by

$$k_{eq} = \frac{3EI}{L^3} \tag{55}$$

The cross sectional area of the annulus is

$$A_{cross} = 2\pi rt \tag{56}$$

and the mass of exposed probe length is

$$m = \rho A_{cross} L \tag{57}$$

By inserting Equations (53), (55), (56) and (57) into Equation (54), the natural frequency of a the exposed thin wall probe is

$$f_n = \frac{1}{2\pi}\sqrt{\frac{3Er^2}{2\rho L^4}} \tag{58}$$

Note that the wall thickness *t* cancels out, leaving only the probe radius *r* as an unknown. However, this is an equivalent radius, not to be confused with the actual probe outer radius. In Chapter 8.3.1, it was postulated that resonance occurs at different probe insertion depths for various flow conditions. Thus a conservative approach was taken to determine the effective radius r. By manipulating Equation (58), it is possible to calculate the effective radii corresponding to the various exposed probe length and average flow velocities. The different effective radii were calculated by

$$r_i = \sqrt{\frac{8\pi^2\rho\left(f_{st_i}\right)^2\left(L_i\right)^4}{3E}} \tag{59}$$

L_i and f_{st_i} are the insertion length and corresponding vortex shedding frequency as observed from the tests at different velocities V_i. Note that the exposed length is the measurement position as reported in Figure 78 , plus the length of the probe extending beyond the measurement holes, which was 50mm. Since the effective radius is a geometric property of the probe and assumed to remain constant, an average of the various effective radii was calculated for the four flow velocities considered. The results of the vibration analysis are thus summarized in Table 5.

Table 5: Summary of vibration analysis

n	Test velocity (m/s)	Vibration depth (mm)	Exposed length (mm)	Effective radius (mm)
1	3	15	65	0.811
2	2.5	30	80	0.953
3	2.08	60	110	1.5
4	1.47	90	140	1.717
			Average	1.2

Figure 89 plots both Equation (52) and (58) on the x-axis, and the probe length and average flow velocity on the y-axis. If for example the average flow velocity is 3 m/s, the vortex shedding frequency is 124 Hz. Thus the corresponding exposed probe length or insertion depth of the probe, where resonance occurs, is approximately 100mm. This is illustrated by line A in Figure 89.

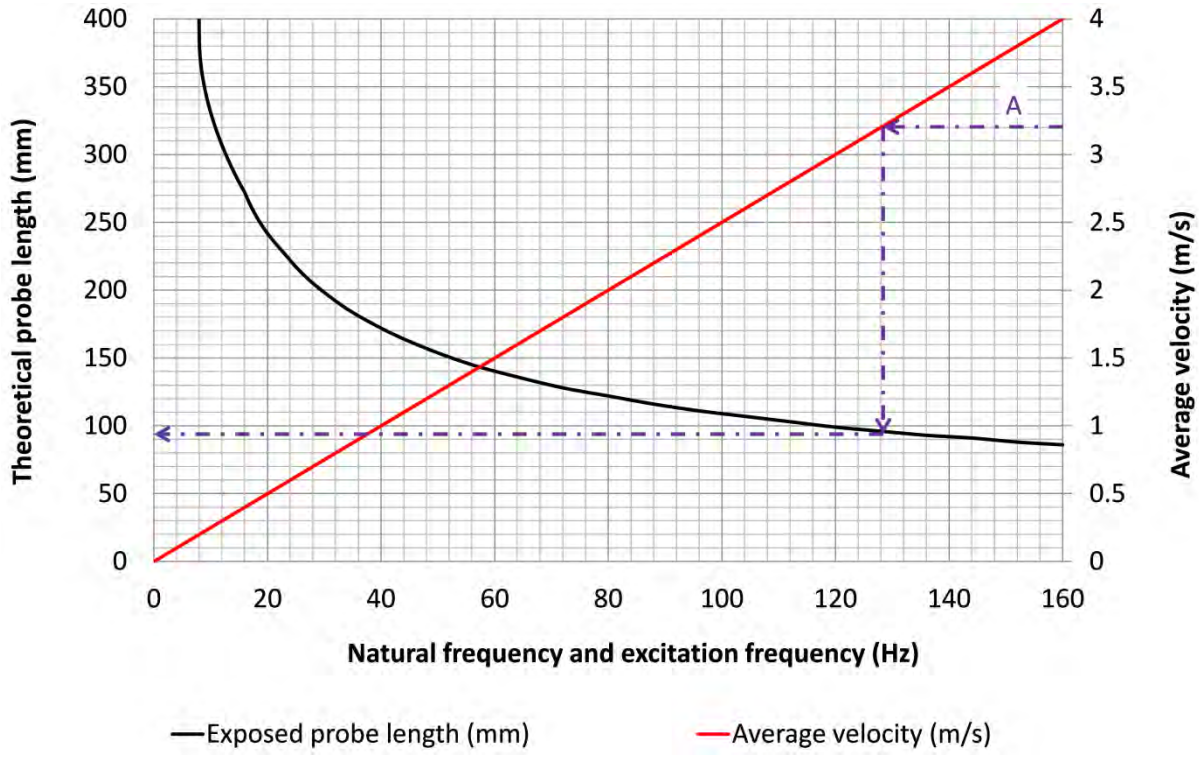

Figure 89: Probe vibration analysis (theoretical)

Using the average effective radius and above method, the insertion depth where vibration is expected to occur for a certain test velocity was calculated. Figure 90 is a repetition of Figure 78 but with these predictions added. Although the predicted points do not lie exactly on the measured locations, the trend is similar.

It can therefore be concluded that vortex-shedding induced vibration was indeed the cause of the anomalies seen in the tests. As was in the case of Figure 78, the curves for a velocity 2.08m/s and 2.65m/s shown in Figure 90, indicate a distorted flow profile at the maximum insertion depth of the probe. This was attributed to the vibration of the probe. Thus the outlying points can therefore be excluded from measurements, as they are not a true reflection of the local flow velocity.

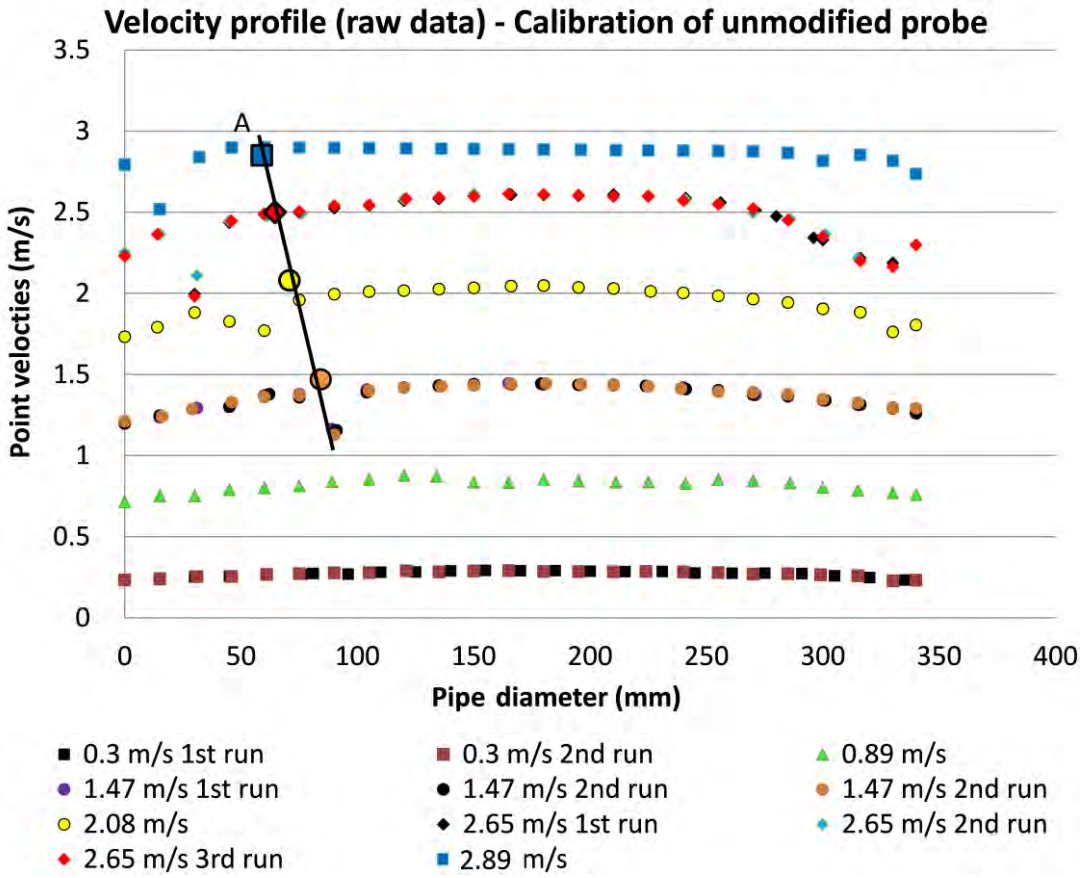

Figure 90: Probe vibration analysis results

Flow measurements where probe vibrations exist can be improved by the following interventions:

- increase the probe stiffness;
- avoid measurements where vortex shedding frequency around the probe equals the natural frequency of the probe; and
- note the vibration of the probe and discard outlying velocity measurements resulting from the vibration.

8.5 Summary of test results

A summary of the test results is shown in Figure 91. The error between the measured mass flow rate and the test reference flow rate, is indicated for the various completed test conditions. The results shown are those for: different traversing paths; different measurement locations after the bend; and various Reynolds numbers.

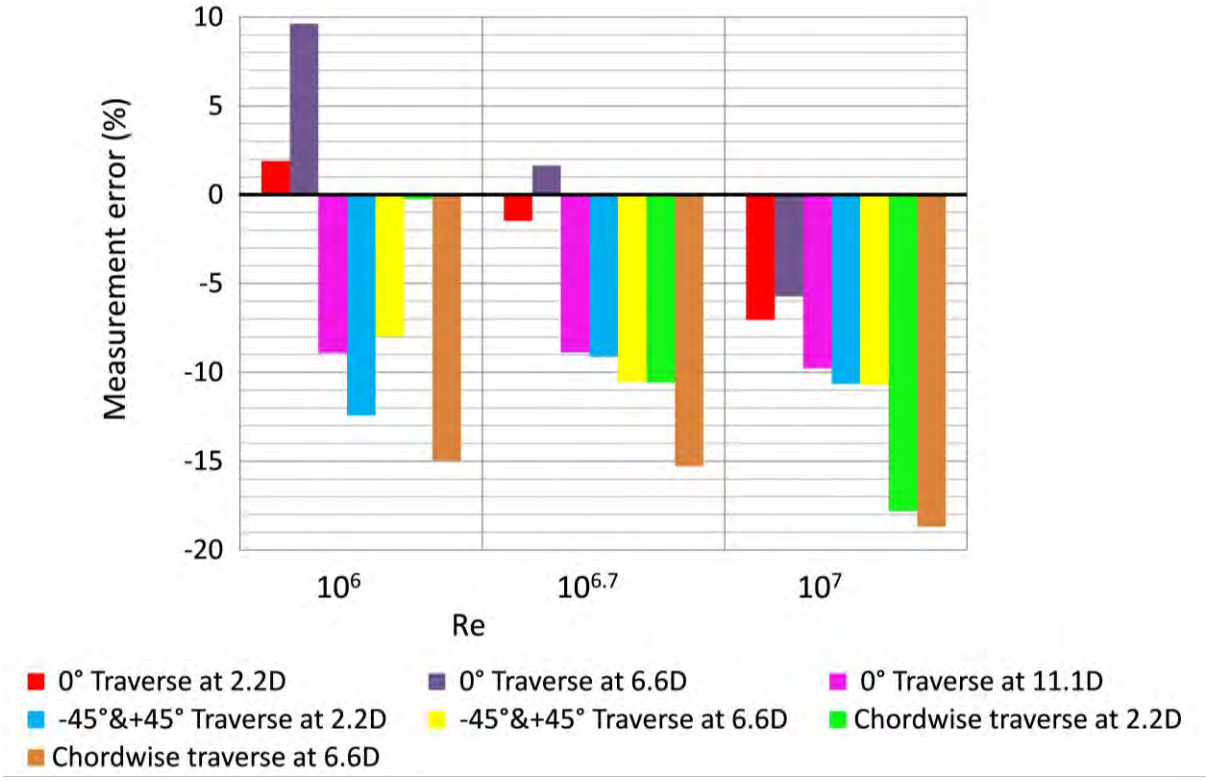

Figure 91: Measurement error for various traverses at given Reynolds numbers

The results show that the two ±45° traverse scheme provides consistent measurement percentage errors over the considered Reynolds numbers. In Chapter 8.3.2 it was discussed and shown by Figure 82 and Figure 83 that the ±45 ° traverses are more likely to sufficiently capture the flow dynamics compared with the other traversing paths. This may have attributed to the lower measurement errors and consistency relative to the other traversing paths.

Figure 67 in Chapter 7.5, which shows the static errors obtained from implementing the CFD simulations into the algorithm, further shows that the ±45° traverses provide relative low measurement errors and consistent results.

Consider the chord-wise traverses at 6.6D with $Re=10^6$, applying a static compensation, through Equation (49) as discussed in Chapter 7.5, on the measured flow rate gives the following results shown in Table 6.

Table 6: Application of static error compensation

Chord-wise traverses at 6.6D with $Re=10^6$	
Test reference mass flow rate measurement (kg/s)	108.83
Test mass flow rate measurement (kg/s): (see Appendix D)	94.66
Static error (%) at 6.6D for respective Reynolds number (see Appendix C)	-12.132
Compensated test mass flow rate measurement (kg/s)	107.73

It is important to note that the sign convention utilized is such that a negative static error represents an underestimation of the reference flow rate or in this case, the test reference mass flow rate. The results show an improvement on the measured flow rate when applying a compensation. However the additional error, after compensation, can be attributed to insufficient measurement points taken, as well as the instrument uncertainty and errors.

8.6 Tolerance due to number of measurements

Assuming that the static error compensation is a valid approach, one still has an additional tolerance to the result due to the number of measurements taken.

Figure 92 shows the typical curve of the error produced by one of the integration algorithms (see Figure 61 for example). If $\#n_1$ measurement points are made, the expected uncertainly would be 1%, while $\#n_2$ points will result in 2% uncertainty. One can therefore add a band around the compensated result to show the possible minimum and maximum measured result.

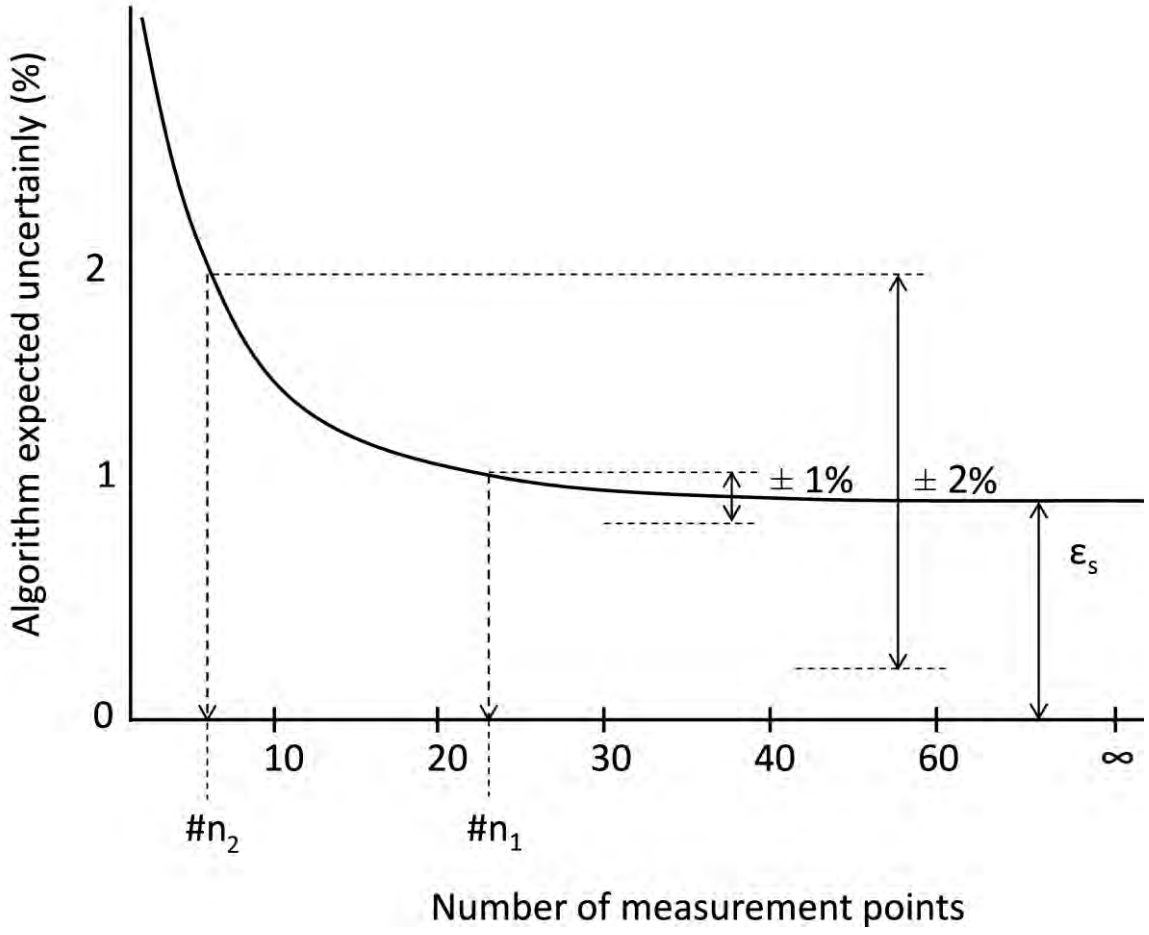

Figure 92: Static error compensation illustration

For the chord-wise traverse at 6.6D, a total of 26 points were taken. From Appendix B, the corresponding tolerance band is about 3% for $10^6 \leq Re \leq 10^7$. Consider the static compensation indicated in Figure 92, applying this tolerance band to the compensated results produces Figure 93 below.

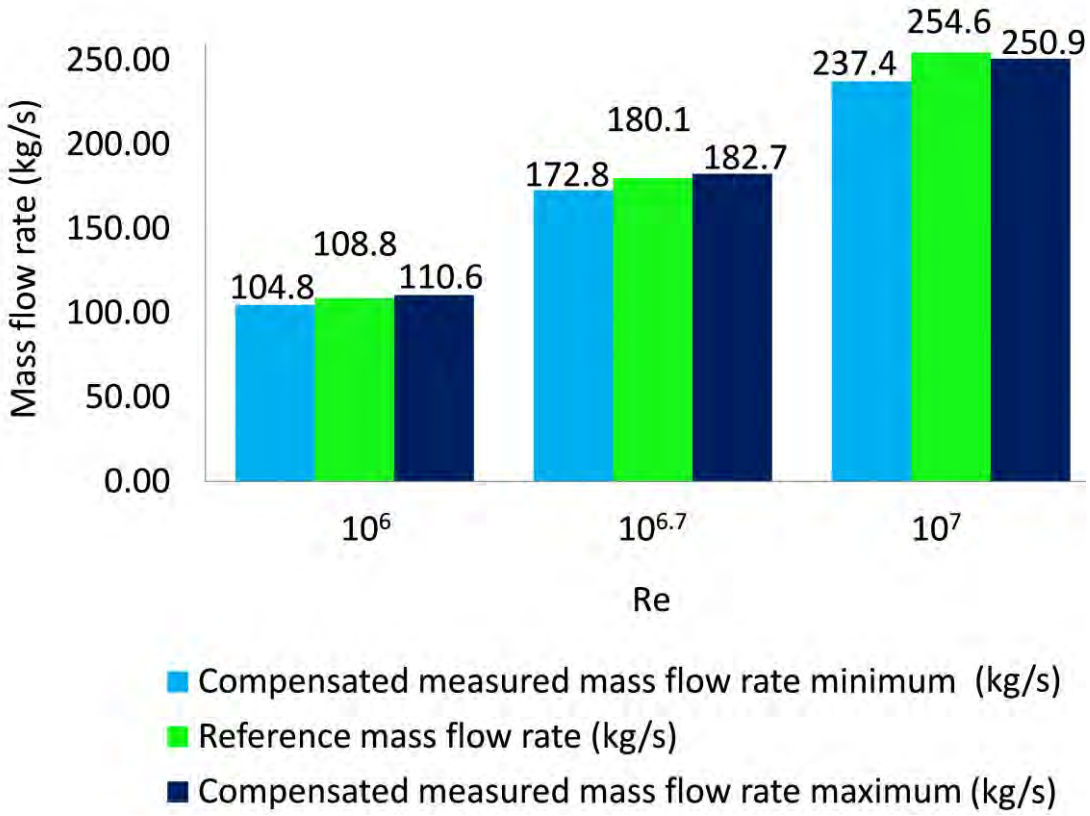

Figure 93: Compensated test results for chord-wise traverse at 6.6D

Figure 93 indicates how the reference mass flow rate, which was measured by an electromagnetic flow meter, compares to the minimum and the maximum of the compensated test mass flow rates. It can be seen, from Figure 93 that the reference mass flow rate is very close to the tolerance band.

However it was also found in other cases, e.g. the ±45° traverse tests at 20D that the reference mass flow rate lies outside the tolerance bandwidth of the compensated minimum and maximum test mass flow rate. This means that the tests conducted do not successfully validate the proposed compensation technique. The additional error is probably due to instrumentation errors. This re-enforces the fact that it is quite difficult to achieve very accurate flow measurements in practice.

A summary of the compensated test results for chord-wise traverse at 6.6D is provided in Table 7.

Table 7: Summary of compensated test results for chord-wise traverse at 6.6D

Chord-wise traverses at 6.6D			
Reynolds number	10^6	$10^{6.7}$	10^7
Reference mass flow rate (kg/s)	108.83	180.14	254.62
Probe measurement (see Appendix D) (kg/s)	94.67	156.25	214.51
Predicted accuracy at 26 measurement points (± %)	2.71	2.77	2.77
Static error at 6.6D for respective Reynolds number (see Appendix C)	-12.13	-12.12	-12.16
Compensated measured mass flow rate (minimum) (kg/s)	104.82	172.87	237.45
Compensated measured mass flow rate (maximum) (kg/s)	110.66	182.72	250.98

One has to remember that the purpose of the tests were not to irrefutably confirm the developed theory, but rather to test the theory in a limited scope in an actual application. A much more thorough test with accurate measurements would be needed to fully validate the theory presented here.

9. Conclusion and Recommendations

The main aim of the project was to develop a flow rate measuring technique for CW ducts and recommend a less intrusive flow meter that could be implemented at Eskom power stations. This was a result of the lack of flow measurement devices currently installed on Eskom Power Station for reasons stated in Chapter 1.

A literature survey into the various state of the art of technology of flow measurement techniques was successfully conducted. The survey was focused on flow measurement techniques suitable for application in the CW ducts at various Eskom power stations.

In order to identify a less intrusive method for measuring the flow rate in CW ducts, some constraints, reported in Chapter 2.3, had to be taken into consideration. These include the size of the meter pit, which affects the dimensions of the recommended measuring equipment, e.g. traversing angles and length of measuring device (refer to Figure 16). Furthermore since the flow profile in the CW ducts was unknown, the research then focused on a local flow measurement technique.

An added deciding factor to the measurement technique was accessibility, which made the local flow measurement technique the option of choice. The selected measurement device was a pitot tube and a summary of the type of technologies studied in this research are summarised in Table 1.

It was found that are a multitude of flow meters on the market. The instrument selection criteria may include:

- the required measurement accuracy;
- capital cost;
- flow medium and operating conditions;
- range of the flow to be measured; and
- final installation.

Pursuant to the selection of the pitot tube, the author conducted a study on the mechanical design of the probe. Equation (21) was developed to calculate the minimum outer radius of the probe with a given wall thickness, allowable bending stress and an average flow velocity through a pipe.

Three algorithms were developed in order to predict the flow measurements accuracies in the CW ducts, they were: a single 0° traverse; two ±45° traverses; and a chord-wise traverse.

The bandwidth or tolerance of flow measurement accuracy as shown in Figure 93 and Table 7 is based on:

- the number of traverses across the CW duct;
- the number of flow measurement points along the traverse;
- the position of flow measurement devices downstream of a bend; and
- the path of the traverses (i.e. 0° traverse, ±45° traverse and chord-wise traverse).

In developing the three mentioned algorithms, it was necessary to perform CFD simulations of the flow through a 90° bend. The CFD simulations conducted in this research were in order to predict the flow profiles in the CW ducts. Therefore the flow patterns were not studied since the author only required point velocity data to use as inputs in the development of the algorithms. The existing plant data could not be used to develop the algorithms since such data is not properly recorded nor is it reliable.

The CFD model was compared to findings in literature. This included experimental work by Rütten et al. [21] and Squire [23]. The correlation found between the CFD model in this research and the existing experimental work in the literature, provided confidence in the CFD model.

In order to verify the developed algorithms, the following were used:

- an analytical solution in the form of the one-seventh power-law velocity profile equation to verify the single 0° traverse through the centre of the pipe;
- CFD results to verify the two ±45° traverses; and
- a 3D CAD model to verify the chord-wise traverse.

Physical tests were performed at the Eskom Water Flow Calibration Laboratory. The tests were performed at flow conditions similar to those considered in the CFD simulations. Test investigations were conducted at: 2.2D; 6.6D; 11.1D and 20D downstream of a 90° bend.
It was during these physical tests where the author witnessed an interesting phenomenon in the flow measurement results. It was found that the vibration of the probe affects the flow measurements. Subsequent to the discovery of the phenomena, it was possible to predict the insertion depths at which vibrations will occur for given flow rates. This analysis is documented in Chapter 8.

It was found that probe vibrations may introduce outlying point velocities that do not represent the dynamics of the flow, thus contributing to erroneous flow rate measurements. It is therefore recommended that test personnel take cognisance of this risk.

In this research, it was found that flow measurement accuracy is dependent on the distance of the measurement from the bend and the traversing path. In particular, measurements conducted very close to the bend were investigated. It was found that such measurements are not recommended owing to high flow re-circulations which may introduce inconsistent flow measurement errors. It is therefore recommended that measurements be taken at least 2.2D downstream of a 90° bend, since the flow profile improves with distance downstream of the bend. This is not necessarily a new observation.

The 90° traverse is suitable for flow measurements close to the bend. For measurements more than 2.2D downstream of the bend, the 0° traverse and multiple traverses of two traverses at -45° and +45° to the plane of bending, are recommended. Furthermore, the multiple traverses offer more consistent and more reliable measurements. This was deduced from the relatively low and consistent static error in flow rate measurement approximation results.

The predictions or measurement approximations in this research are limited to a Reynolds numbers range of $Re=10^{5.5}$ to $Re=10^{7}$ and error of 0% to 10%. Nonetheless for the studied range of Reynolds numbers, it was predicted that a minimum of 32 measurement points, equally spaced, would produce measurement accuracy equal or less than 1% for all but the chord-wise traverse. This however is not valid for measurements at 0D and 2.2D after a 90° bend.

The chord-wise traverse option had the potential benefit of requiring only one access hole for the probe, and could work well in the confined spaces. However, the discretization and integration scheme does not seem to produce better results than a single vertical traverse.

Future work exists to fully validate the algorithms by conducting accurate experimental tests. More work can be done in refining or improving the chord-wise technique in order to decrease the approximation errors associated with the assumptions made in Chapter 5.3 of this report. Furthermore, investigations can be conducted for a range of Reynolds numbers not restricted to site operating conditions.

10. References

[1] Janusz M. Gasiorek, John A. Swaffield, Lynne B. Jack John F.Douglas, *Fluid Mechanics 5th Edition*. London: Longman, 2005.

[2] John G. Webster, *The Measurement, Instrumentation and Sensors Handbook*. Boca Raton: CRC Press LLC, 1999.

[3] Yusus A. Cengel and JohnM.Cimbala, *Fluid mechanics: fundamentals and applications, 1st Ed*. New York: McGraw Hill, 2006.

[4] Chipkin Automation Systems. (2010, May) Newsletter. [Online]. http://www.chipkin.com/newsletter/may-2010-newsletter/

[5] ABB. (2005) Flow meter technology selection.

[6] B.K. Gandhi, S.N. Singh, Ratnesh K. Pandey A. Seshadri, "Analysis of the effect of body shape on annubar factor using CFD," *ELSEVIER*, vol. Measurement, no. 35, pp. 25-32, 2004.

[7] R.G. Folsom, "Review of the Pitot Tube," in *Fluid Meters Research Committee*, Chicago, 1955, pp. 35-51.

[8] The Bristish Standards Institution, ISO 3966:2008: Measurement of fluid flow in closed conduit - Velocity area method using Pitot static tubes, 2008.

[9] The engineering toolbox. (2015, May) The engineering toolbox. [Online]. http://www.engineeringtoolbox.com/factors-safety-fos-d_1624.html

[10] The Bristish Standard & Switzerland Institution, ISO 5168:2005 Measurement of fluid flow-Procedures for the evaluation of uncertainties, 2005.

[11] The Bristish Standards Institution, ISO 7194:2008: Measurement of fluid flow in closed conduits - Velocity-area methods of flow measurement in swirling or asymmetric flow conditions in circular ducts by means of current-meters or Pitot static tubes, 2008.

[12] Paap Tekno Trading. (2014, May) http://www.paab.com/. [Online]. http://www.paab.com/dokument/bibliotek/Flodesmatning/introduction_itabar_en.pdf

[13] L.N. Mabuza, "Hot Tapping of Cooling Water System Ducts Standard," Eskom, Johannesburg, Standard 240-61227267, 2013.

[14] Magnetrol, "Thermal Dispersion Mass flow Measurement Handbook," Illinois, 2012.

[15] John H Lienhard, "Synopsis of lift, drag, and vortex frequency data for rigid circular cylinders," Washington, 1966.

[16] Darelle T.Janse van Rensburg, "Lethabo power station-Corrosion and coating insoection of the eastern side cooling water ducts," Orytech (Pty) Ltd , Johannesburg, Inspection ORY18609, 2009.

[17] Keith Northcott, "Corrosion protection case history study-Letahabo power station," Eskom, Johannesburg, Case study No.3, 2004.

[18] D.T. Janse van Rensburg, "Duvha power station-orth side visual inspection of CW duct coatings," Eskom, Johannesburg, Inspection TRR/S96/083, 2009.

[19] D.P. Erhard et al., *Prandtl-essentals of fluids mechanics, 3rd Edition*. New York: Springer, 2010.

[20] Donald F. Young, Bruce R. Munson, Theodore H. Okiishi, and Wade W. Huebsch, *A brief introduction to fluid mechanics 5th Ed*. United States of America: John Wiley and Sons, 2011.

[21] Frank Rütten, Matthias Meinke, and Wolfgang Schröder, "Large-eddy simulations of 90° pipe bend flows," *Joural of Turbulence*, vol. 2, no. N3, pp. 2-14, 2001.

[22] M.Rowe, "Measurements and computations of flow in pipe bends," *Journal of Fluid Mechanics*, vol. 43, no. Part 4, pp. 771-783, 1970.

[23] H. B. Squire, "Note on secondary flow in a curved circular pipe," *Unpublished British Aero. Res. Council*, no. 16601, 1954.

[24] H.G. CUMING, "The secondary flow in curved pipes," *Aeronautical Research Council Reports and Memoranda*, pp. 1-4, 1952.

[25] S.V. Patankar, V.S. Pratap, and D.B. Spalding, "Prediction of turbulent flow in curved pipes," *Journal of Fluid Mechanics*, vol. 67, no. 3, pp. 583-595, 1975.

[26] k Sudo, M Sumida, and H Hibara, "Experimental investigation on turbulent flow in a circular-sectioned 90° bend," *Experiments in fluids*, vol. 25, no. 1, pp. 42-49, 1998.

[27] Cooling Technology Institute, "Standard for Liquid Flow Measurement," Houston, 2008.

[28] Deerfield High School. (2014, August) Deerfield High School. [Online]. dhs.dist113.org/Faculty/SummyJ/Documents/./calc_5-4_ln_answers.pdf

[29] Allen. (2011, September) Allen Math Blog. [Online]. http://allenmathblog.wordpress.com/2011/09/30/

[30] Physics Forums. (2005, October) Physics Forums. [Online]. https:www.physicsforums.com/threads/finding-the-area-of-a-triangle-using-determiants.96957/

[31] John J. Bloomer, *Practical fluid mechanics for engineering applications*, L.L. Faulkner, Ed. New York, United States of America: Marcel Deker, Inc, 2000.

[32] J M Hobbs, "Standard methods for calibrating flowmeters and testing pipeline components in water at NEL," East Kilbride, 1987.

[33] University of Cape Town, MEC4047F Mechanical Vibrations Course Notes, 2014.

[34] Mark V. Zagarola and Alexander J. Smits, "Mean-flow scaling of turbulent pipe flow," *Journal of Fluid Mechanics*, vol. 373, pp. 33-79, 1998.

[35] Victor P. Head, "Multiple velocity traverse flow rate measuring technique," US4317178/A, February 23, 1982.

[36] F.R. DeJarnette J.C. Williams III, "The accuracy of type-S pitot tubes," North Carolina, 1977.

[37] Brian H. Welker, "Sensor probe and pipleine construction and method," US 7,194,920 B2, March 27, 2007.

[38] FIP FLSNET. Engineering info. [Online]. http://www.flsnet.it/?l1=3&page=tutorials

[39] John Eustice, "Experiments on stream-line motion in curved pipes," *Proceedings of the Royal Society of London*, vol. Series A, pp. 119-130, 1911.

[40] Bill Cox, Understanding engineering mathematics, 2001.

[41] ASME PTC 23-2003, Atmospheric water cooling equipment performance test codes, 2003.

[42] Anupam Sengupta, Flow Measurement Techniques, Department of Mechanical Engineering Indian Institute of Technology.

[43] The Bristish Standard & Switzerland Institution, BS4485 Part 2: 1988: Methods for performance testing, 1988.

[44] L.M. Liebenberg D.W.F. Senekal, Procedure for on-site verification of liquid flowmeters, 2007, Eskom Holdings SOC LTD.

[45] Darelle T.Janse van Rensburg, "Lethabo power station-Corrosion and coating insoection of the eastern side cooling water ducts," Orytech (Pty) Ltd, Johannesburg, Inspection ORY18609, 2009.

[46] Keith Northcott, "Corrosion protection case history study-Letahabo power station," Eskom, Johannesburg, Case study No.3, 2004.

Appendix A. Integration Algorithms

A.1. Verification of algorithm using analytical solution

Pipe diameter:

$D := 400mm$

Pipe radius:

$R_{max} := \frac{D}{2}$

Density of water:

$\rho_w := 999.4 \frac{kg}{m^3}$

Analytical solution

Flow velocity at the centre of the duct:

$u_{max} := 2.5 \frac{m}{s}$

Power law equation exponent corresponding to flow regime:

$z := 7$

Flow velocity obtained from Power Law:

$$u(r) := u_{max} \cdot \left(1 - \frac{r}{R_{max}}\right)^{\frac{1}{z}}$$

Exact mass flow from analytical solution:

$$M_{exact} = 2\pi \cdot \rho_w \int_0^R u(r) \cdot r \cdot dr$$

$$= -\tfrac{7}{4}\pi \cdot \rho_w \cdot R \cdot u_{max} \left(1 - \frac{r}{R}\right)^{\tfrac{8}{7}} \Bigg|_{r=0}^{r=R}$$

$$= \tfrac{7}{4}\pi \cdot \rho_w \cdot R \cdot u_{max}$$

Numerical solution

Discretization: number of measurement points (n):

$n := 100$

$f(n) :=$ | for $j \in 0..n$

$Y_j \leftarrow \frac{R_{max}}{n} j$

$R \leftarrow R_{max} - Y$

$U_j \leftarrow u_{max} \cdot \left(1 - \frac{R_j}{R_{max}}\right)^{\frac{1}{z}}$

for $i \in 1..n$

$r_i \leftarrow \frac{R_{i-1} + R_i}{2}$

$u_i \leftarrow u_{max} \cdot \left(1 - \frac{r_i}{R_{max}}\right)^{\frac{1}{z}}$

for $i \in 1..n-1$

$a_i \leftarrow \frac{\pi}{2} \cdot \left[(r_i)^2 - (r_{i+1})^2\right]$

$a_n \leftarrow \frac{\pi}{2} \cdot \left[(r_n)^2\right]$

$q_i \leftarrow a_i \cdot U_i$

$q_n \leftarrow a_n \cdot U_n$

$M_{est} \leftarrow 2 \cdot \left(\rho_w \cdot \sum q\right)$

$\%Error \leftarrow \frac{M_{est} - M_{exact}}{M_{exact}} \cdot 100$

A.2. Verification of algorithm using CFD results (single traverse)

Pipe diameter:

$D := 3000mm$

Pipe radius:

$R_{max} := \frac{D}{2}$

Density of water:

$\rho_w := 999.4 \frac{kg}{m^3}$

Exact mass flow used in the CFD simulation:

$M_{exact} := 15000 \frac{kg}{s}$

Data extracted from CFD:

$Data_{raw} :=$

0	9.6974E-19
0.000309708	0.029525436
0.026959527	1.307283673
0.157128951	1.586626543
0.287298375	1.808477507
0.4174678	1.945046336
0.547637224	2.038895952
0.677806648	2.10870733
0.829670976	2.169898952
0.959840401	2.211006791
1.111704729	2.247404487
1.285263961	2.277468099
1.479411597	2.297122172
1.522248155	2.298882572
1.588992618	2.301673848
1.784246754	2.298623107
2.001195795	2.281061368
2.261534643	2.24192984
2.760517436	2.154484276
2.890651487	2.092992018
2.945056959	2.072325984
3	6.93889E-18

```
Remove_zeros(V) := | K ← 0
                   | for P ∈ V
                   |   K_rows(K) ← P if P ≠ 0
                   | K
```

```
f_upper(Data_raw) := | n_raw ← last(Data_raw^⟨0⟩)
                     | Y_raw ← Data_raw^⟨0⟩
                     | U_raw ← Data_raw^⟨1⟩
                     | for j ∈ 0..n_raw
                     |   Y_raw_split ← D·(1/m)/2 − Data_raw^⟨0⟩
                     |   Data_split ← augment(Y_raw_split, U_raw)
                     |   Y_raw_upper_j ← Y_raw_split_j · (Y_raw_split_j > 0)
                     |   Y_raw_upper ← Remove_zeros(Y_raw_upper)
                     |   n ← last(Y_raw_upper)
                     | for i ∈ 0..n
                     |   Y_raw_upper_(n+1) ← 0
                     |   Y_raw_UPPER ← Y_raw_upper
                     |   n_upper ← last(Y_raw_UPPER)
                     | for i ∈ 0..n_upper
                     |   U_raw_upper_i ← U_raw_i
                     |   U_raw_upper
                     |   U_raw_upper_(n+1) ← linterp(Y_raw, U_raw, max(Y_raw)/2)
                     |   U_raw_centre ← U_raw_upper_(n+1)
                     |   U_raw_UPPER ← U_raw_upper
                     | Data_UPPER ← augment(Y_raw_UPPER, U_raw_UPPER)
```

$$
\begin{aligned}
&\text{f\_lower}(\text{Data}_{raw}) := \\
&\quad n_{raw} \leftarrow \text{last}\left(\text{Data}_{raw}^{\langle 0 \rangle}\right) \\
&\quad Y_{raw} \leftarrow \text{Data}_{raw}^{\langle 0 \rangle} \\
&\quad U_{raw} \leftarrow \text{Data}_{raw}^{\langle 1 \rangle} \\
&\quad \text{for } j \in 0..n_{raw} \\
&\quad\quad Y_{raw\_split} \leftarrow \frac{D \cdot \left(\frac{1}{m}\right)}{2} - \text{Data}_{raw}^{\langle 0 \rangle} \\
&\quad\quad \text{Data}_{split} \leftarrow \text{augment}\left(Y_{raw\_split}, U_{raw}\right) \\
&\quad\quad Y_{raw\_upper_j} \leftarrow Y_{raw\_split_j} \cdot \left(Y_{raw\_split_j} > 0\right) \\
&\quad\quad Y_{raw\_lower_j} \leftarrow Y_{raw\_split_j} \cdot \left(Y_{raw\_split_j} < 0\right) \\
&\quad\quad Y_{raw\_upper} \leftarrow \text{Remove\_zeros}\left(Y_{raw\_upper}\right) \\
&\quad\quad n \leftarrow \text{last}\left(Y_{raw\_upper}\right) \\
&\quad \text{for } i \in 0..n \\
&\quad\quad Y_{raw\_upper_{n+1}} \leftarrow 0 \\
&\quad\quad Y_{raw\_UPPER} \leftarrow Y_{raw\_upper} \\
&\quad\quad n_{upper} \leftarrow \text{last}\left(Y_{raw\_UPPER}\right) \\
&\quad \text{for } i \in 0..n_{upper} \\
&\quad\quad U_{raw\_upper_i} \leftarrow U_{raw_i} \\
&\quad\quad U_{raw\_upper} \\
&\quad\quad U_{raw\_upper_{n+1}} \leftarrow \text{linterp}\left(Y_{raw}, U_{raw}, \frac{\max\left(Y_{raw}\right)}{2}\right) \\
&\quad\quad U_{raw\_centre} \leftarrow U_{raw\_upper_{n+1}} \\
&\quad\quad Y_{raw\_lower} \leftarrow \text{Remove\_zeros}\left(Y_{raw\_lower}\right) \\
&\quad\quad n \leftarrow \text{last}\left(Y_{raw\_lower}\right) \\
&\quad \text{for } i \in 0..n \\
&\quad\quad Y_{raw\_lower_i} \leftarrow \left|Y_{raw\_lower_i}\right| \\
&\quad\quad Y_{raw\_LOWER} \leftarrow \text{reverse}\left(Y_{raw\_lower}\right) \\
&\quad \text{for } i \in n_{upper}..n_{raw} \\
&\quad\quad U_{raw\_lower_i} \leftarrow U_{raw_i} \\
&\quad\quad U_{raw\_lower} \\
&\quad\quad U_{raw\_lower\_rev} \leftarrow \text{reverse}\left(U_{raw\_lower}\right) \\
&\quad Y_{raw\_LOWER} \\
&\quad n \leftarrow \text{last}\left(Y_{raw\_LOWER}\right) \\
&\quad Y_{raw\_LOWER_{n+1}} \leftarrow 0 \\
&\quad U_{raw\_lower\_rev_{n+1}} \leftarrow U_{raw\_centre} \\
&\quad k \leftarrow \text{last}\left(Y_{raw\_LOWER}\right) \\
&\quad \text{for } i \in 0..k \\
&\quad\quad U_{raw\_LOWER_i} \leftarrow U_{raw\_lower\_rev_i} \\
&\quad\quad U_{raw\_LOWER} \\
&\quad \text{Data}_{LOWER} \leftarrow \text{augment}\left(Y_{raw\_LOWER}, U_{raw\_LOWER}\right)
\end{aligned}
$$

$$Data\_upper := f\_upper(Data_{raw})$$
$$Data\_lower := f\_lower(Data_{raw})$$
$$R_{raw\_.upper} := Data\_upper^{\langle 0 \rangle}$$
$$U_{raw\_upper} := Data\_upper^{\langle 1 \rangle}$$
$$R_{raw\_lower} := Data\_lower^{\langle 0 \rangle}$$
$$U_{raw\_lower} := Data\_lower^{\langle 1 \rangle}$$

Discretization: number of measurement points (n):

$$n := 200$$

Calculation:

$$M_{est\_upperhalve}(n) :=$$
for $j \in 0..n$
$$Y_j \leftarrow \frac{R_{max}}{n} j$$
$$U_{raw\_up_j} \leftarrow linterp\left[reverse(R_{raw\_.upper}), reverse(U_{raw\_upper}), Y_j \cdot \left(\frac{1}{m}\right)\right]$$
$$U \leftarrow reverse\left(U_{raw\_up} \cdot \frac{m}{s}\right)$$
$$R \leftarrow R_{max} - Y$$
for $i \in 1..n$
$$r_i \leftarrow \frac{R_{i-1} + R_i}{2}$$
for $i \in 1..n-1$
$$a_i \leftarrow \frac{\pi}{2} \cdot \left[(r_i)^2 - (r_{i+1})^2\right]$$
$$a_n \leftarrow \frac{\pi}{2} \cdot \left[(r_n)^2\right]$$
$$q_i \leftarrow a_i \cdot U_i$$
$$q_n \leftarrow a_n \cdot U_n$$
$$M_{est\_upper} \leftarrow \rho_w \cdot \sum q$$
$$M_{est\_upper}$$

$$M_{est\_lowerhalve}(n) :=$$

for $j \in 0..n$

$Y_j \leftarrow \frac{R_{max}}{n} j$

$U_{raw\_low_j} \leftarrow linterp\left[reverse\left(R_{raw\_lower}\right), reverse\left(U_{raw\_lower}\right), Y_j \cdot \left(\frac{1}{m}\right)\right]$

$U \leftarrow reverse\left(U_{raw\_low} \cdot \frac{m}{s}\right)$

$R \leftarrow R_{max} - Y$

for $i \in 1..n$

$r_i \leftarrow \frac{R_{i-1} + R_i}{2}$

for $i \in 1..n-1$

$a_i \leftarrow \frac{\pi}{2} \cdot \left[\left(r_i\right)^2 - \left(r_{i+1}\right)^2\right]$

$a_n \leftarrow \frac{\pi}{2} \cdot \left[\left(r_n\right)^2\right]$

$q_i \leftarrow a_i \cdot U_i$

$q_n \leftarrow a_n \cdot U_n$

$M_{est\_lower} \leftarrow \rho_w \cdot \sum q$

M_{est_lower}

A.3. Verification of algorithm using CFD results (two traverses)

Exact mass flow used in the CFD simulation:

$$M_{exact} := 14697 \frac{kg}{s}$$

Pipe diameter:

$$D := 3000mm$$

Pipe radius:

$$R_{max} := \frac{D}{2}$$

Density of water:

$$\rho_w := 999.4 \frac{kg}{m^3}$$

Input data from respective traverses

$$Data1_{raw} := \begin{bmatrix} 0 & 0 \\ 0.035 & 1.291 \\ 0.086 & 1.617 \\ 0.137 & 1.792 \\ 0.187 & 1.896 \\ 0.238 & 1.975 \\ 0.288 & 2.04 \\ 0.339 & 2.097 \\ 0.389 & 2.146 \\ 0.44 & 2.191 \\ 0.541 & 2.269 \\ 0.642 & 2.333 \\ 0.743 & 2.388 \\ 0.844 & 2.434 \\ 0.995 & 2.489 \\ 1.147 & 2.529 \\ 1.298 & 2.555 \\ 1.45 & 2.567 \\ 1.49997255 & 2.567 \\ 1.652 & 2.559 \\ 1.803 & 2.537 \\ 1.955 & 2.501 \\ 2.106 & 2.451 \\ 2.258 & 2.385 \\ 2.359 & 2.331 \\ 2.46 & 2.266 \\ 2.561 & 2.189 \\ 2.611 & 2.145 \\ 2.662 & 2.095 \\ 2.712 & 2.038 \\ 2.763 & 1.973 \\ 2.813 & 1.895 \\ 2.864 & 1.791 \\ 2.914 & 1.615 \\ 2.965 & 1.29 \\ 3 & 0 \end{bmatrix}$$

$$Data2_{raw} := \begin{bmatrix} 0 & 0 \\ 0.035 & 1.291 \\ 0.086 & 1.617 \\ 0.137 & 1.792 \\ 0.187 & 1.896 \\ 0.238 & 1.975 \\ 0.288 & 2.04 \\ 0.339 & 2.097 \\ 0.389 & 2.146 \\ 0.44 & 2.191 \\ 0.541 & 2.269 \\ 0.642 & 2.333 \\ 0.743 & 2.388 \\ 0.844 & 2.434 \\ 0.995 & 2.489 \\ 1.147 & 2.529 \\ 1.298 & 2.555 \\ 1.45 & 2.567 \\ 1.49997255 & 2.567 \\ 1.652 & 2.559 \\ 1.803 & 2.537 \\ 1.955 & 2.501 \\ 2.106 & 2.451 \\ 2.258 & 2.385 \\ 2.359 & 2.331 \\ 2.46 & 2.266 \\ 2.561 & 2.189 \\ 2.611 & 2.145 \\ 2.662 & 2.095 \\ 2.712 & 2.038 \\ 2.763 & 1.973 \\ 2.813 & 1.895 \\ 2.864 & 1.791 \\ 2.914 & 1.615 \\ 2.965 & 1.29 \\ 3 & 0 \end{bmatrix}$$

Function to remove zero entries:

$$\text{Remove\_zeros}(V) := \begin{array}{l} K \leftarrow 0 \\ \text{for } P \in V \\ \quad K_{\text{rows}(K)} \leftarrow P \text{ if } P \neq 0 \\ K \end{array}$$

Discretization: number of measurement points (n):

$$n := 10$$

Discretization of upper half:

$$M1_{\text{est\_upperhalve}}(n) := \begin{array}{l} \text{for } j \in 0..n \\ \quad Y_j \leftarrow \frac{R_{max}}{n} j \\ \quad U_{\text{raw\_up}_j} \leftarrow \text{linterp}\left[\text{reverse}\left(R1_{\text{raw\_.upper}}\right), \text{reverse}\left(U1_{\text{raw\_upper}}\right), Y_j \cdot \left(\frac{1}{m}\right)\right] \\ \quad U \leftarrow \text{reverse}\left(U_{\text{raw\_up}} \cdot \frac{m}{s}\right) \\ \quad R \leftarrow R_{max} - Y \\ \text{for } i \in 1..n \\ \quad r_i \leftarrow \frac{R_{i-1} + R_i}{2} \\ \text{for } i \in 1..n-1 \\ \quad a_i \leftarrow \frac{\pi}{4} \cdot \left[(r_i)^2 - (r_{i+1})^2\right] \\ \quad a_n \leftarrow \frac{\pi}{4} \cdot \left[(r_n)^2\right] \\ \quad q_i \leftarrow a_i \cdot U_i \\ \quad q_n \leftarrow a_n \cdot U_n \\ \quad M_{\text{est\_upper}} \leftarrow \rho_w \cdot \sum q \\ M_{\text{est\_upper}} \end{array}$$

$M1_{est\_lowerhalve}(n) :=$ | for $j \in 0..n$
| $Y_j \leftarrow \frac{R_{max}}{n} j$
| $U_{raw\_low_j} \leftarrow linterp\left[reverse\left(R1_{raw\_lower}\right), reverse\left(U1_{raw\_lower}\right), Y_j \cdot \left(\frac{1}{m}\right)\right]$
| $U \leftarrow reverse\left(U_{raw\_low} \cdot \frac{m}{s}\right)$
| $R \leftarrow R_{max} - Y$
for $i \in 1..n$
$r_i \leftarrow \frac{R_{i-1} + R_i}{2}$
for $i \in 1..n-1$
| $a_i \leftarrow \frac{\pi}{4} \cdot \left[\left(r_i\right)^2 - \left(r_{i+1}\right)^2\right]$
| $a_n \leftarrow \frac{\pi}{4} \cdot \left[\left(r_n\right)^2\right]$
| $q_i \leftarrow a_i \cdot U_i$
| $q_n \leftarrow a_n \cdot U_n$
| $M_{est\_lower} \leftarrow \rho_w \cdot \sum q$
M_{est_lower}

In this case, the areas are divided by four since the approximation is based on one quarter. Therefore instead of dividing the areas by four, a more generic approach is to account for the total number of traverses as shown below

$$a_i = \frac{\pi}{2 \cdot T}\left(\left(r_i^2\right) - \left(r_{i+1}^2\right)\right)$$

$$a_n = \frac{\pi}{2 \cdot T}\left(r_n^2\right)$$

where T is the number of traverses.

$$
\begin{aligned}
&M2_{est\_upperhalve}(n) := \left|\begin{array}{l}
\text{for } j \in 0..n \\
\quad \left|\begin{array}{l}
Y_j \leftarrow \frac{R_{max}}{n} j \\
U_{raw\_up_j} \leftarrow \text{linterp}\left[\text{reverse}\left(R2_{raw\_.upper}\right), \text{reverse}\left(U2_{raw\_upper}\right), Y_j \cdot \left(\frac{1}{m}\right)\right] \\
U \leftarrow \text{reverse}\left(U_{raw\_up} \cdot \frac{m}{s}\right) \\
R \leftarrow R_{max} - Y
\end{array}\right. \\
\text{for } i \in 1..n \\
\quad r_i \leftarrow \frac{R_{i-1} + R_i}{2} \\
\text{for } i \in 1..n-1 \\
\quad \left|\begin{array}{l}
a_i \leftarrow \frac{\pi}{4} \cdot \left[\left(r_i\right)^2 - \left(r_{i+1}\right)^2\right] \\
a_n \leftarrow \frac{\pi}{4} \cdot \left[\left(r_n\right)^2\right] \\
q_i \leftarrow a_i \cdot U_i \\
q_n \leftarrow a_n \cdot U_n \\
M_{est\_upper} \leftarrow \rho_w \cdot \sum q
\end{array}\right. \\
M_{est\_upper}
\end{array}\right.
\end{aligned}
$$

In this case the areas are also divided by four since the approximation is based on one quarter. Similarly,

$$a_i = \frac{\pi}{2 \cdot T}\left(\left(r_i^2\right) - \left(r_{i+1}^2\right)\right)$$

$$a_n = \frac{\pi}{2 \cdot T}\left(r_n^2\right)$$

where T is the number of traverses.

$$M2_{est\_lowerhalve}(n) :=$$

for $j \in 0..n$

$Y_j \leftarrow \frac{R_{max}}{n} j$

$U_{raw\_low_j} \leftarrow linterp\left[reverse\left(R2_{raw\_lower}\right), reverse\left(U2_{raw\_lower}\right), Y_j \cdot \left(\frac{1}{m}\right)\right]$

$U \leftarrow reverse\left(U_{raw\_low} \cdot \frac{m}{s}\right)$

$R \leftarrow R_{max} - Y$

for $i \in 1..n$

$r_i \leftarrow \frac{R_{i-1} + R_i}{2}$

for $i \in 1..n-1$

$a_i \leftarrow \frac{\pi}{4} \cdot \left[\left(r_i\right)^2 - \left(r_{i+1}\right)^2\right]$

$a_n \leftarrow \frac{\pi}{4} \cdot \left[\left(r_n\right)^2\right]$

$q_i \leftarrow a_i \cdot U_i$

$q_n \leftarrow a_n \cdot U_n$

$M_{est\_lower} \leftarrow \rho_w \cdot \sum q$

M_{est_lower}

A.4. Complete chord-wise algorithm to estimate the mass flow rate - verification (CAD)

Traverses along the chord of the duct:

$Data_{a\_raw} :=$

0	2.2671821
0.022295892	2.267906526
0.044591785	2.27079483
0.066887677	2.275841316
0.089183569	2.283034482
0.113826838	2.289602957
0.13696171	2.29689333
0.160096582	2.30923994
0.183231453	2.325969934
0.206366325	2.346743833
0.229501197	2.371221123
0.254733377	2.376552848
0.279965558	2.385087216
0.306049557	2.392918926
0.332133556	2.404159252
0.345175556	2.411040781
0.383733676	2.410086184
0.422291795	2.411682879
0.460849915	2.415656127
0.593805522	2.391683534
0.692820323	2.37871002
0.71940219	2.372782896
0.825729657	2.350690182
0.852311524	2.345826263
0.923653891	2.313077991
1.000787883	2.265103235
1.026499213	2.250138781
1.077921874	2.224808594
1.103633205	2.210639534
1.129344536	2.194761214
1.155055866	2.177200288
1.207533162	2.119748926
1.233771809	2.089549253
1.270756854	2.04275024
1.293719357	2.007355482
1.31668186	1.974777609
1.339644364	1.944974929
1.362606867	1.917900723
1.385640646	1.89343192

$Data_{b\_raw} :=$

0	2.2671821
0.024644233	2.275324135
0.049288467	2.285587212
0.0739327	2.297942912
0.123621167	2.326565445
0.1486654	2.346976732
0.173709633	2.37343151
0.198753867	2.405730413
0.213064857	2.408643058
0.227375848	2.412573348
0.241686838	2.417516321
0.255997829	2.423465779
0.270308819	2.430414332
0.28461981	2.438353439
0.2989308	2.447273458
0.327552781	2.4509357
0.356174762	2.456452785
0.384796743	2.463812252
0.399107734	2.46817789
0.427736305	2.466193298
0.456364876	2.464921657
0.484993448	2.464364072
0.513622019	2.465470579
0.542250591	2.468234048
0.570879162	2.471700502
0.599507734	2.475866988
0.685393448	2.477883341
0.771279162	2.481448836
0.799907734	2.482980517
0.828615389	2.48167197
0.914461556	2.47873771
1.000307723	2.477274138
1.028936293	2.473329245
1.057564863	2.470074707
1.086193433	2.467513255
1.114822003	2.466579485
1.143450573	2.467276738
1.172079142	2.468672841
1.200707712	2.470766607
1.229342876	2.46248893
1.257978039	2.456041579
1.286613203	2.451438998
1.300930784	2.449832908
1.315248366	2.440314474
1.329565948	2.431772815
1.343883529	2.424218256
1.358201111	2.417660051
1.372518693	2.412106326
1.386836274	2.407564033
1.401153856	2.404038905
1.426209624	2.368683556
1.451265392	2.339185352
1.47632116	2.31576813
1.501376928	2.298617747
1.52599438	2.282344862
1.550611832	2.268173884
1.575229284	2.25614442
1.6	2.246236408

$Data_{c\_raw} :=$

0	2.2671821
0.025399605	2.280662818
0.05079921	2.29500963
0.076198815	2.310184188
0.101598419	2.326148684
0.113826838	2.332293839
0.13696171	2.339456886
0.160096582	2.349194098
0.183231453	2.361364692
0.206366325	2.37582582
0.229501197	2.392434027
0.242077039	2.391081595
0.254652881	2.390420973
0.267228724	2.390495631
0.279804566	2.391349719
0.305579195	2.394159869
0.318777982	2.396165402
0.331976769	2.39907082
0.345175556	2.402901843
0.370880969	2.397322029
0.396586382	2.39380389
0.422291795	2.392605372
0.435144502	2.392963712
0.447997208	2.394010241
0.460849915	2.395783994
0.487486724	2.386970285
0.514123533	2.37924571
0.594033959	2.370138915
0.620670768	2.363747114
0.647307577	2.356691863
0.673944385	2.348967983
0.692820323	2.339810796
0.769764846	2.28772388
0.898005717	2.189441861
0.923653891	2.17045538
1.098171578	2.1037787
1.328083789	2.101150788
1.356747257	2.106910894
1.385640646	2.117219302

Include angle between the traverses in degrees:

$\alpha := 30^{\circ}$

Mass density of water:

$$\rho_w := 998.9 \frac{kg}{m^3}$$

Exact total mass per unit time (s):

$$M_{exact} := 4415 \frac{kg}{s}$$

Pipe diameter:

$$D := 1600mm$$

Pipe radius:

$$R_{max} := \frac{D}{2}$$

Angle between traverse a and centre traverse b in degrees:

$$\beta_a := 30°$$

Angle between traverse c and centre traverse b in degrees:

$$\beta_c := 30°$$

Measurement location for the respective traverse:

$$a_{raw} := Data_{a\_raw}^{\langle 0 \rangle} m$$

$$b_{raw} := Data_{b\_raw}^{\langle 0 \rangle} m$$

$$c_{raw} := Data_{c\_raw}^{\langle 0 \rangle} m$$

Corresponding local flow velocity for the respective traverse:

$$Ua_{raw} := Data_{a\_raw}^{\langle 1 \rangle}$$

$$Ub_{raw} := Data_{b\_raw}^{\langle 1 \rangle}$$

$$Uc_{raw} := Data_{c\_raw}^{\langle 1 \rangle}$$

Number of measurement point along respective traverse:

$$n_a := last(a_{raw})$$

$$n_b := last(b_{raw})$$

$$n_c := last(c_{raw})$$

Maximum number of measurement points on either traverse:

$$n := max(n_a, n_b, n_c)$$

$M_{est\_tess}(n) :=$

for $i \in 1..n$

$a_i \leftarrow \frac{\max(a_{raw})}{n} i$

$Ua \leftarrow linterp\left(\frac{a_{raw}}{m}, Ua_{raw} \cdot \frac{m}{s}, \frac{a}{m}\right)$

$c_i \leftarrow \frac{\max(c_{raw})}{n} i$

$Uc \leftarrow linterp\left(\frac{c_{raw}}{m}, Uc_{raw} \cdot \frac{m}{s}, \frac{c}{m}\right)$

for $i \in 1..n+1$

$b_i \leftarrow \frac{\max(b_{raw})}{n+1} i$

$Ub \leftarrow linterp\left(\frac{b_{raw}}{m}, Ub_{raw} \cdot \frac{m}{s}, \frac{b}{m}\right)$

$n_a \leftarrow last(a)$

$n_b \leftarrow last(b)$

$n_c \leftarrow last(c)$

Discretized measurement points along respective traverse:

Corresponding local flow measurement:

$Xa_0 \leftarrow a_0$

$Xb_0 \leftarrow b_0$

$Xc_0 \leftarrow c_0$

Initial X coordinates for the respective traverses:

$Ya_0 \leftarrow a_0$

$Yb_0 \leftarrow b_0$

$Yc_0 \leftarrow c_0$

Initial Y coordinates for the respective traverses:

for $i \in 1..n_b$

$Xb_i \leftarrow b_i$

$Yb_i \leftarrow 0$

Range variable to compute the vertice coordinates along the respective traverse:

for $i \in 1..n$

$Xa_i \leftarrow a_i \cdot \cos(-\alpha)$

$Ya_i \leftarrow a_i \cdot \sin(-\alpha)$

$Xc_i \leftarrow c_i \cdot \cos(\alpha)$

$Yc_i \leftarrow c_i \cdot \sin(\alpha)$

Range variable to compute the vertice

Coordinates along the respective traverse:

Individual tessellated areas along the respective traverse:

$$Aba_i \leftarrow \frac{1}{2}\left\|\frac{1}{m}\cdot\begin{pmatrix} Xb_{i-1} & Yb_{i-1} & 1m \\ Xb_i & Yb_i & 1m \\ Xa_i & Ya_i & 1m \end{pmatrix}\right\| m^2$$

$$Abc_i \leftarrow \frac{1}{2}\left\|\frac{1}{m}\cdot\begin{pmatrix} Xb_{i-1} & Yb_{i-1} & 1m \\ Xb_i & Yb_i & 1m \\ Xc_i & Yc_i & 1m \end{pmatrix}\right\| m^2$$

Average local velocities based on the velocities at the vertices:

$$u_{ba_i} \leftarrow \frac{Ub_{i-1} + Ub_i + Ua_i}{3}$$

$$u_{ba_n} \leftarrow Ub_{n-1}$$

$$u_{bc_i} \leftarrow \frac{Ub_{i-1} + Ub_i + Uc_i}{3}$$

$$u_{bc_n} \leftarrow Uc_{n-1}$$

$$Qba_{est_i} \leftarrow Aba_i \cdot u_{ba_i}$$

$$Qbc_{est_i} \leftarrow Abc_i \cdot u_{bc_i}$$

for $i \in 1..n-1$

$$Aab_i \leftarrow \frac{1}{2}\left\|\frac{1}{m}\cdot\begin{pmatrix} Xa_i & Ya_i & 1m \\ Xa_{i+1} & Ya_{i+1} & 1m \\ Xb_i & Yb_i & 1m \end{pmatrix}\right\| m^2$$

$$Acb_i \leftarrow \frac{1}{2}\left\|\frac{1}{m}\cdot\begin{pmatrix} Xc_i & Yc_i & 1m \\ Xc_{i+1} & Yc_{i+1} & 1m \\ Xb_i & Yb_i & 1m \end{pmatrix}\right\| m^2$$

$$u_{ab_i} \leftarrow \frac{Ua_i + Ua_{i+1} + Ub_i}{3}$$

$$u_{ab_{n-1}} \leftarrow \frac{Ua_{n-1} + Ub_{n-1}}{2}$$

$$u_{cb_i} \leftarrow \frac{Uc_i + Uc_{i+1} + Ub_i}{3}$$

$$u_{cb_{n-1}} \leftarrow \frac{Uc_{n-1} + Ub_{n-1}}{2}$$

$$Qab_{est_i} \leftarrow Aab_i \cdot u_{ab_i}$$

$$Qcb_{est_i} \leftarrow Acb_i \cdot u_{cb_i}$$

Total volumetric flow estimate through the individual tessellated areas:

$$Q_{est} \leftarrow \sum Qba_{est} + \sum Qab_{est} + \sum Qbc_{est} + \sum Qcb_{est}$$

$$M_{est} \leftarrow \rho_w \cdot Q_{est}$$

Segments along traverses

Number of measurement points:

$n_{initial} := n$

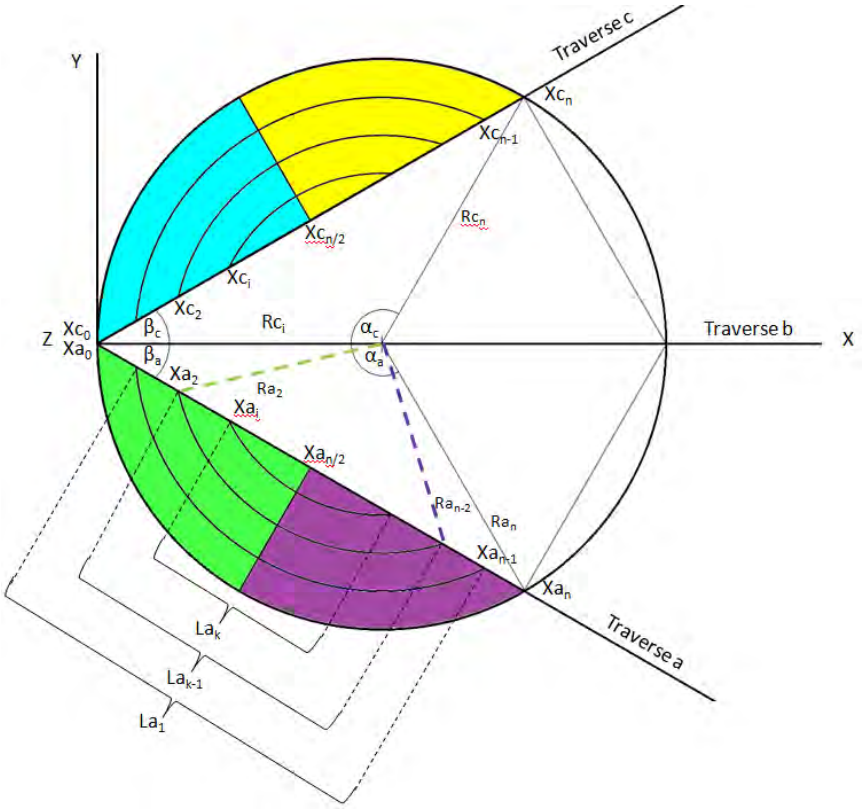

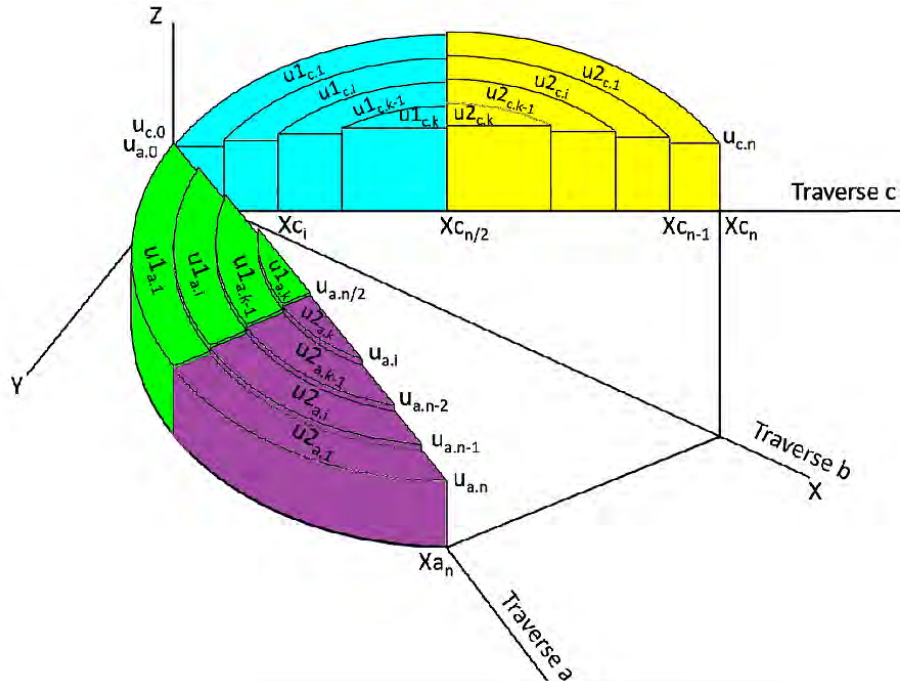

Mass flow of the segment along traverse a:

$M_{seg\_a}(n_{initial}) :=$

$n_a \leftarrow n_{initial}$

Number of measurement points:

$n_c \leftarrow n_{initial}$

$Ua_{raw} \leftarrow Data_{a\_raw}^{\langle 1 \rangle}$

Raw local velocity location along the respective traverse:

$a_{raw} \leftarrow Data_{a\_raw}^{\langle 0 \rangle}$

Raw measurement location along the respective traverse:

for $i \in 0..n_a$

Range variable for discretization:

$Xa_{gen_i} \leftarrow \frac{max(a_{raw})}{n_a} i$

Discretized measurement location:

$u_{a_i} \leftarrow linterp(a_{raw}, Ua_{raw}, Xa_{gen_i})$

New corresponding interpolated local velocity along the respective traverse

$Data_{a\_gen} \leftarrow augment(Xa_{gen}, u_a)$

$a_{mid} \leftarrow \frac{max(a_{raw})}{2}$

Centre measurement location along the respective traverse:

$Ua_{mid} \leftarrow linterp(a_{raw}, Ua_{raw}, a_{mid})$

Corresponding centre flow velocity along the respective traverse:

$a_{centre} \leftarrow (a_{mid} \quad Ua_{mid})$

Centre point coordinates:

$Data_{a\_centre} \leftarrow stack(Data_{a\_gen}, a_{centre})$

Centre point coordinates stacked into the raw measurement data:

$Data_{a\_new} \leftarrow csort(Data_{a\_centre}, 0)$

New measurement data with forced centre coordinates:

$Xa \leftarrow Data_{a\_new}^{\langle 0 \rangle} m$

$Ua \leftarrow Data_{a\_new}^{\langle 1 \rangle} \frac{m}{s}$

$n \leftarrow \text{last}(Xa)$

$k \leftarrow \text{mod}(n_a, 2)$

Modulus of n to differentiate between odd and even number of measurement points:

for $i \in 1..n$

$xa_i \leftarrow \frac{Xa_{i-1} + Xa_i}{2}$

Midpoints of the discretized measurement locations

$Ra_i \leftarrow \sqrt{(xa_i)^2 + \left(\frac{D}{2}\right)^2 - 2xa_i \cdot \frac{D}{2} \cdot \cos(\beta_a)}$

along the respective traverse:
Radius of the sector from which the area of its segment is calculated:

for $i \in 1..\left(\frac{n-1+k}{2}\right)$

$La_i \leftarrow \left|xa_{n-i+1} - xa_i\right|$

Length of each discretized segment:

$\alpha_{a_i} \leftarrow \text{acos}\left[\frac{(Ra_i)^2 + (Ra_i)^2 - (La_i)^2}{2 \cdot Ra_i \cdot Ra_i}\right]$

Angle of the sector from which the area of the discretized segments is calculated:

$Seg_{a_i} \leftarrow \frac{1}{2}(Ra_i)^2\left(\alpha_{a_i} - \sin(\alpha_{a_i})\right)$

Area of the discretized segments:

for $i \in 1..\left(\frac{n-1+k}{2}\right) - 1$

$Anu\_seg_{a_i} \leftarrow \frac{1}{2}\left(Seg_{a_i} - Seg_{a_{i+1}}\right)$

Area of annular segments up to the midpoint of the respective traverse:

$Anu\_seg_{a\left(\frac{n-1+k}{2}\right)} \leftarrow \frac{1}{2}\left[Seg_{a\left(\frac{n-1+k}{2}\right)}\right]$

Area of discretized segments:

$Ua1_i \leftarrow Ua_i$

Local flow velocities along the first half of the respective traverse:

$q_{a1_i} \leftarrow Anu\_seg_{a_i} \cdot Ua1_i$

$Q_{a1} \leftarrow \sum q_{a1}$

Sum of the volumetric flow along the first half of the respective traverse:

for $j \in \left[\left(\frac{n+1-k}{2}\right)..n\right]$

$Ua2_j \leftarrow Ua_j$

$Ua2 \leftarrow \text{Remove\_zeros}(Ua2)$

$q_{a2_i} \leftarrow Anu\_seg_{a_i} \cdot Ua2_i$

$Q_{a2} \leftarrow \sum q_{a2}$

Total flow rate through the area of annular segments along the respective traverse:

$M_{est} \leftarrow \rho_w \cdot (Q_{a1} + Q_{a2})$

Mass flow of the segment along traverse c:

Total flow rate through the area of annular segments along the traverse is calculated similar to *Mass flow of the segment along traverse a* .

Thus the total estimated mass flow rate and measurement error, using the chord-wise algorithm, is obtained from the following function. It generates an array of percentage error for given number of measurement points (n):

$$
\begin{aligned}
&f\left(n_{initial}\right) := \left|\begin{array}{l}
\text{for } j \in 0..n_{initial} \\
\quad \left|\begin{array}{l}
M_{est\_tess}(n) \\
M_{seg\_a}\left(n_{initial}\right) \\
M_{seg\_c}\left(n_{initial}\right) \\
M_{est} \leftarrow M_{est\_tess}(n) + M_{seg\_a}\left(n_{initial}\right) + M_{seg\_c}\left(n_{initial}\right)
\end{array}\right. \\
\dfrac{M_{est} - M_{exact}}{M_{exact}} \cdot 100
\end{array}\right.
\end{aligned}
$$

Appendix B. Accuracy Prediction Results (CFD Simulations)

The following graphs represent the predicted measurement accuracy as a function of the number of measurement points (vice versa) for various traversing paths at 0, 2.2D, 3.3D, 6.6D, 11.1D and 20D after a bend. The Reynolds number=$10^{5.5}$ and $\varepsilon/D=1.3\times10^{-3}$.

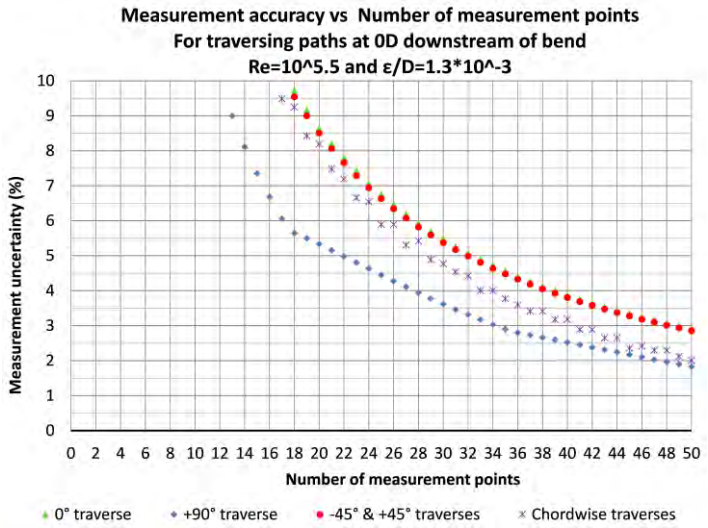

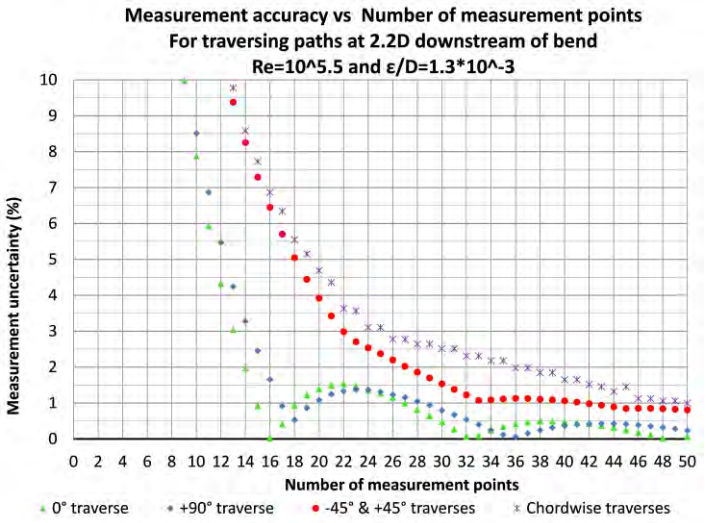

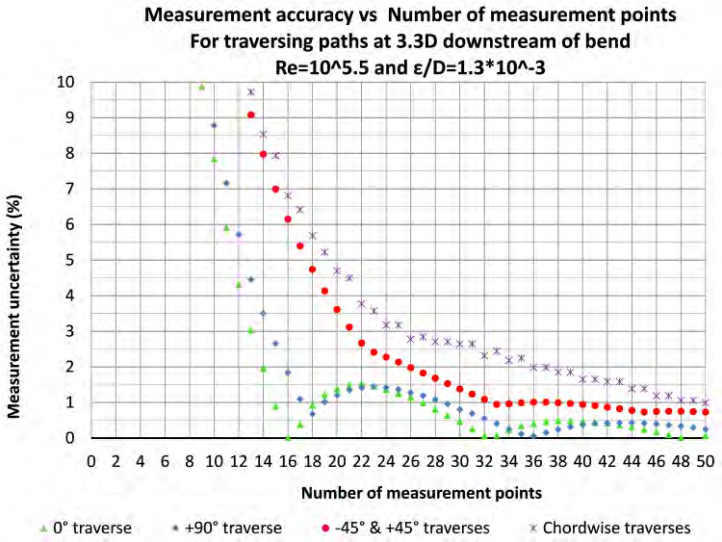
Measurement accuracy vs Number of measurement points
For traversing paths at 3.3D downstream of bend
Re=10^5.5 and ε/D=1.3*10^-3
Measurement uncertainty (%)
Number of measurement points
0° traverse
+90° traverse
-45° & +45° traverses
Chordwise traverses

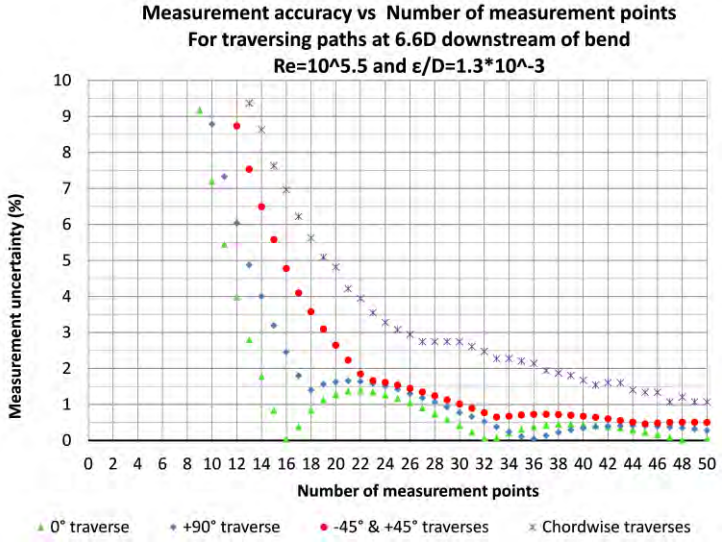
Measurement accuracy vs Number of measurement points
For traversing paths at 6.6D downstream of bend
Re=10^5.5 and ε/D=1.3*10^-3
Measurement uncertainty (%)
Number of measurement points
0° traverse
+90° traverse
-45° & +45° traverses
Chordwise traverses

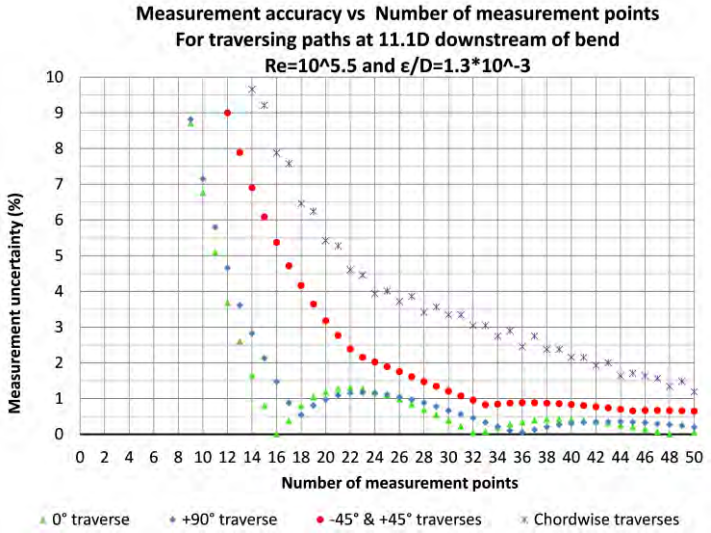
Measurement accuracy vs Number of measurement points
For traversing paths at 11.1D downstream of bend
Re=10^5.5 and ε/D=1.3*10^-3
Measurement uncertainty (%)
Number of measurement points
0° traverse
+90° traverse
-45° & +45° traverses
Chordwise traverses

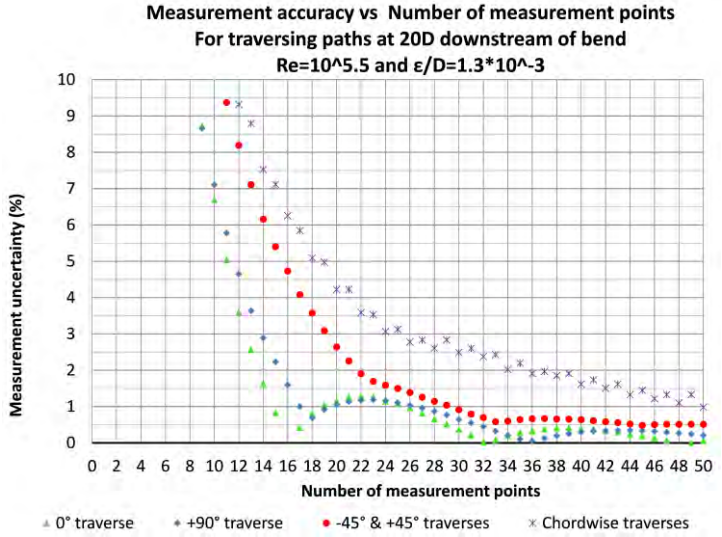
Measurement accuracy vs Number of measurement points
For traversing paths at 20D downstream of bend
Re=10^5.5 and ε/D=1.3*10^-3
Measurement uncertainty (%)
Number of measurement points
0° traverse
+90° traverse
-45° & +45° traverses
Chordwise traverses

The following graphs represent the predicted measurement accuracy as a function of the number of measurement points (vice versa) for various traversing paths at 0, 2.2D, 3.3D, 6.6D, 11.1D and 20D after a bend. The Reynolds number=10^6 and $\varepsilon/D=1.3\times10^{-3}$.

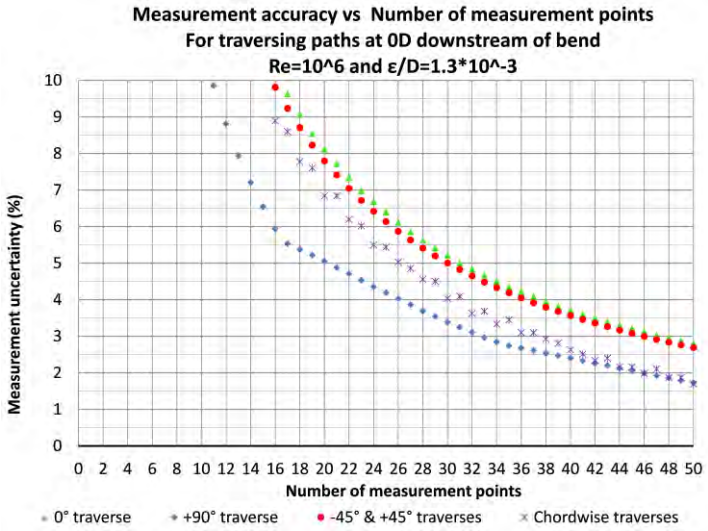

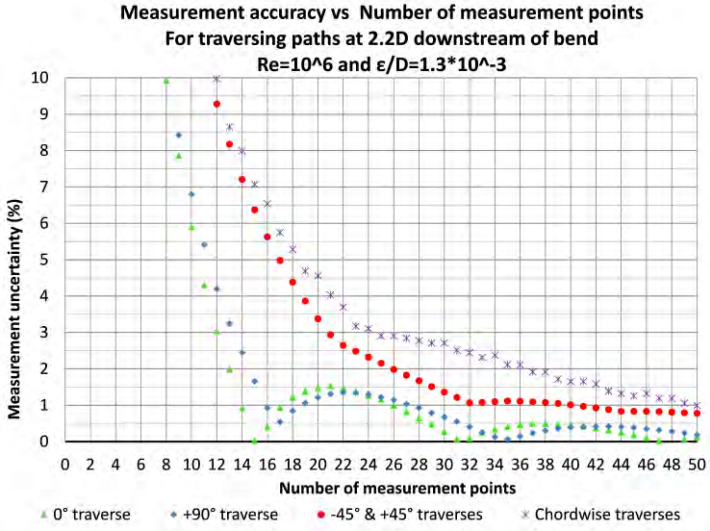

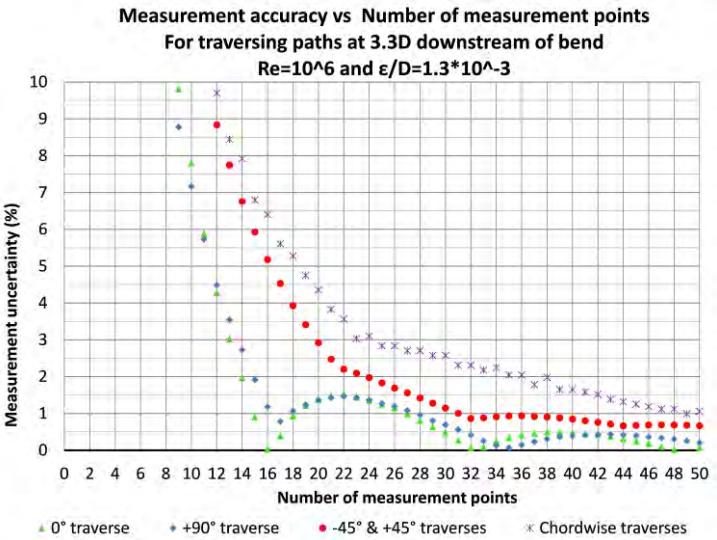
Measurement accuracy vs Number of measurement points
For traversing paths at 3.3D downstream of bend
Re=10^6 and ε/D=1.3*10^-3
Measurement uncertainty (%)
Number of measurement points
0° traverse
+90° traverse
-45° & +45° traverses
Chordwise traverses

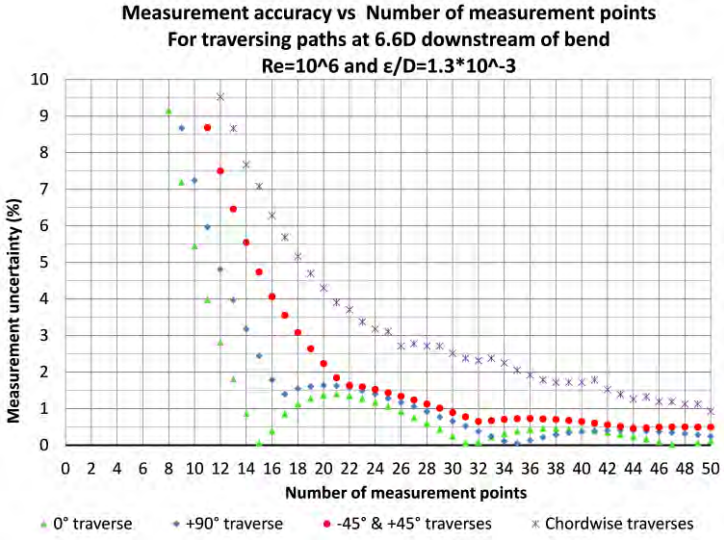
Measurement accuracy vs Number of measurement points
For traversing paths at 6.6D downstream of bend
Re=10^6 and ε/D=1.3*10^-3
Measurement uncertainty (%)
Number of measurement points
0° traverse
+90° traverse
-45° & +45° traverses
Chordwise traverses

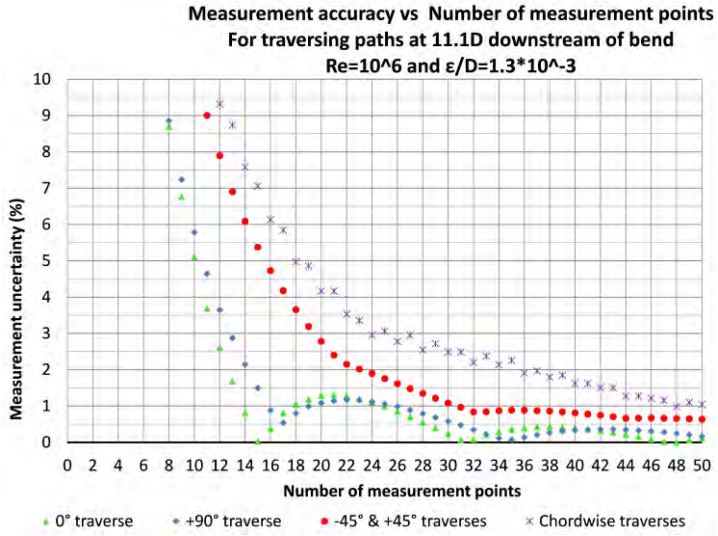
Measurement accuracy vs Number of measurement points
For traversing paths at 11.1D downstream of bend
Re=10^6 and ε/D=1.3*10^-3
Measurement uncertainty (%)
Number of measurement points
0° traverse
+90° traverse
-45° & +45° traverses
Chordwise traverses

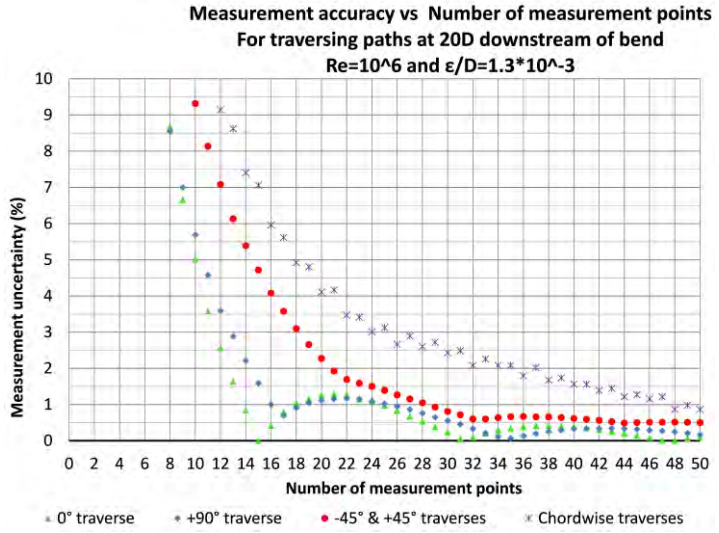
Measurement accuracy vs Number of measurement points
For traversing paths at 20D downstream of bend
Re=10^6 and ε/D=1.3*10^-3
Measurement uncertainty (%)
Number of measurement points
0° traverse
+90° traverse
-45° & +45° traverses
Chordwise traverses

The following graphs represent the predicted measurement accuracy as a function of the number of measurement points (vice versa) for various traversing paths at 0, 2.2D, 3.3D, 6.6D, 11.1D and 20D after a bend. The Reynolds number=$10^{6.7}$ and $\varepsilon/D=1.3\times10^{-3}$.

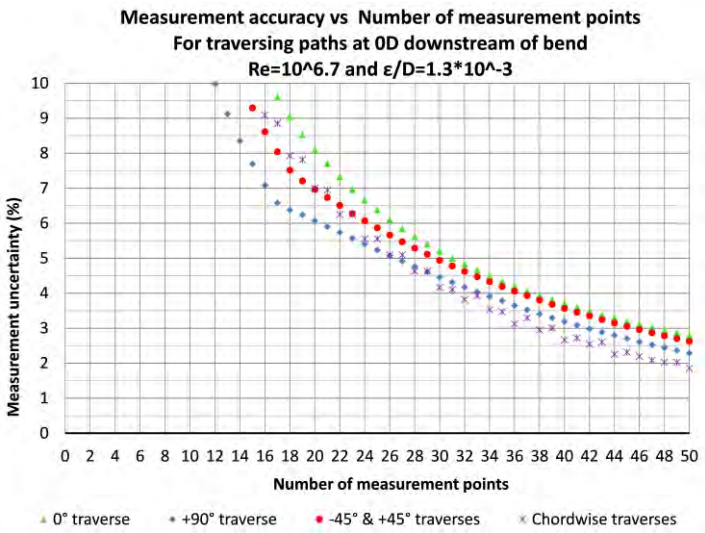

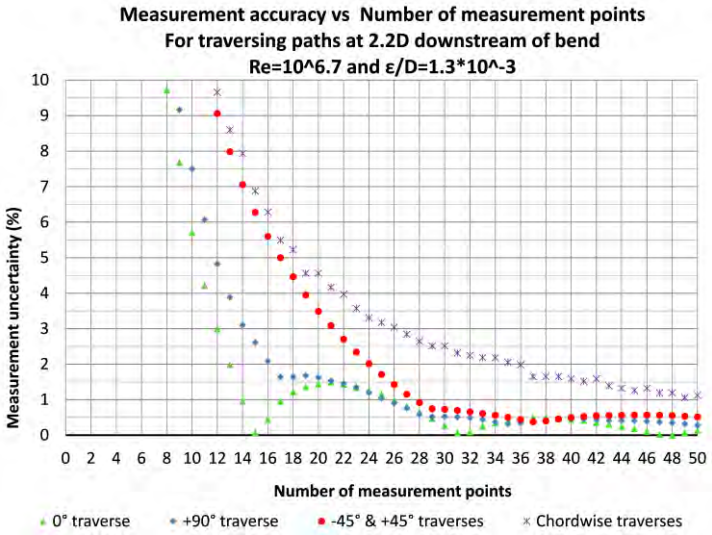

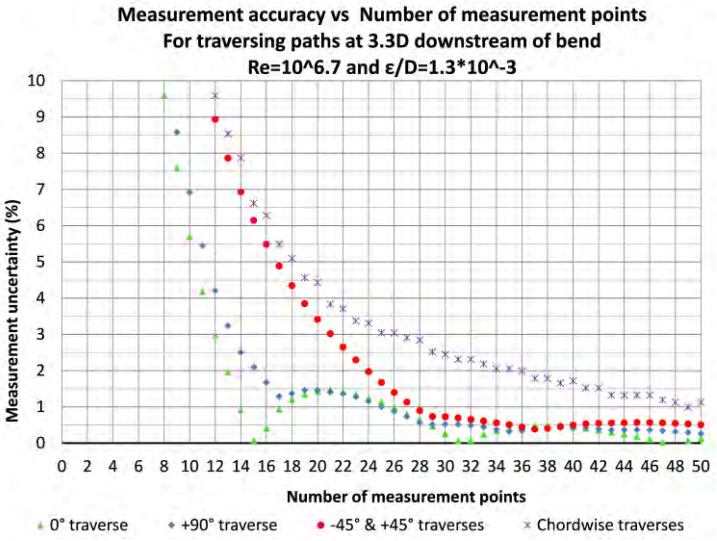
Measurement accuracy vs Number of measurement points
For traversing paths at 3.3D downstream of bend
Re=10^6.7 and ε/D=1.3*10^-3
Measurement uncertainty (%)
Number of measurement points
0° traverse
+90° traverse
-45° & +45° traverses
Chordwise traverses

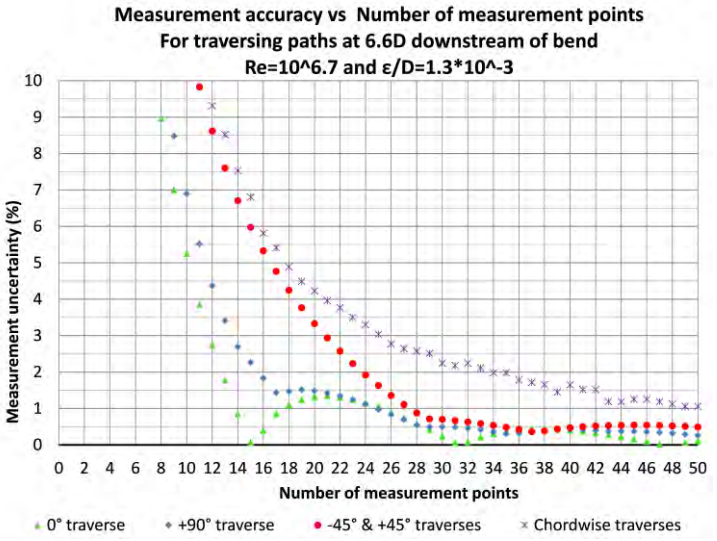
Measurement accuracy vs Number of measurement points
For traversing paths at 6.6D downstream of bend
Re=10^6.7 and ε/D=1.3*10^-3
Measurement uncertainty (%)
Number of measurement points
0° traverse
+90° traverse
-45° & +45° traverses
Chordwise traverses

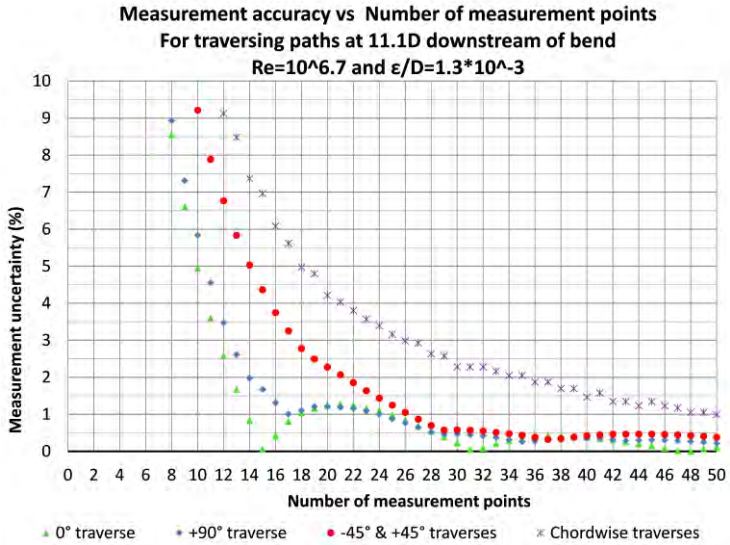
Measurement accuracy vs Number of measurement points
For traversing paths at 11.1D downstream of bend
Re=10^6.7 and ε/D=1.3*10^-3
Measurement uncertainty (%)
Number of measurement points
0° traverse
+90° traverse
-45° & +45° traverses
Chordwise traverses

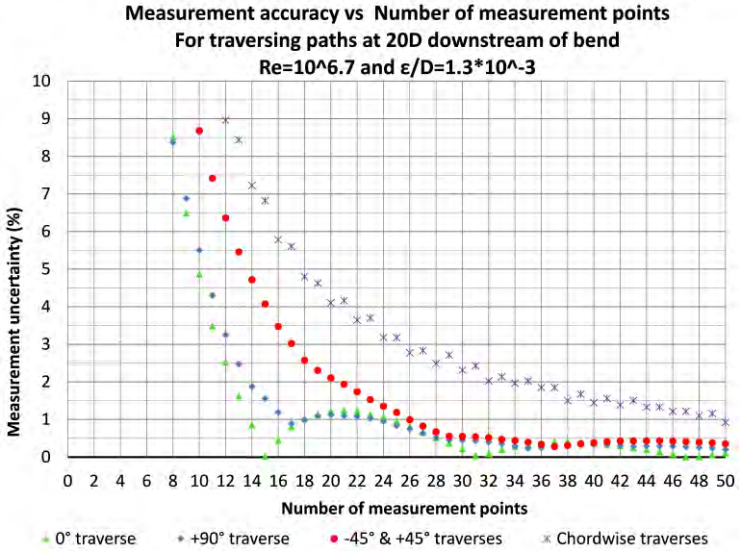
Measurement accuracy vs Number of measurement points
For traversing paths at 20D downstream of bend
Re=10^6.7 and ε/D=1.3*10^-3
Measurement uncertainty (%)
Number of measurement points
0° traverse
+90° traverse
-45° & +45° traverses
Chordwise traverses

The following graphs represent the predicted measurement accuracy as a function of the number of measurement points (vice versa) for various traversing paths at 0, 2.2D, 3.3D, 6.6D, 11.1D and 20D after a bend. The Reynolds number=10^7 and $\varepsilon/D=1.3\times10^{-3}$.

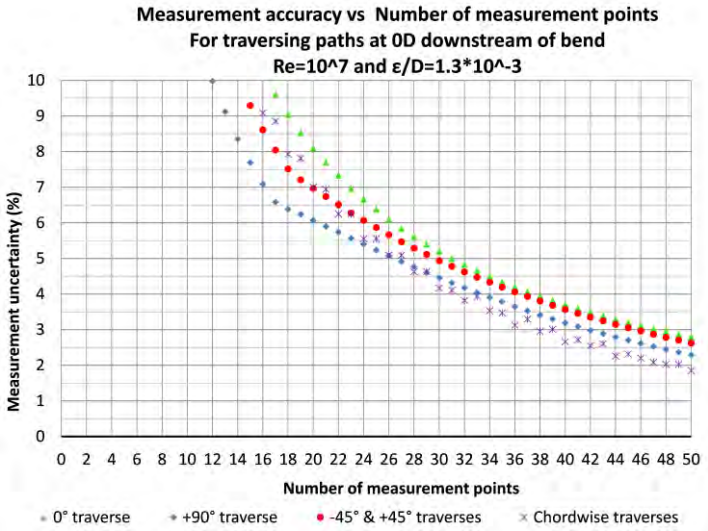

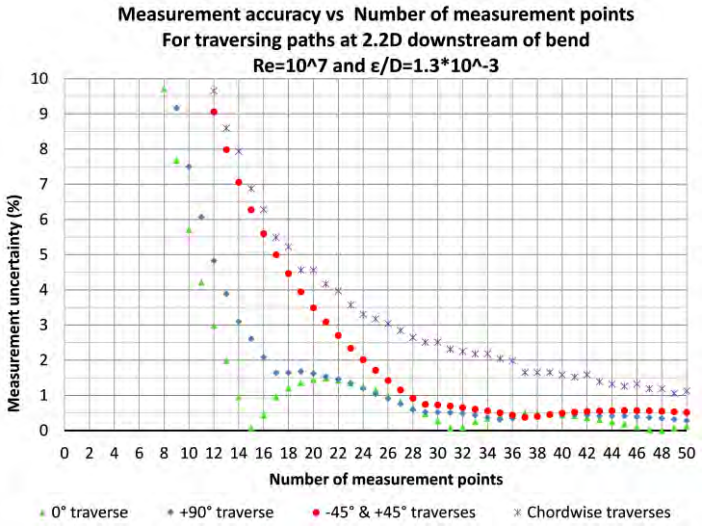

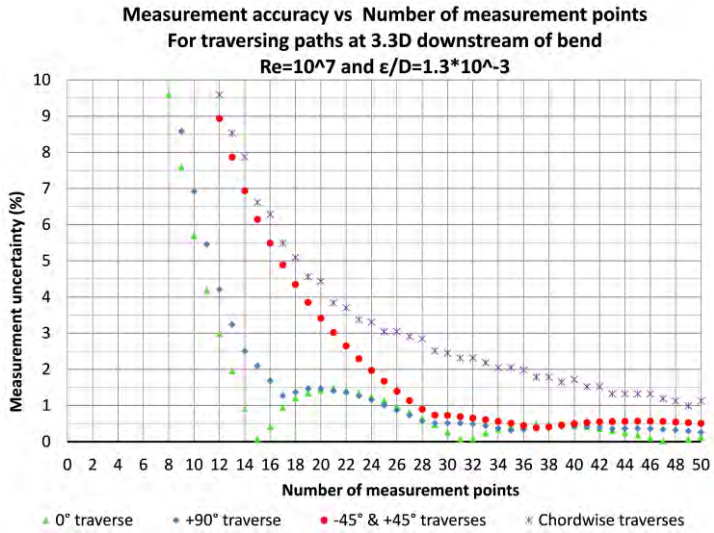
Measurement accuracy vs Number of measurement points
For traversing paths at 3.3D downstream of bend
Re=10^7 and ε/D=1.3*10^-3
Measurement uncertainty (%)
Number of measurement points
0° traverse
+90° traverse
-45° & +45° traverses
Chordwise traverses

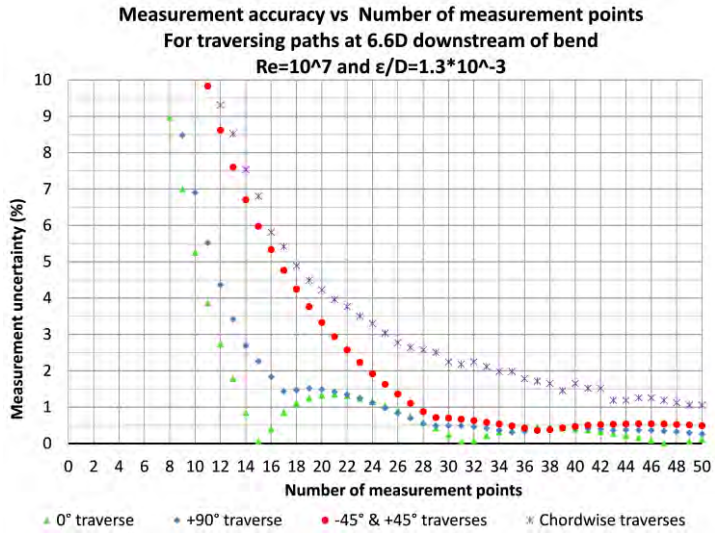
Measurement accuracy vs Number of measurement points
For traversing paths at 6.6D downstream of bend
Re=10^7 and ε/D=1.3*10^-3
Measurement uncertainty (%)
Number of measurement points
0° traverse
+90° traverse
-45° & +45° traverses
Chordwise traverses

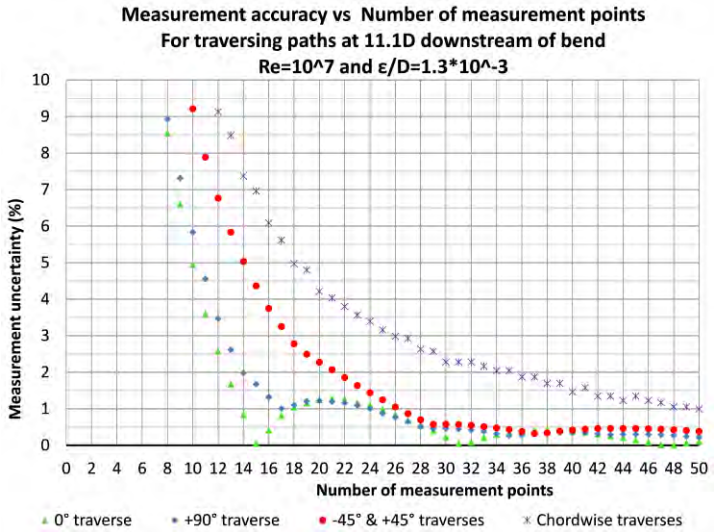
Measurement accuracy vs Number of measurement points
For traversing paths at 11.1D downstream of bend
Re=10^7 and ε/D=1.3*10^-3
Measurement uncertainty (%)
Number of measurement points
0° traverse
+90° traverse
-45° & +45° traverses
Chordwise traverses

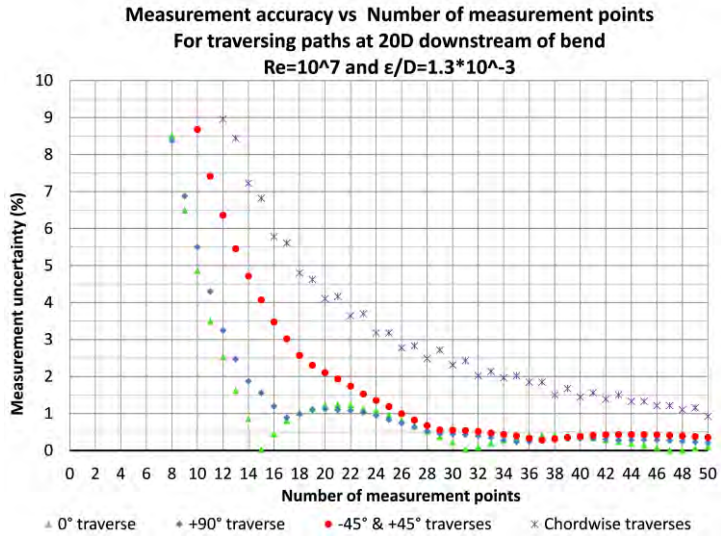
Measurement accuracy vs Number of measurement points
For traversing paths at 20D downstream of bend
Re=10^7 and ε/D=1.3*10^-3
Measurement uncertainty (%)
Number of measurement points
0° traverse
+90° traverse
-45° & +45° traverses
Chordwise traverses

Appendix C. Static Errors

The following graphs represent the static error associated with the algorithm for various traversing paths at different measurement locations downstream a bend.

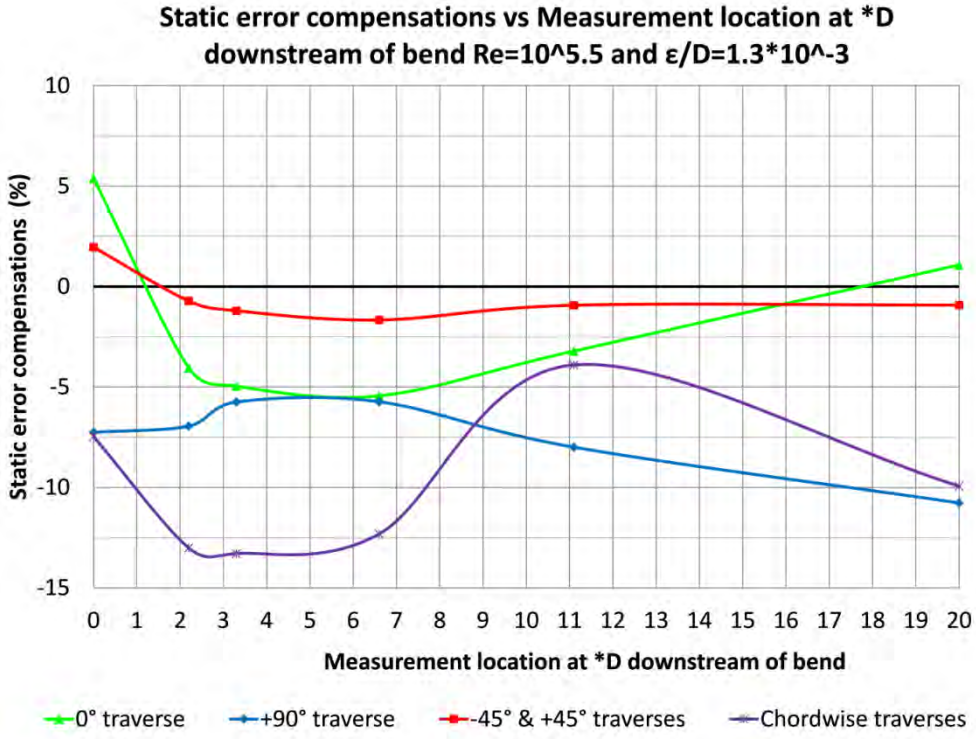

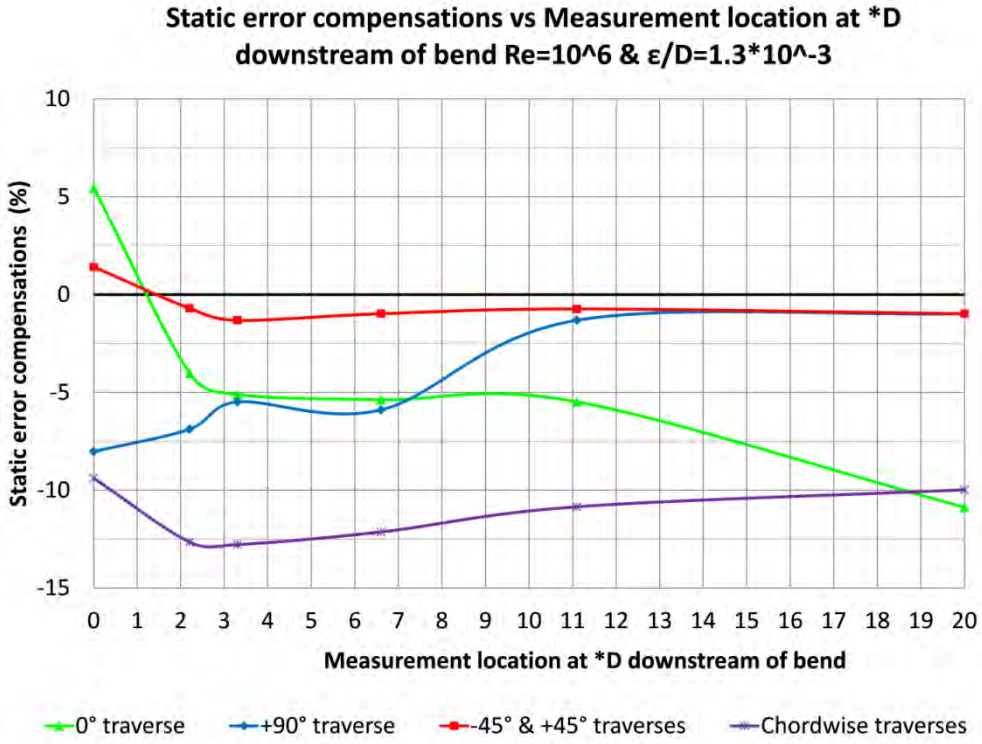

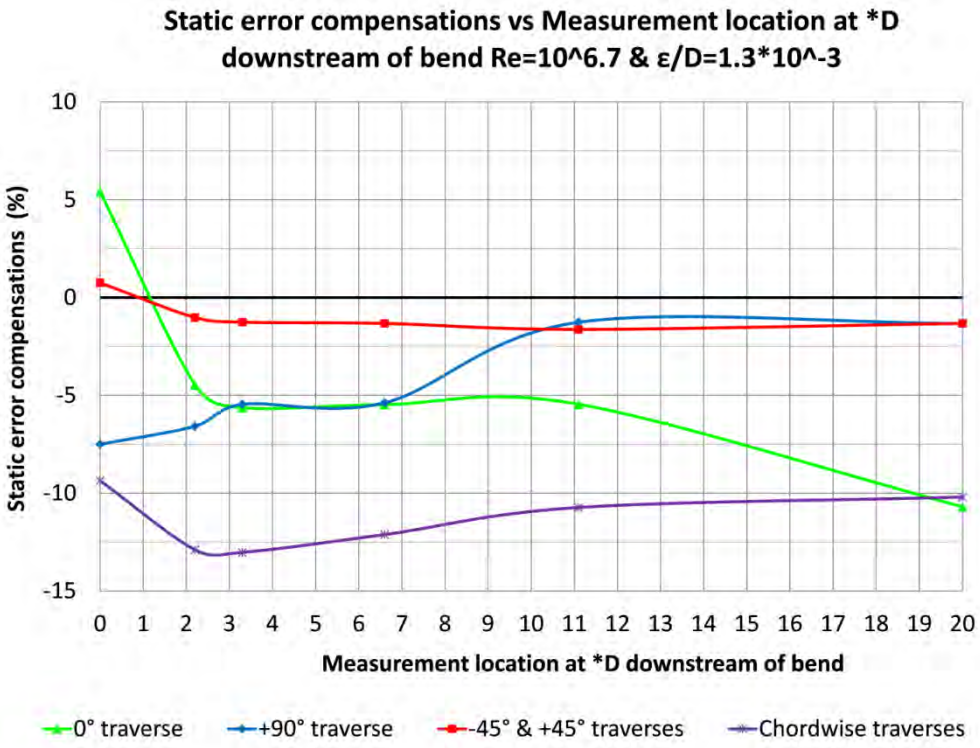
Static error compensations vs Measurement location at *D downstream of bend Re=10^6.7 & ε/D=1.3*10^-3
Static error compensations (%)
10
5
0
-5
-10
-15
0 1 2 3 4 5 6 7 8 9 10 11 12 13 14 15 16 17 18 19 20
Measurement location at *D downstream of bend
0° traverse
+90° traverse
-45° & +45° traverses
Chordwise traverses

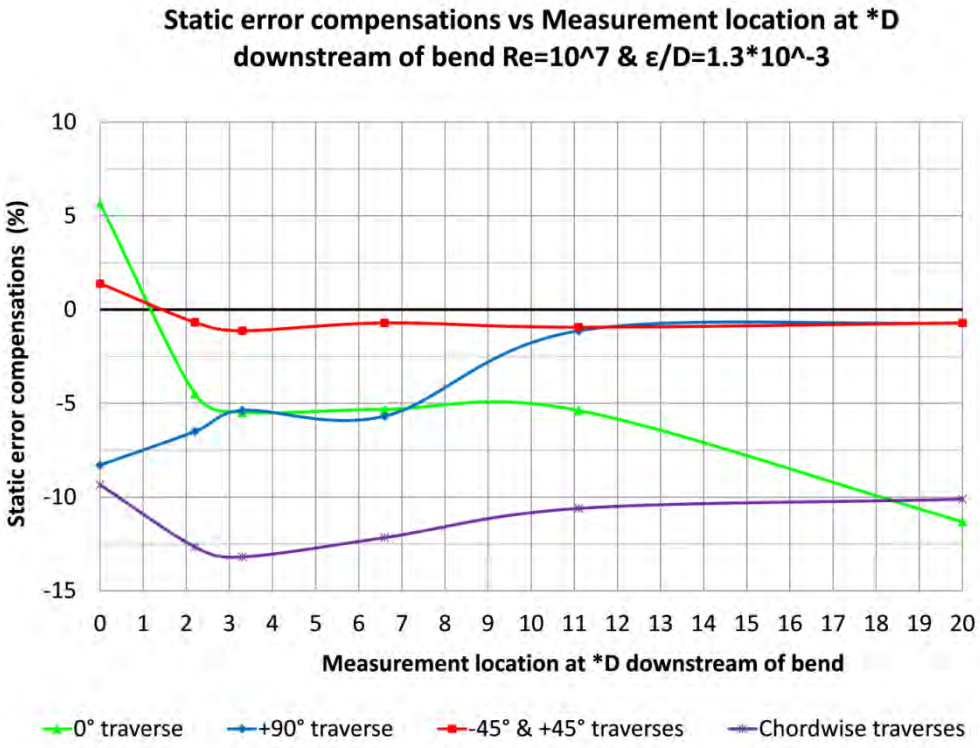
Static error compensations vs Measurement location at *D downstream of bend Re=10^7 & ε/D=1.3*10^-3
Static error compensations (%)
10
5
0
-5
-10
-15
0 1 2 3 4 5 6 7 8 9 10 11 12 13 14 15 16 17 18 19 20
Measurement location at *D downstream of bend
0° traverse
+90° traverse
-45° & +45° traverses
Chordwise traverses

Appendix D. Experimental Results

The following graphs represent experimental results for the calibration of the probe at 20D downstream of a bend at different flow conditions and traversing paths.

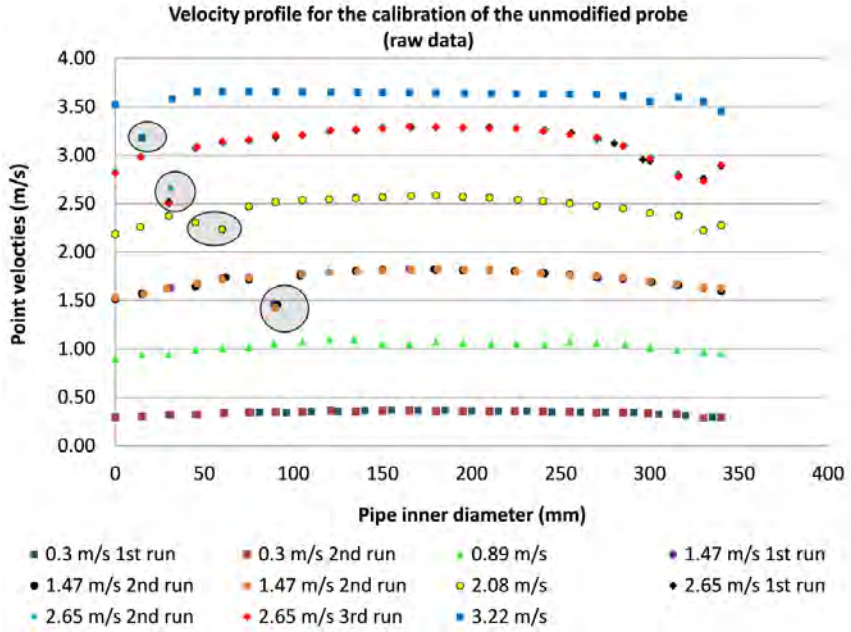

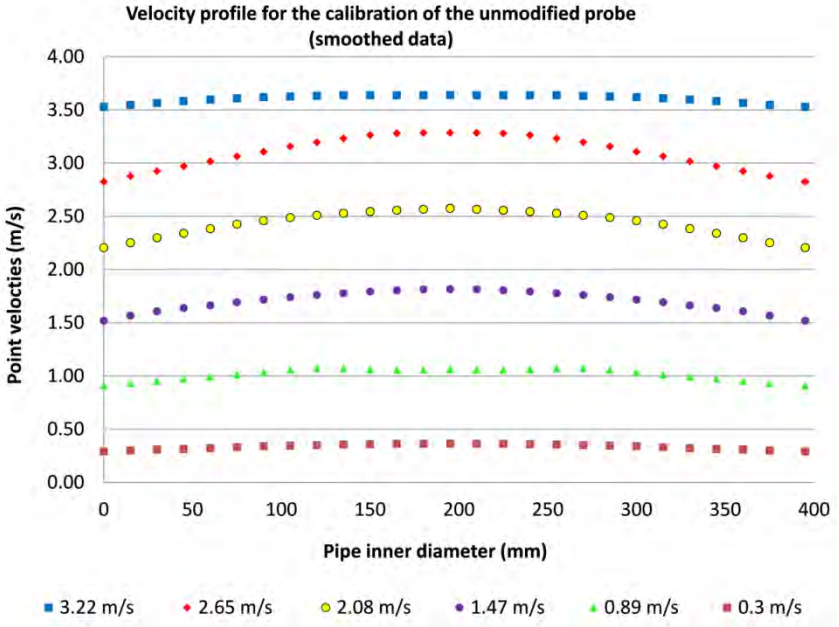

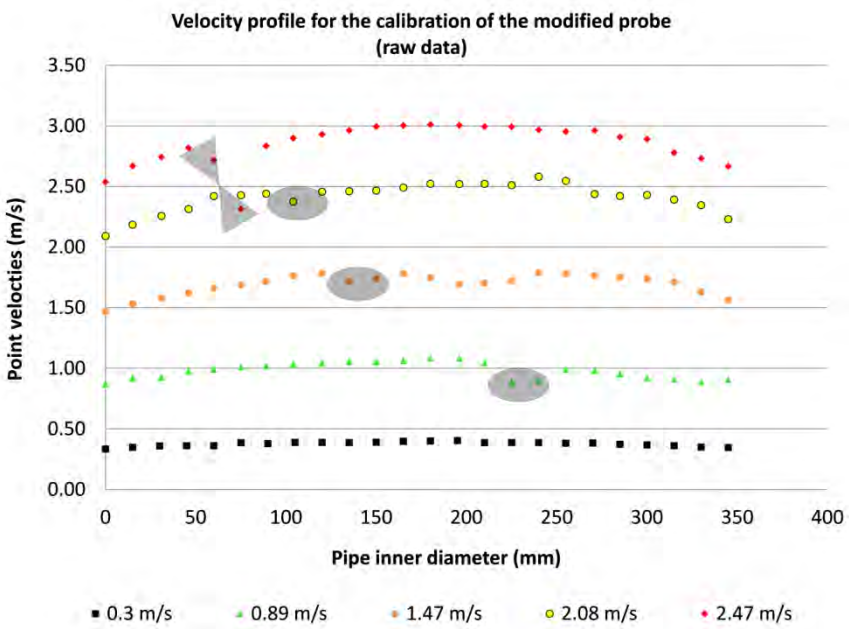
Velocity profile for the calibration of the modified probe
(raw data)
Point velocties (m/s)
3.50
3.00
2.50
2.00
1.50
1.00
0.50
0.00
0
50
100
150
200
250
300
350
400
Pipe inner diameter (mm)
0.3 m/s
0.89 m/s
1.47 m/s
2.08 m/s
2.47 m/s

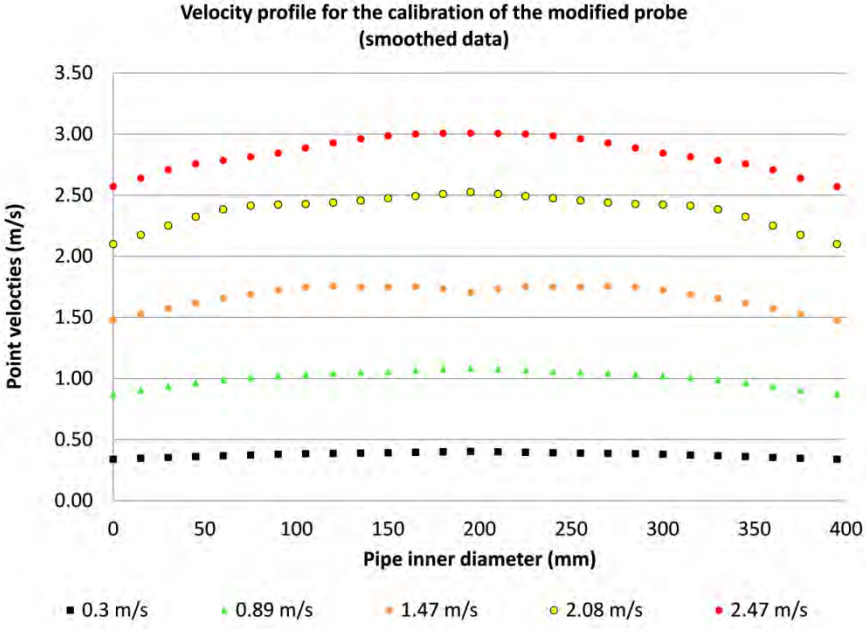
Velocity profile for the calibration of the modified probe
(smoothed data)
Point velocties (m/s)
3.50
3.00
2.50
2.00
1.50
1.00
0.50
0.00
0
50
100
150
200
250
300
350
400
Pipe inner diameter (mm)
0.3 m/s
0.89 m/s
1.47 m/s
2.08 m/s
2.47 m/s

The following graphs represent experimental results for flow measurements conducted at 2.2D downstream of a bend at different flow conditions and traversing paths.

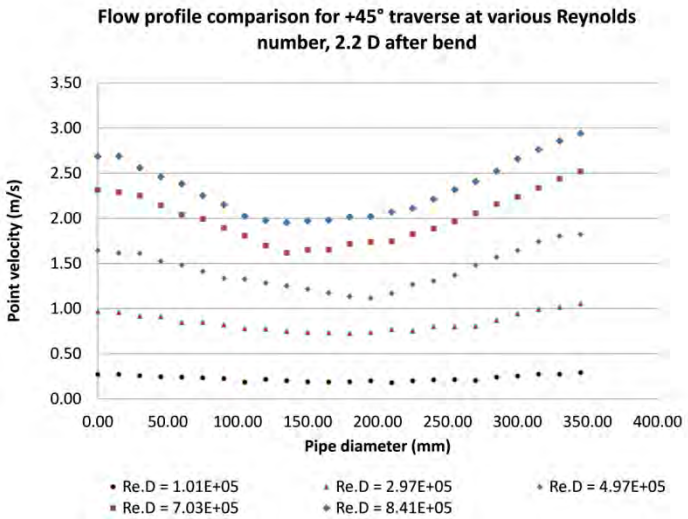

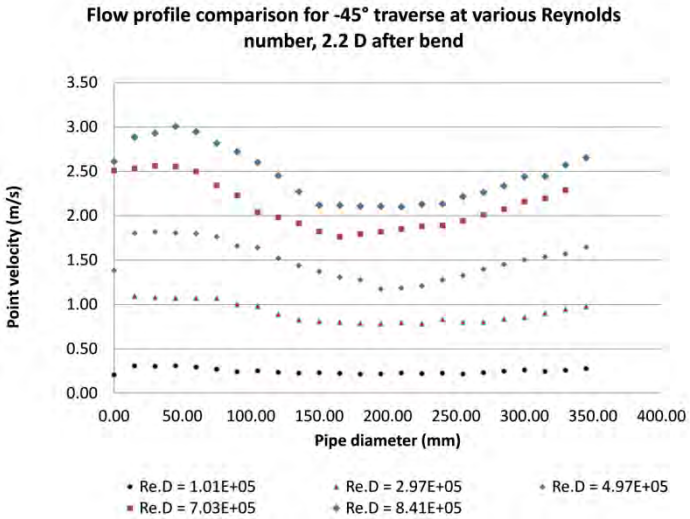

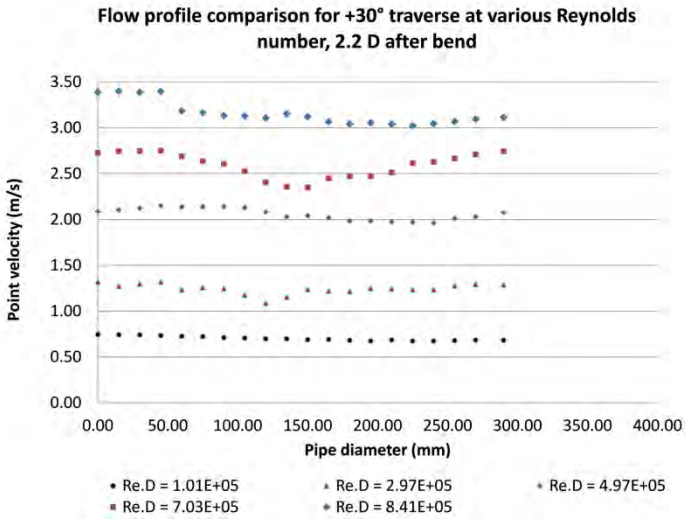
Flow profile comparison for +30° traverse at various Reynolds number, 2.2 D after bend
Point velocity (m/s)
3.50
3.00
2.50
2.00
1.50
1.00
0.50
0.00
0.00 50.00 100.00 150.00 200.00 250.00 300.00 350.00 400.00
Pipe diameter (mm)
Re.D = 1.01E+05
Re.D = 2.97E+05
Re.D = 4.97E+05
Re.D = 7.03E+05
Re.D = 8.41E+05

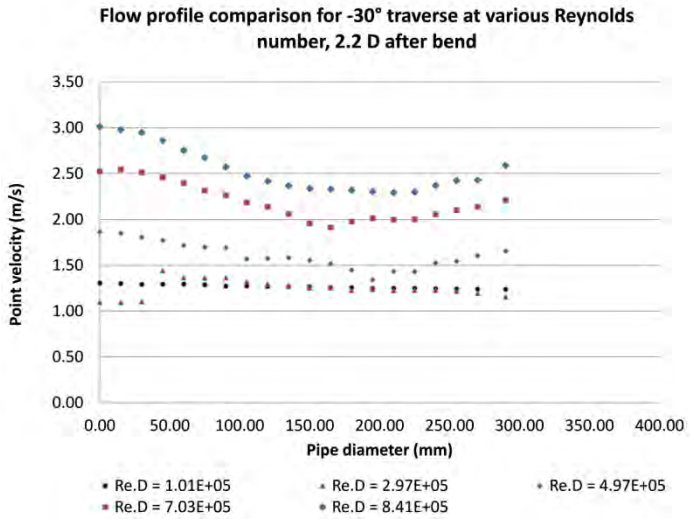
Flow profile comparison for -30° traverse at various Reynolds number, 2.2 D after bend
Point velocity (m/s)
3.50
3.00
2.50
2.00
1.50
1.00
0.50
0.00
0.00 50.00 100.00 150.00 200.00 250.00 300.00 350.00 400.00
Pipe diameter (mm)
Re.D = 1.01E+05
Re.D = 2.97E+05
Re.D = 4.97E+05
Re.D = 7.03E+05
Re.D = 8.41E+05

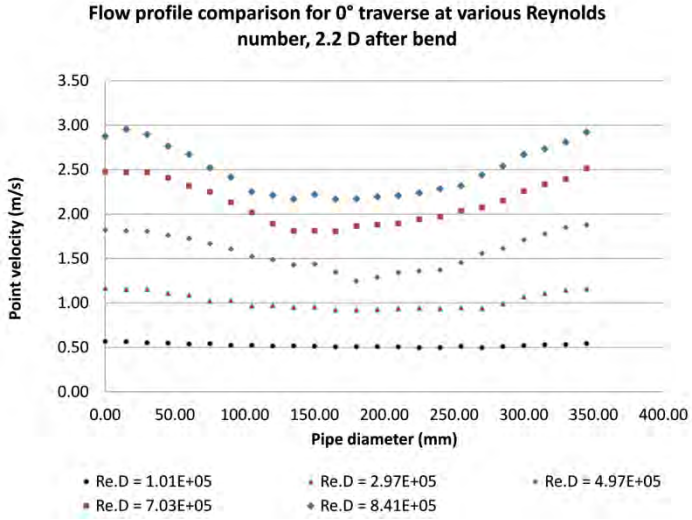
Flow profile comparison for 0° traverse at various Reynolds number, 2.2 D after bend
Point velocity (m/s)
3.50
3.00
2.50
2.00
1.50
1.00
0.50
0.00
0.00 50.00 100.00 150.00 200.00 250.00 300.00 350.00 400.00
Pipe diameter (mm)
Re.D = 1.01E+05
Re.D = 2.97E+05
Re.D = 4.97E+05
Re.D = 7.03E+05
Re.D = 8.41E+05

The following graphs represent experimental results for flow measurements conducted at 6.6D downstream of a bend at different flow conditions and traversing paths.

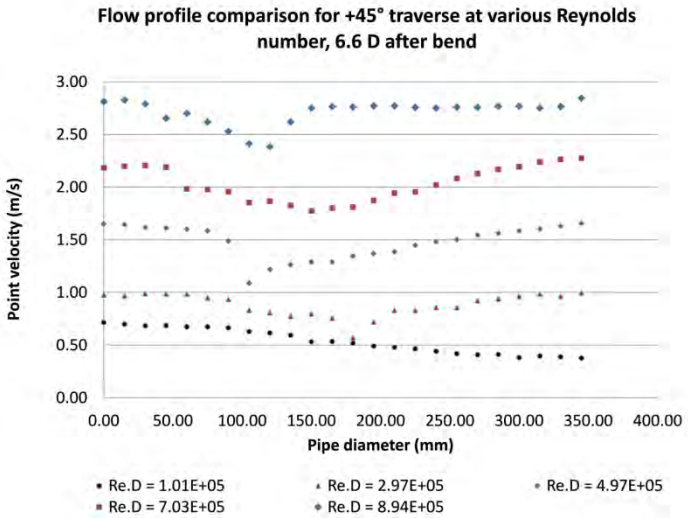

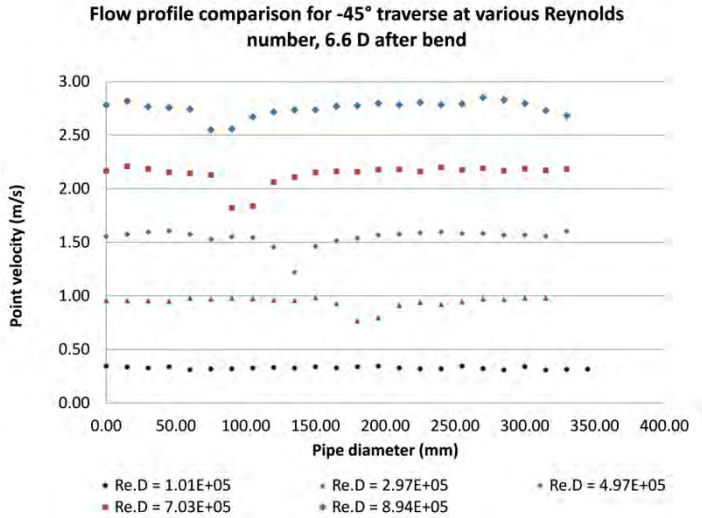

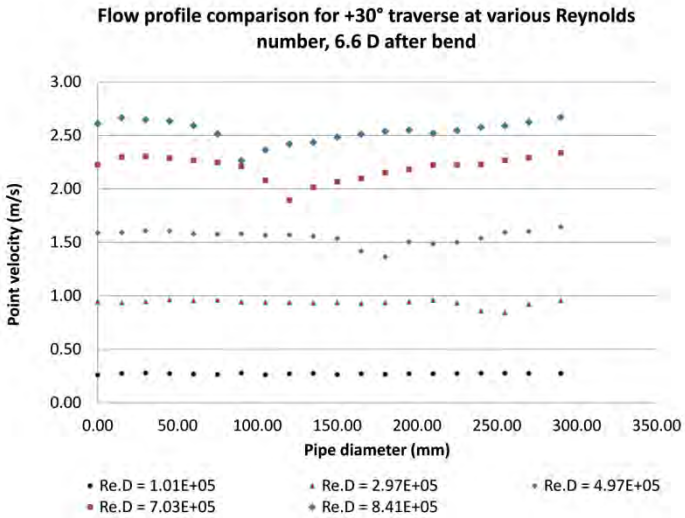
Flow profile comparison for +30° traverse at various Reynolds number, 6.6 D after bend
Point velocity (m/s)
3.00
2.50
2.00
1.50
1.00
0.50
0.00
0.00 50.00 100.00 150.00 200.00 250.00 300.00 350.00
Pipe diameter (mm)
Re.D = 1.01E+05
Re.D = 2.97E+05
Re.D = 4.97E+05
Re.D = 7.03E+05
Re.D = 8.41E+05

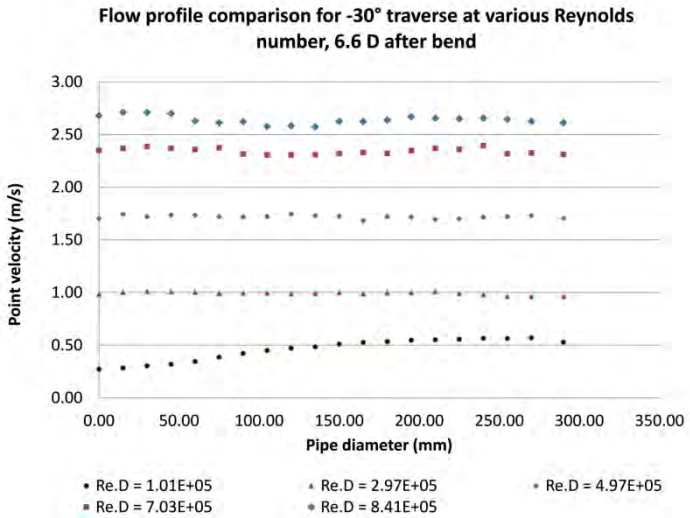
Flow profile comparison for -30° traverse at various Reynolds number, 6.6 D after bend
Point velocity (m/s)
3.00
2.50
2.00
1.50
1.00
0.50
0.00
0.00 50.00 100.00 150.00 200.00 250.00 300.00 350.00
Pipe diameter (mm)
Re.D = 1.01E+05
Re.D = 2.97E+05
Re.D = 4.97E+05
Re.D = 7.03E+05
Re.D = 8.41E+05

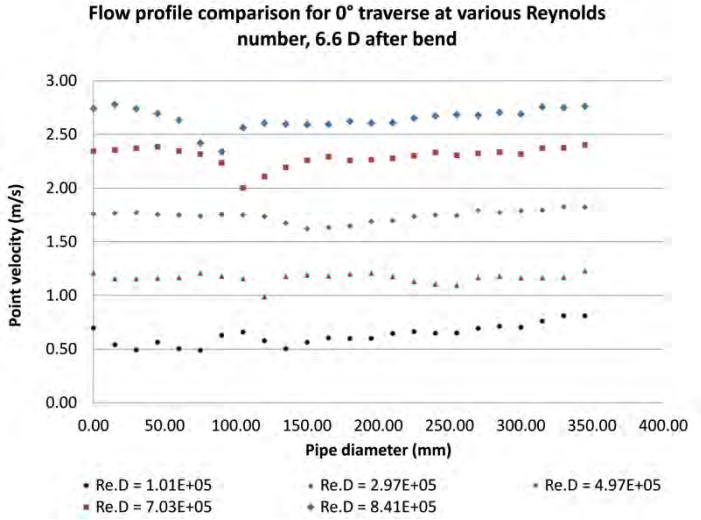
Flow profile comparison for 0° traverse at various Reynolds number, 6.6 D after bend
Point velocity (m/s)
3.00
2.50
2.00
1.50
1.00
0.50
0.00
0.00 50.00 100.00 150.00 200.00 250.00 300.00 350.00 400.00
Pipe diameter (mm)
Re.D = 1.01E+05
Re.D = 2.97E+05
Re.D = 4.97E+05
Re.D = 7.03E+05
Re.D = 8.41E+05

The following graphs represent experimental results for flow measurements conducted at 11.1D downstream of a bend at different flow conditions and traversing paths.

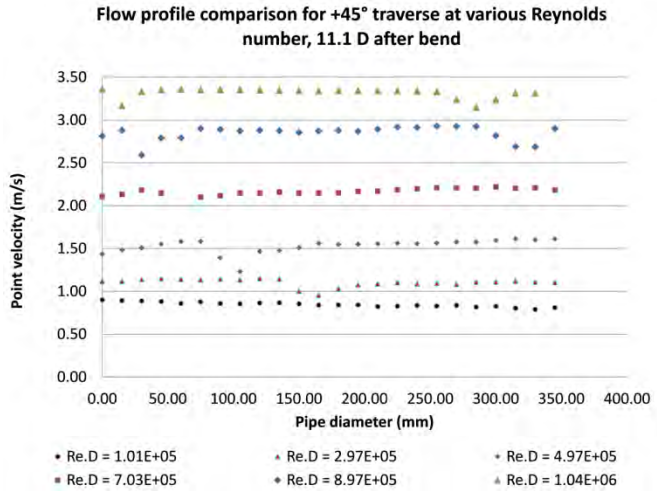

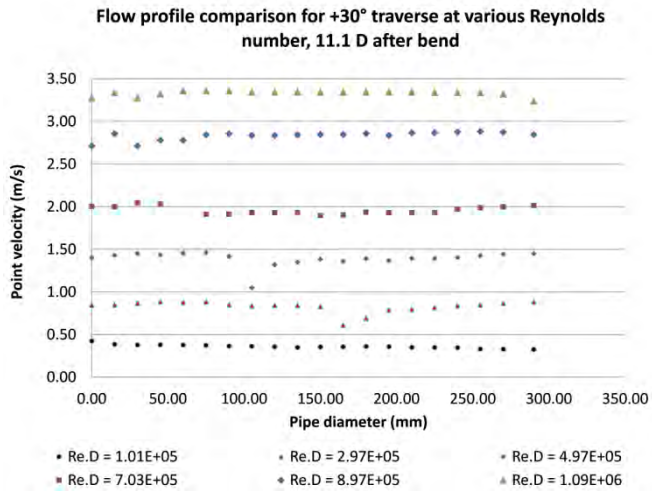

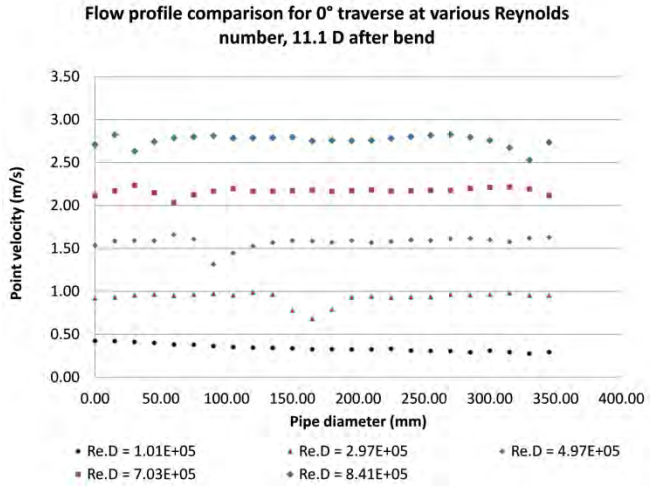

Appendix E. Probe Integrity Calculations

Average flow velocity through the pipe:

$$V_f := \begin{pmatrix} 0.1 \\ 0.3 \\ 0.6 \\ 0.9 \\ 1.2 \\ 1.5 \\ 1.8 \\ 2.1 \\ 2.4 \\ 2.7 \\ 3 \\ 3.3 \end{pmatrix} \frac{m}{s}$$

$D_{pipe} := 395mm$

Probe thickness (assumption):

$t := 1mm$

Probe maximum insertion length:

$L_{max} := D_{pipe}$

Density of water at $20\,°C$:

$$\rho_w := 999.4 \frac{kg}{m^3}$$

Drag force on the probe

Drag coefficient for a circular cylinder:

$C_D := 1.2$

A conservative approach was taken to determine the maximum drag force and its position along the probe. The resulting bending moment was then calculated. Maximum projected area when the probe is fully inserted through the centre of the duct to the opposite wall:

$A_{max\_projected} = 2r_o \cdot L_{max}$

Maximum drag force on the probe for various flow rates:

$$F_D = C_D \frac{1}{2} \rho_w \cdot A_{max\_projected} \cdot V_f^2$$

$$F_D = C_D \frac{1}{2} \rho_w \cdot (2r_o \cdot L_{max}) \cdot V_f^2$$

Maximum bending moment on the probe. Here the drag force is applied at the midpoint of the probe when fully inserted through the centre of the duct to the opposite wall:

$$M_B = F_D \cdot \frac{L_{max}}{2}$$

$$M_B = C_D \frac{1}{2} \rho_w \cdot (2r_o \cdot L_{max}) \cdot V_f^2 \cdot \frac{L_{max}}{2}$$

$$M_B = \frac{C_D \cdot \rho_w \cdot r_o \cdot L_{max\_insertion}^2 \cdot V_f^2}{2}$$

Second moment of area (I) considers the geometry of the cross section to measure the stiffness. It does not consider the cross section's material property:

$$I = \frac{\pi\left(r_o^4 - r_i^4\right)}{4}$$

Probe material yield strength, (brass) (MPa):

$\sigma_y := 205MPa$ at 20deg C

Safety factor:

$N_s := 2$

Allowable bending stress:

$$\sigma_B := \frac{\sigma_y}{N_s}$$

Corresponding maximum bending stress:

$$\sigma_B = \frac{M_B \cdot y}{I}$$

The maximum bending stress occurs at:

$y = r_o$

Maximum bending stress on a probe traversed all the way to the opposite duct wall for a given probe diameter (d), duct diameter (D), average flow velocity V_f.

$$\sigma_B = \frac{4 C_D \rho_w \cdot r_o^{\,2} \cdot L_{max}^{\,2} \cdot V_f^{\,2}}{\pi\left(r_o^{\,4} - r_i^{\,4}\right)}$$

$$r_i = r_o - t$$

$$\sigma_B = \frac{4 C_D \rho_w \cdot r_o^{\,2} \cdot L_{max}^{\,2} \cdot V_f^{\,2}}{\pi\left[r_o^{\,4} - \left(r_o - t\right)^4\right]}$$

For a material with an allowable stress of 200MPa and a safety factor of 2, the allowable bending stress is

$\sigma_B := 100\text{MPa}$

$L_{max} := 3\text{m}$

$$fn\left(r_o, V_f, t\right) := \frac{4 C_D \rho_w \cdot r_o^{\,2} \cdot L_{max}^{\,2} \cdot V_f^{\,2}}{\pi\left[r_o^{\,4} - \left(r_o - t\right)^4\right]} - \sigma_B$$

Initial probe outer radius guess: $rx := 10\text{mm}$

$V_f := 0.1\frac{\text{m}}{\text{s}}, 0.2\frac{\text{m}}{\text{s}} .. 3.5\frac{\text{m}}{\text{s}}$

probe outer for V_f=1m/s and wall thickness t=1mm

$$\text{root}\left(fn\left(rx, 1\frac{\text{m}}{\text{s}}, 1\cdot\text{mm}\right), rx\right) = 35.829\text{mm}$$

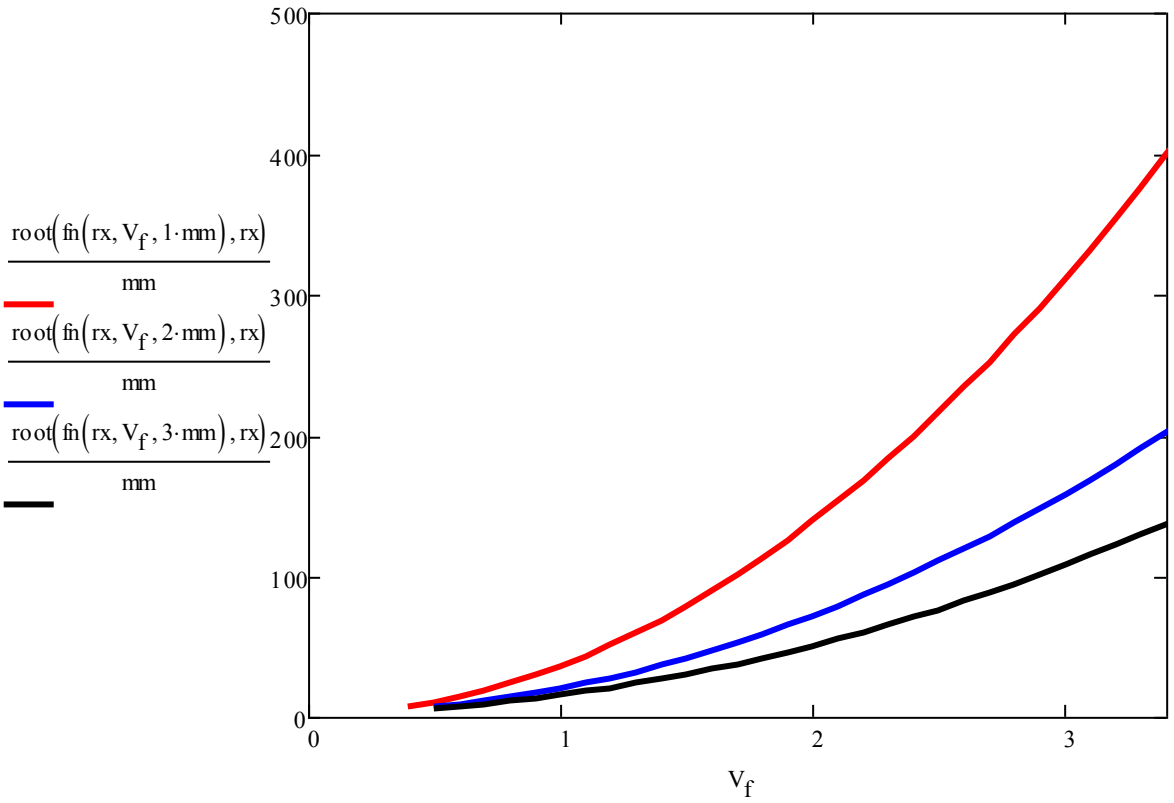
root(fn(rx, Vf, 1·mm), rx) / mm
root(fn(rx, Vf, 2·mm), rx) / mm
root(fn(rx, Vf, 3·mm), rx) / mm
500
400
300
200
100
0
0
1
2
3
Vf

Appendix F. Probe Vibration Analysis

Area moment of inertia for an annulus of inner radius r1 and outer radius r2:

$$I = \frac{\pi}{4}\left(r_2^{\,4} - r_1^{\,4}\right)$$

For a thin tube approximation:

$$I = \pi r^3 t$$

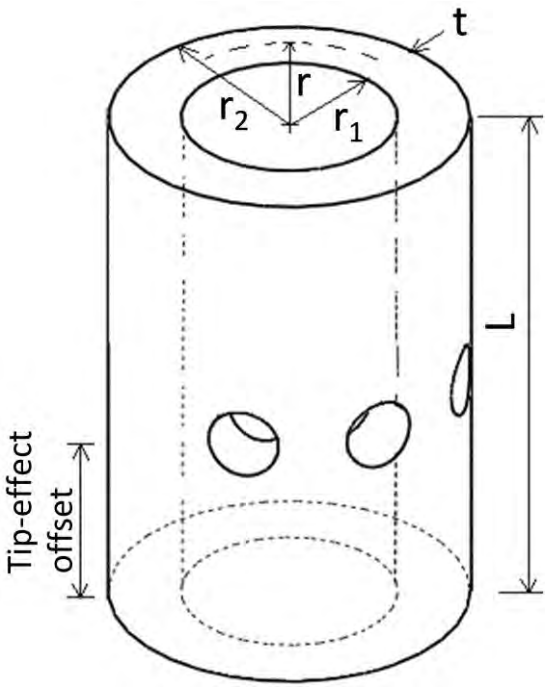

Figure 94: Thin wall cylinder

Natural frequency:

$$f_{b\_n} = \frac{1}{2\pi}\cdot\sqrt{\frac{k_{eq}}{m}}$$

Equivalent stiffness:

$$k_{eq} = \frac{3E\cdot I}{L^3}$$

Cross sectional area:

$$A_{cross} = 2\pi r\cdot t$$

Mass for a exposed length L:

$$m = \rho\cdot A_{cross}\cdot L$$

Substituting equivalent stiffness , mass and Cross sectional area equation ,natural frequency becomes:

$$f_n = \frac{1}{2\pi}\cdot\sqrt{\frac{3\cdot E\cdot\left(\pi r^3 t\right)}{L^3\cdot\rho\cdot(2\pi r\cdot t)\cdot L}}$$

$$f_n = \frac{1}{2\pi}\cdot\sqrt{\frac{3\cdot E\cdot\left(\pi r^3 t\right)}{L^3\cdot\rho\cdot(2\pi r\cdot t)\cdot L}}$$

$$f_n = \frac{1}{2\pi}\cdot\sqrt{\frac{3\cdot E\cdot r^2}{2\cdot\rho\cdot L^4}}$$

Natural frequency for an annulus with a thin wall can be simplified to:
includes 50mm offset

$$Exp\_data := \begin{pmatrix} 65 & 3.22 \\ 80 & 2.5 \\ 110 & 2.08 \\ 140 & 1.47 \end{pmatrix}$$

Young's modulus for the brass section:

$E := 100GPa$

Mass density for the brass section:

$$\rho := 8430\,\frac{kg}{m^3}$$

Exposed probe length during experiments where the probe oscillated:

$L_{exp} := Exp\_data^{\langle 0\rangle}\,mm$

Average flow velocity at which resonance was suspected during experiments:

$$V_{exp} := Exp\_data^{\langle 1\rangle}\,\frac{m}{s}$$

Probe diameter:

$d := 5mm$

Strouhal number for a cylinder:

$S_{st} := 0.2$

Corresponding excitation frequency due to vortex shedding:

$$f_{st} := \frac{S_{st}\cdot V_{exp}}{d} = \begin{pmatrix} 128.8 \\ 100 \\ 83.2 \\ 58.8 \end{pmatrix}\frac{1}{s}$$

Corresponding probe length at which resonance was suspected during experiments:

$L_{exp} := Exp\_data^{\langle 0 \rangle}\ mm$

The aim is to find a geometric parameter of the probe that remains constant and thus can be input into the calculation of the probes natural frequency, Set $f_{st}=f_n$ to find r:

$$f_{st} = \frac{1}{2\pi}\cdot\sqrt{\frac{3\cdot E\cdot r^2}{2\cdot\rho\cdot L^4}}$$

$i := 0..last(L_{exp})$

$$r_i := \sqrt{\frac{8\cdot\pi^2\rho\cdot\left(f_{st_i}\right)^2\cdot\left(L_{exp_i}\right)^4}{3E}}$$

$mean(r) = 1.245\times 10^{-3}\ m$

Since r is the geometric property of the probe and remains constant:

$r_{eq} := mean(r)$

$d_{eq} := 2.r_{eq}$

$d_{eq} = 2.49\cdot mm$

$$f_n := \frac{1}{2\pi}\cdot\sqrt{\frac{3\cdot E\cdot\left(r_{eq}\right)^2}{2\cdot\rho\cdot L_{exp}^4}}$$

Average flow velocity

$$V_f := \begin{pmatrix} 0.001 \\ 0.2 \\ 0.4 \\ 0.6 \\ 0.8 \\ 1 \\ 1.2 \\ 1.4 \\ 1.6 \\ 1.8 \\ 2 \\ 2.2 \\ 2.4 \\ 2.6 \\ 2.8 \\ 3 \\ 3.2 \\ 3.4 \\ 3.6 \\ 3.8 \\ 4 \end{pmatrix} \frac{m}{s}$$

Resultant excitation frequency

$$f_{st} := \frac{S_{st} \cdot V_f}{d}$$

$$f_n := f_{st}$$

Theoretical length at which resonance is expected:

$$L_{theoretical} := \sqrt[4]{\frac{3 \cdot E \cdot (r_{eq})^2}{4 \rho \pi^2 f_n{}^2}}$$

The graph below represents the theoretical exposed length and respective natural frequency and average flow velocity and corresponding excitation frequency.